Project No. 14-6482

# Studies of Lanthanide Transport in Metallic Fuel

## Fuel Cycle Research and Development

**Jinsuo Zhang**
The Ohio State University

Janelle Eddins, Federal POC
Steven Hayes, Technical POC

NEUP Nuclear Energy University Programs
U.S. Department of Energy

**Final Report**

**Project No**. 14-6482

**Project Title:** Studies of Lanthanide Transport in Metallic Fuel

**Principal Investigator:** Jinsuo Zhang (10/01/2014-09/30/2017); Christopher Taylor (10/01/2017-12/31/2017)

**Institution:** The Ohio State University (OSU); Virginia Tech (VT); Los Alamos National Laboratory (LANL); Idaho National Laboratory (INL)

**Collaborator:** Cetin Unal (LANL), R. D. Mariani, R. C. Martineau (INL)

**Students:** Xiang Li (Ph.D, OSU), Jeremy Isler (M.S., OSU), Weiqian Zhuo (Ph.D, VT)

**Postdoc:** Adib Samin (OSU), Charles Arnold (LANL), Christopher Matthews (LANL), Yi Xie (VT),

**Duration:** 10/01/2014 to 12/30/2017

**Total Funding Level:** $800,000

**TPOC:** Hayes , Steve

**Federal Manager:** Goldner, Frank

**Workscope:** FC 2.1

**PICSNE Workpackage #:** NU-14-OH-OSU-0101-03

**Contacting Information:** Prof. Jinsuo Zhang, Email: zjinsuo5@vt.edu phone: 540-231-9675

# Table of Contents

# List of Figures

# List of Tables

## 1. Executive Summary

Metallic nuclear fuels were tested in fast reactor programs and performed well. However, metallic fuels have shown the phenomenon of FCCI that are due to deleterious reactions between lanthanide fission products and cladding material. As the burnup is increased, lanthanide fission products that contact with the cladding could react with cladding constituents such as iron and chrome. These reactions produce higher-melting intermetallic compounds and low-melting alloys, and weaken the mechanical integrity. The lanthanide interaction with clad in metallic fuels is recognized as a long-term, high-burnup cause of the clad failures. Therefore, one of the key concerns of using metallic fuels is the redistribution of lanthanide fission products and migration to the fuel surface. It is believed that lanthanide migration is in part due to the thermal gradient between the center and the fuel-cladding interface, but also largely in part due to the low solubility of lanthanides within the uranium-based metal fuel. PIE of EBR-II fuels shows that lanthanides precipitate directly and do not dissolve to an appreciable extent in the fuel matrix.

Based on the PIE data from EBR-II, a recent study recommended a so-called "liquid-like" transport mechanism for lanthanides and certain other species. The liquid-like transport model readily accounts for redistribution of Ln, noble metal fission products, and cladding components in the fuel matrix. According to the novel mechanism, fission products can transport as solutes in liquid metals, such as liquid cesium or liquid cesium–sodium, and on pore surfaces and fracture surfaces for metals near their melting temperatures. Transport in such solutions is expected to be much more rapid than solid-state diffusion. The mechanism could explain the Ln migration to the fuel slug peripheral surface and their deposition with a sludge-like form. Lanthanides have high solubility in liquid cesium but have low solubility in liquid sodium. As a result, Ln could transport to the fuel surface through pores filled with liquid cesium fission products. At the fuel slug surface, the lanthanides would undergo rapid precipitation when swamped with the large increase in liquid sodium content and cooler temperatures, which would lead to the observed sludge-like deposit. Prior PIE data also show that lanthanide deposits were found on the cold sides of closed and isolated pores, i.e., on pore surfaces directed away from the center, which can also be explained by the liquid-like transport theory. Since the total amount of lanthanides exceeds their solubility limit in liquid cesium, the small temperature gradient across a pore combined with the long durations is sufficient to drive cesium-mediated transport of lanthanides to the cold side of the pore. The liquid-like transport mechanism can qualitatively account for the migration and redistribution of lanthanides fission products in metallic fuels.

The present project studied the mechanisms of lanthanide transport in metallic fuels

based on the novel interpretation of ‘liquid-like’ transport mechanism experimentally and analytically. The project completed all the proposed research tasks by using an integral approach: (1) experimental studies for measurements of key parameters and first principles calculations to determine, for example, lanthanide solubility and diffusion coefficient in liquid cesium, sodium and cesium-sodium alloy; (2) theoretical model development for lanthanide transport in a non-isothermal single pore and porous medium to understand the observed behavior (deposition, dissolution and migration) in a single closed or open pore and porous medium; (3) further development of the multi-phase/physics BISON model. The key goal of the project is to develop fundamental understanding of the lanthanide fission product migration and redistribution in advanced metallic nuclear fuels, and then to provide fundamental theory/data for mitigating FCCI of advanced metallic fuels.

Experimentally, the project investigated the interaction between the lanthanides and cesium and sodium, with a focus on the solubility of the lanthanides in these liquid alkali metals. First, a prediction of the solubility was calculated using the Miedema model. This prediction was then compared to the inversion crucible solubility experiment performed in this study. The solubility experiment studied the temperature and liquid-composition dependence of the lanthanides in liquid sodium, cesium and sodium-cesium mixtures. In addition, the solubility in mixtures shows the various alkali metals concentration effect on the solubility. With the results of differential scanning calorimetry (DSC) experiments, updated phase diagrams for sodium-neodymium and cesium-neodymium were obtained from the experimental data. The temperature dependence of the solubility of neodymium in liquid cesium and the solubility differences in liquid sodium and liquid cesium provide key experimental data towards the theory of ‘liquid-like’ transfer.

Numerically and theoretically, the project established the “liquid-like” mechanism based MOOSE/BISON model to describe Ln transport behaviors both in pore-scale and macroscopic porous media. The project also conducted theoretically analysis on the Soret effects on Ln transport based on the liquid-like mechanism. Fundamental properties of three abundant Ln during FCCI (Ce, Pr, Nd) such as solubility and diffusivity in liquid Na, Cs and Na-Cs mixture have been obtained via different simulation methods. By applying the corresponding material properties into models, it turns out “liquid-like” transport mechanism can account for the Ln migration down the temperature from the fuel center to the surface. The Na or Cs filled pores can provide a path for Ln to move through at fast speed due to the large Ln diffusion coefficients in these alkali metal solutions and Soret effects. With the temperature driving force considered by the inclusion of Soret effects, Ln tend to migration down the temperature gradient and precipitate on the cold side of both the liquid metal filled pores and the Na-filled gap. The major physical kinetics has been included either in the media block

or at the interface and the corresponding reaction rate constants have been clarified. This work can serve as a framework for the development of more sophisticated model by including more physical kinetics and determining the corresponding parameters. The greater understanding of the lanthanide transport in the U-Zr fuel allows for the fuel to be more efficiently engineered to mitigate FCCI and thus achieve to higher burnups.

# 2. Lanthanide Behaviors in Metallic Fuels

## 2.1 Development of Metallic Fuel

The selection by the Generation IV International Forum of sodium-cooled fast reactor concept has brought metallic fuels, such as U-Zr fuel, under renewed focus [1]. Metallic U-Zr fuels have shown advantageous capabilities, including a high thermal conductivity, high fissile atom density, easy fabrication, and pyroprocessing capability. Along with these properties, metallic fuels have shown good performance on both steady state and transient operating conditions of sodium-cooled fast reactors by experiments performed with the experimental breeder reactor II (EBR-II) [2]. The metallic fuel pin is comprised of rod-shaped fuel alloy made of U-Fs (Fs (fissium) is composed of elements Ru, Mo, Pd, Te, Rh, Nb and Zr.), U-Zr or U-Pu-Zr, the fuel-to-clad gap filled with liquid sodium (Na), and steel cladding (HT-9) [2]. The fuel pin is designed to allow for fuel swelling within the fuel-to-clad gap, and fission gas accumulating in the top plenum during reactor operation.

One of the earliest developments on metallic fuels was alloying. Some of the earliest alloying additions included molybdenum (Mo) and fissium (Fs). Later, Zr became the alloying element for metallic fuel in the use of EBR-II and fast flux test facility (FFTF) [3]. Alloying with Zr presents the ability to raise the solidus temperature of fuel, increase the compatibility between cladding and fuel, and increase the dimensional stability of metallic fuel under irradiation. It was also identified that the best composition of Zr is 10 wt.% in the fuel [5]. Although fuel alloying can increase the dimensional stability of metallic fuels under irradiation, design refinement of fuel element is still desired to reduce the effects of fuel swelling and chemical interactions between fuel and cladding.

At the beginning of metallic fuel development, the fuel-to-clad gap was relatively small, so large stresses were generated when fuel swells even at very low specific burnups (~3 at.%) [4]. Failures from the fuel imposing stresses on the cladding is known as fuel-cladding mechanical interaction (FCMI). To overcome FCMI, the designed thickness of fuel-to-clad gap was increased. The smear density was decreased to 75 % to allow the fuel with more initial unconstrained swelling to prevent failures caused by FCMI [5]. With 75 % smear density, an adequate amount of swelling occurs with the porosity developing in the fuel to form interconnected pathways from the fuel to the gap. The interconnected pathways allow fission gas to release from the fuel and to accumulate in the plenum at the upper portion of fuel pin. The release of fission gas eliminates one of the largest contributors to swelling. The design of smaller smear density has alleviated FCMI and achieved higher burnups.

As allowing the fuel to swell, the transformations associated with higher burnups have become a significant focus. Figure 1a is an optical micrograph, showing these transformations of the irradiated U-Zr fuel element T225 at a burnup of 10 at.% [6]. Figure 1b is a schematic image of an irradiated fuel with several microstructure transformations of interest illustrated, including swelling, porosity, and constituent redistribution. Porosity developing in the swelling fuel is just one of many microstructure evolutions at high burnups. The other microstructure evolution was constituent redistribution in U-Zr fuels during reactor operation. Constituent redistribution results in a relatively higher Zr concentration at the fuel radial center and peripheral regions, while a higher U concentration at the intermediate regions. Previous work has shown that the constituent redistribution is driven by the temperature gradient between the fuel center and periphery [7]. The constituent redistribution in U-Zr fuels has some advantages: the increased Zr concentration at the center may improve the solidus temperature of the hottest part of fuel, and the increased Zr concentration at the periphery may increase the chemical compatibility between fuel and cladding. However, the disadvantage of redistribution is also critical as which would result in porosity and void formation in the fuel.

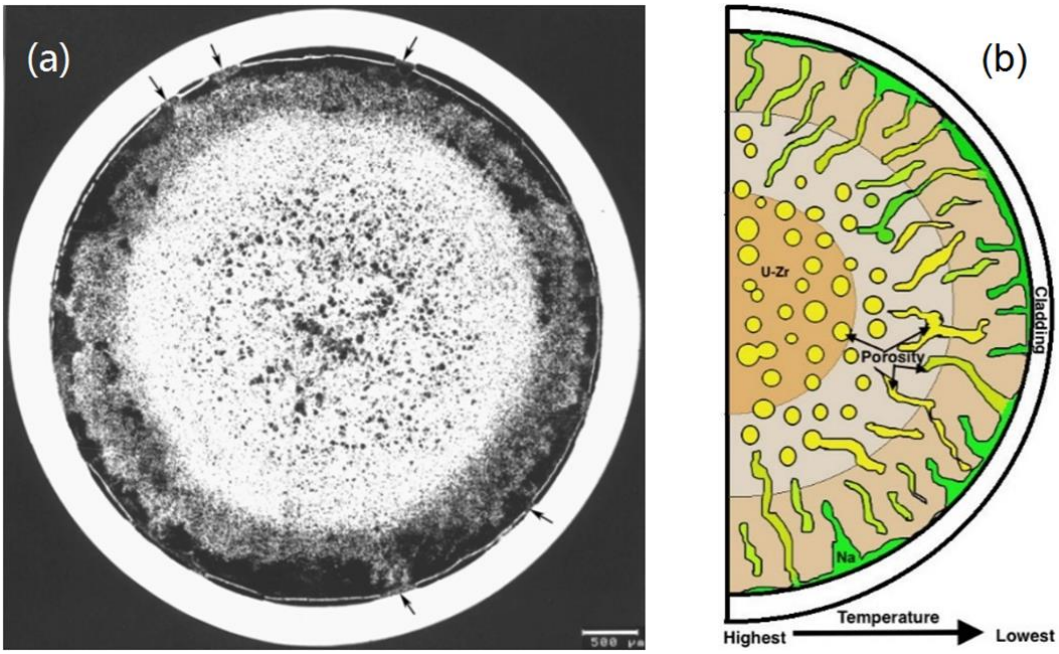


**Figure 1 Transformations of post-irradiation U-Zr fuel. (a) Optical micrograph of fuel cross section [6], and (b) schematic diagram of half cross section with fuel transformations [8].**

The swelling at the inner hottest region of fuel is dominated by the formation and growth of fission gas bubbles; while at the outer colder region is dominated by the tearing and cavity formation at grain boundaries. In addition to the various swelling

mechanisms, the amount of swelling differs as well. The differences of swelling occurring at different regions result in the overall fuel swelling anisotropic and cracks growing at the fuel periphery [9]. Caused by the cracks, cavities and fission gas bubbles, the U-Zr fuel may develop a pathway of porosity, which connects from the fuel interior to the fuel-to-clad gap. This interconnected porosity is one of key features in the release of fission gas and the elimination of FCMI. Furthermore, the interconnected porosity is the migration path of lanthanide (Ln) fission products, the chemistry of which plays an important role in fuel-cladding chemical interaction (FCCI) [10].

Metallic U-Zr fuels have been used in EBR-II and qualified up to a specific burnup of 10 at.%, however, such a burnup is still far below the desired burnup of 20 at.% for the advanced sodium-cooled fast reactor [11]. A major reason for the limitation of higher burnup is FCCI, which occurs at the fuel/cladding interface during irradiation [12]. FCCIs include fuel-cladding interactions (e.g. U-Fe) and lanthanide-cladding interactions (e.g. Ce-Fe). These chemical interactions may lead to cladding wastage with the formation of low temperature eutectics and brittle intermetallics. Low temperature eutectics composite of fuel constituents (U, Pu and Zr) and cladding constituents (Fe and Cr) have been found [13,14]. Liquefaction and liquid-phase penetration to cladding have been found during irradiation, the liquefied region is coincided with the Fe diffusion depth, the liquefaction threshold temperature is dependent on fuel composition and burnup [15,16]. However, the greatest concern of FCCI is lanthanide-cladding interactions, as lanthanide migrates fast in a fuel and diffuses rapidly into cladding.

## 2.2 Fuel-Cladding Interaction

One type of FCCI is due to the chemical interactions between the fuel components (U, or Zr) and the cladding constituents (Fe, Cr, or Ni). These inactions can be understood by diffusion couple tests (e.g. [17,18,19])

U/Fe Diffusion Couple

K. Huang et al.[20] reported the experimental efforts and inter-diffusion analysis for U-Fe diffusion couples annealed at multiple temperatures where uranium exhibits different phases: orthorhombic α-U at 853 K, 888 K, 923 K and tetragonal β-U at 953 K, 973 K.

There were two developed intermetallics $U_6Fe$ and $UFe_2$ with different growth rates. $U_6Fe$ grew faster and impeded the growth of $UFe_2$, while the $UFe_2$ growth had little impact on the growth of $U_6Fe$ [20]. The U6Fe phase layer with larger growth rate is much thicker than $UFe_2$. The change in specific heat and/or crystal structure of U resulting from the allotropic transformation (from α-U to β-U) also has impact on inter-

diffusion between U an $U_6Fe$ [35,20]. This binary system serves to form the basis for quantitative investigation of the effects of alloying addition (e.g., Zr, Cr and Ni) on the FCCI between metallic fuels and Fe based cladding materials [35].

U-Zr/Fe Diffusion Couple

A series of experiments have been conducted on diffusion couples of U-Zr/Fe and a complex multi-layer structure with various intermetallic compounds have been observed in the interaction zone in most cases [20]. Ogata et al. reported results of isothermal inter-diffusion of U-Zr/Fe as a function of time at an annealing temperature 923K [35]. Nakamura et al. [17] studied diffusion couples of U-Zr vs Fe and Fe-12at.%Cr alloy at multiple temperatures (908 K, 923 K, 953 K, 973 K, and 988 K) with formation of different phases in the reaction zone. Phase diagrams can shed light on microstructural and compositional development from diffusion couples and Raghavan [21] has accessed a ternary isothermal phase diagram for U-Zr-Fe at 973 K. In the reaction zone, the diffusion path varied regarding annealing temperature on the Fe side while remained the same regardless of the temperature on the U-Zr side [17]. Such difference in diffusional behaviors was accounted for by the potential variation in the formation energy of the $U_6Fe$, $UFe_2$, and $ZrFe_2$ phases [17,22].

With emphasis on the alloying addition of Zr, Park et al. examined the diffusional interaction in U-10wt.%Zr vs pure Fe diffusion couples at temperatures of 903 K, 923 K, and 953 K and observed layers constituted by multiple phases such as $U_6Fe$, $UFe_2$, $ZrFe_2$, α-U, β-U, Zr-precipitates, χ (Fe(Zr,U)), ε (Fe(Zr,U)$_2$) and λ($U_3$(Zr,Fe)) [19]. The reaction zone becomes thicker with the increasing temperature. Inter-diffusion microstructure development at an annealing temperature 953K with the largest reaction zone of approximately 152 μm. There are several localized regions of enrichment and depletion of U, Zr, and Fe near the pure Fe region [19]. Zr is depleted in the U-rich region and U appeared to preferentially diffuse through the $ZrFe_2$ phases to form $U_6Fe$ in the matrix of $UFe_2$ phase [19]. U was found to move faster than Zr on the Fe side and the rate of diffusional interaction between U and Fe was reduced by the inclusion of Zr [19].

To evaluate the liquid phase formation temperature during FCCI, Ogata et al. carried out inter-diffusion experiments at 923 K [35] and 1003K [23] with the diffusion couples consisting of U–23at.% Zr/Fe and U–23at.%Zr–1at.% Ce/Fe. Multiple developed layers in the reaction zone at an annealing temperature of 923K were respectively identified as: a single-phase layer $UFe_2$, a two-phase $U_6Fe$+$UFe_2$, a single-phase $ZrFe_2$, $U_6Fe$+$ZrFe_2$, $U_6Fe$+ε and αU+λ. Big difference can be observed between the appearances of the reaction zone structures at 1003 K shown in (b) and at 923 K in (a). And the reaction zone growth rates were different under two temperature conditions: it took only 90 min for the reaction zone to grow to about 400μm thickness at 1003 K

while 17 days to about 160 μm at 923 K [23]. A liquid phase forms in the reaction zone at 1003 K, just 5 K higher than the eutectic point in the U–Fe binary system [23]. The fact that the reaction zone grew much faster at 1003 K than at 923 K indicates Zr in the fuel alloy has little impact on the threshold temperature for the liquefaction onset [23]. Also the reaction zone structure at 1003 K showed independence of pre-annealing time and Ce addition[23]. Three different regions were found: (c): a fine two-phase-like region on the Fe side, a coarse two-phase-like region in the middle, and a fine two-phase-like region on the U–Zr or U–Zr–Ce side [23].

U-Pu-Zr/Fe

Ogata et al. examined the reaction zones formed in two couples U-13at.%Pu-22at.%Zr/Fe and U-22at.%Pu-22at.%Zr/Fe at 923 K and only found the liquid phase formation in the U-22at%Pu-22at%Zr/Fe couple [24]. The Pu content in the initial U-Pu-22at%Zr alloy was found to have a big influence on the phase combinations in reaction zones [24]. As the maximum Pu content in the $(U,Pu)_6Fe$ phase in the reaction zone increased with the initial Pu content in the fuel alloy, the liquid phase formed when the Pu concentration in the $(U, Pu)_6Fe$-type phase was larger than the Pu solubility limit of this phase [24]. This was also observed from experiments by Nakamura et al. on diffusion couples of U-Pu/Fe at 923K and 943 K [25]. Liquefaction at 923K occurred when the Pu/(U+Pu) ratio exceed 0.25 and the threshold Pu/(U+Pu) ratio for liquefaction onset became lower with increasing temperature which may be partly caused by the decreasing Pu solubility limit in the (U,Pu)6Fe phase with increasing temperature [25]. Based on multiple fuel-cladding compatibility tests, Nakamura et al. also claimed that the liquefaction condition is independent of the Zr content and can be expressed by a function of the reaction temperature and the atomic fraction ratio of Pu/(U+Pu) [25]. The developed U-Pu/Fe reaction zone was observed with each region consisted of a single-phase: $(U, Pu)Fe_2$, $(U, Pu)_6Fe$ [25]. Two and three-phase regions were formed in the reaction zone of U-Pu-Zr/Fe couples as reported in detail by Ogata et al. [24]. Aitkaliyeva et al. [26] performed a diffusion couple study on interaction between U-22wt.%Pu-4wt.%Zr fuel and pure Fe at elevated temperatures. These authors observed substantial FCCI layers formed upon heat treatment of the diffusion couple at 923K. An isothermal section for quaternary U-Pu-Zr-Fe system has been constructed [27].

Effects of Cr and Ni in Cladding Steels

In the diffusion couple between U-Zr fuel alloys and cladding steels, the developed intermetallics and diffusion structures are essentially dictated by the interactions of Fe, Ni, and Cr with U and Zr [28]. Other elements in the cladding steel appear to play a minor role [28]. Keiser et al. carried out experiments at 923K on diffusion couples assembled with a U-23at.% Zr alloy fuel and a series of cladding alloys of selected

compositions in the Fe-Ni-Cr system including pure Fe, pure Ni, three binary alloys Fe-20.1at.%Cr, Ni-16.4at.%Cr, Fe-10.1at.%lNi and a ternary alloy Fe-16.4at.%Ni-9.4at.%Cr [29]. The presence of Ni and Cr was found to have significant influence on the diffusional interaction between U-Zr alloy and various Fe-Cr-Ni alloys [29]. In binary U-Zr fuel/cladding couples, the presence of Ni led to diffusion zones larger than those in non-Ni containing couples because Ni can change the activities of other elements to facilitate formation of relatively large diffusion structures and more intermetallic phases [13]. In ternary U-Pu-Zr fuel/cladding couples, however, couples with the presence of Ni formed smaller diffusion zones than couples without Ni based on isothermal experiments of U-21at.%Pu-23at.%Zr/HT9 and U-21at.%Pu-23at.%Zr/D9 diffusion couples at 923K [13]. Association between Cr and formation of Zr-rich precipitates has been observed [29]. Cr can affect the activity of Zr in Zr-rich precipitates and cause them to decompose, yielding a Zr layer [13, 29]. Such Zr layer is beneficial to the mitigation of FCCI since it can impede the constitutional inter-diffusion between the fuel and the clad.

On the basis of inter-diffusion behaviors between fuel and cladding materials, Keiser et al. [28] concluded that that HT9 is a better choice for a cladding material compared with D9 or SS316 in the context of fuel-cladding compatibility. With the lowest Ni concentration of all the cladding steels, HT9 exhibits the smallest diffusion structure with the fewest number of phases, together with smallest penetration of Fe and Ni into the fuel [28]. Therefore, the less formation of low melting phases or strength reducing structures is expected in HT9 cladding [28].

## 2.3 Ln at Fuel/Clad Interface

Irradiation may enhance diffusion kinetics, thereby these results are different with the out-of-pile results, however, in-pile tests are limit, it's necessary to understand the chemical interactions of lanthanide and cladding through diffusion couple tests.

### 2.3.1 In-Pile Data Analysis

Both the fission yield and fission product decay during the post-irradiation period have an influence on the abundance of lanthanide fission products [30]. As indicated by a sample composition of an irradiated U-10Zr fuel pin at around 8 at.% burnup [31], the vast majority compositions of lanthanide fission products are Nd, Ce, Pr and La. Fission products that are relatively insoluble in the U-Zr fuel matrix have been found as precipitates in the pores of fuel, such as Ce precipitates [12][32][33]. The solubility of Ce in metallic fuel at the typical fuel irradiation temperature (923-973 K) is very low, therefore most of Ce that produced during burning is precipitated. Lanthanides have

been experimentally found precipitated in the pores of fuel [33], and they are the major fission products at the outer region of metallic fuels during irradiation [34]. The temperature gradient in metallic fuel appears to play an important role in the lanthanide migration to the periphery [6] because the isothermal diffusion couple tests of lanthanide-contained fuel did not show lanthanide migration to the fuel surface [35]. Lanthanide precipitates at the fuel periphery have been found even at low burnups, indicating the migration is rapid [36].

Post irradiation examination (PIE) data of metallic fuels (U-Zr and U-Pu-Zr) irradiated in EBR-II reactor were well summarized in the report [6]. The report found that some lanthanides (e.g. Nd, Ce, Pr, La, Sm and Pd) that were originally in the fuel finally were found in the cladding, indicating the occurrence of interdiffusion between lanthanides and cladding when fuel swells. Reports [6,11] also suggested Nd, Ce, Pr and La as the four major lanthanides diffusing into cladding.

The formation of liquid-phase is one of the major type of cladding degradation during FCCI. The liquid phase region coincides with the depth of Fe migration from the cladding as shown from microprobe analysis, the addition of Fe diffusion can form more liquid phase during the test at elevated temperatures [16]. Tsai, et al. reported that the interdiffusion layers on the fuel and cladding inner surface may liquefy, resulting in liquid-phase penetration into the cladding at a high temperature [15]. Results from the fuel behavior test apparatus (FBTA) on EBR-II fuel pins showed that noticeable liquid phase penetration occurred at temperatures higher than 998 K and two types of interactions, grain boundary penetration and matrix dissolution [15]. Cohen, et al. also reported the threshold temperatures for fuel-cladding interaction melting in a 1-h test on a U-19Pu-l0Zr/HT-9 (Alloy HT-9 is composite of 12 Cr, 1 Mo (wt.%), other minor elements such as Ni and C, and Fe as the balance ) element is 1013-1043 K for a 5.6 at.% burnup element, and 923-948 K for an 11 at.% burnup element [16]. The temperature threshold is impacted by the constituent near the fuel/clad interface. More Fe concentration in the fuel caused by the increased burnup may contribute to the lower threshold temperature, depending on the equilibrium phase diagram of the new metallic system.

The cladding penetration rate in the steel cladding is found to be significantly impacted by the existence of lanthanide fission products in the fuel/clad gap [15]. This is consistent with the observation from DP-1 tests reported by Tsai, et al., that FCCI is dominated by lanthanide fission products which were found at the deepest penetration into cladding [37]. In an alloy system with the presence of lanthanide, the inter-diffusion coefficients and activation energies are both different with those in a system without lanthanide. Fuel smear density and cladding type have significant effects on FCCI. Since the high smear density in the fuel can limit the development of

interconnected porosity, which is believed to accelerate the migration of lanthanide fission products, the fuels with lower smear density thereby have higher lanthanide inventory at the fuel/clad interface, leading to more FCCIs [37].

### 2.3.2 Out-of-Pile Data Analysis

Diffusion couple test is a direct and efficient method to study the diffusion kinetics and chemical reactions of materials. The test is to make solid pieces of pure elements or alloys come into intimate contact and then heat-treat for a period of time, and finally determine the interdiffusion behavior of investigated materials with microstructure characterization analysis. The commonly used microstructure characterization techniques include scanning electron microscope, energy-dispersive spectroscopy, X-ray diffraction, electron probe micro-analysis, wavelength-dispersive spectroscopy, Auger electron spectroscopy, secondary ion mass spectrometry, and Rutherford backscattering spectrometry (Kodentsov, Bastin, & van Loo, 2001). The measured composition profiles serve as a good source for interdiffusion analysis, as long as the heat-treatment temperature and time duration are known.

Iron (Fe) is the balance of HT-9 cladding, its chemical interactions with lanthanide have been broadly studied. On the basis of a diffusion couple test employing mischmetal (70Ce-30La wt.%) and Nd separately coupled with the cladding alloy Fe-9Cr-2W wt.% at 1033 K, it was found Ce and Nd diffused into cladding and formed intermetallics, the diffusion kinetics of which followed the parabolic rate law [38,39]. In the quaternary-Ln alloy/HT-9 diffusion couple, $Ln_2(Fe,Cr)_{17}$ compounds (Ln here include Nd, Ce, Pr and La) were formed by interdiffusion [34]. The formation of intermetallics at equilibrium condition and the solidus temperature of the system can be found in its *phase diagram*, accordingly, the potential intermetallics formed at the fuel/cladding interface during irradiation are presented in the following. In the Nd-Fe system, $Nd_2Fe_{17}$ and $Nd_5Fe_{17}$ compounds were reported [40,41], the solidus temperature of Nd-Fe system is at 955 K with 21.7 at.% Fe [42]. In the Ce-Fe system, there are $CeFe_2$ and $Ce_2Fe_{17}$ compounds formed by peritectic reactions, and an eutectic equilibrium presenting in the Ce-rich side [43,44], the solidus temperature of Ce-Fe system is at 865 K with 16.4 at.% Fe. In the Pr-Fe system, only one compound, $Pr_2Fe_{17}$ was found [45,46], the metastable phase $PrFe_2$ was also reported but only exists under high pressure [47], the solidus temperature is at 940 K with 18 at.% Fe [46]. In the La-Fe system, there is no intermetallic phase at the atmospheric pressure, the solidus temperature is at 1078 K with 11.4 at.% Fe [48]. In summary, the compounds formed in the Ln-Fe systems have these two compounds: $LnFe_2$ and $Ln_2Fe_{17}$; except La-Fe system, the solidus temperature of Nd/Ce/Pr-Fe systems is nearly the same as or even lower than the typical fuel/cladding interface temperature (873-923 K), thus susceptible to liquefy.

Chrome (Cr) is the second major component of HT-9. In the Ln-Cr systems, except for some terminal solid phases, there is no compound; the solidus temperature is higher than the typical fuel/cladding interface temperature [49]. The Ln-Cr binary phase may not form during irradiation, moreover, Cr in HT-9 can slow down the Ln-Fe diffusion to some extent. The alloy Fe-20.1Cr and pure Fe metal showed comparable behaviors in the development of a $CeFe_2$ layer at 865 K, the formation of a ternary $Ce_3(Fe,Cr)_7$ phase was observed due to the presence of Cr in the Fe-20.1Cr/Ce diffusion couple, Cr exhibited the phenomenon of flux reversal at the $Ce_3(Fe,Cr)_7$/Fe interface [50]. The Ce/Fe and Ce/(Fe-Cr-Ni) diffusion couples showed different thicknesses of diffusion layer at 833 K, the thickness decreases with the increasing Cr content, the Cr-rich phase consisted of Fe and Cr was found at the front of Ce diffusion path [51]. Therefore, Cr is susceptible to act as a barrier in the interdiffusion between lanthanide and cladding, and slow down the diffusion kinetics.

There is less than 1 wt.% Ni in alloy HT-9, however, even a small composition may liquefy as the solidus temperature of Ln-Ni systems is even lower than Ln-Fe systems to some extent. In the Nd-Ni system, many compounds ($Nd_3Ni$, $Nd_7Ni_3$, NdNi, $NdNi_2$, $NdNi_3$, $Nd_2Ni_7$, $NdNi_5$ and $Nd_2Ni_{17}$) have been found, the solidus temperature of Nd-Ni system is at 857 K with 33.81 at.% Ni, when the range of Ni content is around 19-38 at.%, the solidus temperature is below 973 K [52,53,54]. In the Ce-Ni system, the compounds include $Ce_7Ni_2$, CeNi, $CeNi_2$, $CeNi_3$, $Ce_2Ni_7$, and $CeNi_5$, the solidus temperature is at 750-756 K with 21.0 at.% Ni [55,56,57]. In the Pr-Ni system, the compounds include $Ni_5Pr$, $Ni_7Pr_2$, $Ni_3Pr$, $Ni_2Pr$, NiPr, $Ni_3Pr_7$ and $NiPr_3$, the solidus temperature is at 822 K with 35.1 at.% Ni [58]. In the La-Ni system, compounds include $La_3Ni$, $La_7Ni_3$, LaNi, $La_2Ni_3$, $La_7Ni_{16}$, $LaNi_3$, $La_2Ni_7$ and $LaNi_5$, the solidus temperature is around 790 K with 35 at.% [59,60,61].

Figure 2 shows the enthalpy of formation of Ln-Ni and Ln-Fe systems. Enthalpy of formation represents the thermodynamic stability of compounds and the driving force of compound formation. They are all negative, indicating the potential formation of compounds. Ln-Ni compounds and solid phases will be easy to form and grow as the enthalpy of formation is very negative.

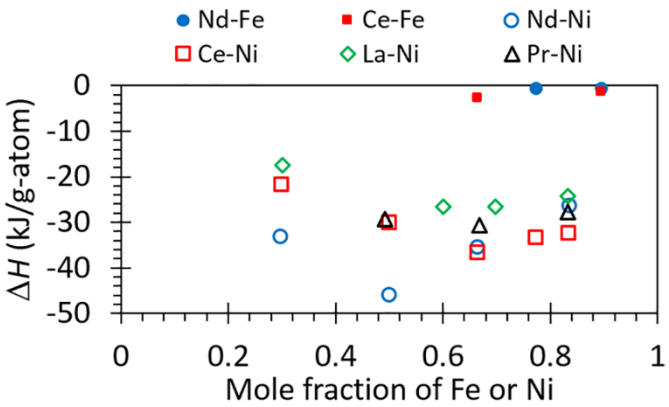


**Figure 2 Enthalpy of formation (kJ/g-atom) at 298 K for Ln-Fe and Ln-Ni systems (Ln = Nd, Ce, Pr and La).**

## 2.4 Ln Migration Theory

Lanthanides at the fuel periphery play important roles in FCCI. During irradiation, lanthanides are generated in fuel, their precipitates at the outer region of fuel and layers of cladding indicate the migration. There are three theories that potentially explain lanthanide migration: solid phase diffusion, vapor phase transport, and "liquid like" transport.

Solid phase diffusion theory suggests that lanthanide can migrate in fuel through solid-state diffusion, the driving force is the gradients of concentration and temperature. Fundamental data, such as lanthanide solubility and diffusion coefficient are required to estimate the lanthanide migration in the solid fuel matrix. These fundamental data are also dependent on the constituent redistribution during burnup [30]. The diffusion coefficient of Ce in U-Zr solid solution has been measured, which is $2\times10^{-13}$ $m^2/s$ at 1123 K and $6\times10^{-14}$ $m^2/s$ at 1023 K [62], since Ce is one of the main compositions of lanthanide fission products, its diffusion behavior is representative. However, these diffusion coefficients are too low, in other words, the solid diffusivity of lanthanide in fuel matrix is extremely small. This is contrary to the actual lanthanide migration, as suggested by the fast interaction of fuel and cladding at 5 at.% burnup, the actual lanthanide migration is rapid. Accordingly, the solid phase diffusion theory is in doubt to explain the rapid migration process, which must be determined by some other factors.

The vapor transport theory comes up to explain the rapid transport process [63]. The theory is based on the facts that lanthanide can migrate through vapor transport via a network of interconnected porosity even at a very low burnup, the vapor that transports down the temperature gradient to the cladding is attributed to a gradient in fission product vapor pressure from the fuel center to the surface [12]. However, this theory fails in explaining several observations of fuel [31]. An example is that both Ce and Sm was observed to migrate in spite of a large difference between the vapor pressures of

these two elements (approximately eleven orders of magnitude apart) [31]. To more accurately describe the dominant transport mechanism for lanthanide migration, a reverse theory is needed.

The “liquid-like” transport mechanism [31] has been proposed. Recently a ‘liquid-like’ transport mechanism has been proposed for the migration of the lanthanides in U-Zr fuel. This theory suggests the interconnected pores containing liquid cesium and liquid sodium, which has intruded through the interconnected porosity from the gap, allows for a faster ‘liquid-like’ transport of the lanthanides to the gap. One aspect of this migration is the lanthanides can be transported as solutes in the liquid cesium and the liquid sodium. Thus the liquid alkalis in the pores can transport the lanthanide solute from the interior of the fuel through the interconnected pores to the periphery. Once at the periphery the lanthanides precipitate out of the liquid alkali metal as metal slugs on the peripheral of the fuel. A schematic of the ‘liquid-like’ transport mechanism is shown in Figure 3.

The “liquid-like” transport indicates that lanthanides are transported through liquid Cs and Na, and it can explain the lanthanide distribution, precipitation and the rapid migration process. The first contribution to the liquid-like transport is the liquid Cs and Na filling the interconnected pores and fissures of fuel. Fuel swelling creates pores and fissures. Cesium (Cs) as a low melting temperature fission product with low solubility in fuel matrix, accumulates in the pores and fissures. Sodium (Na) is a liquid fuel/cladding-gap-filler metal, and fills the porosity of fuel surface. Cs and Na together connects the porosity throughout the fuel, being a path to transport lanthanide. In liquid metals, the solubility of lanthanide decreases with decreasing temperature [64], and is lower in liquid Na than in Cs [65], accordingly explains the lanthanide precipitation at the fuel and cladding surfaces.

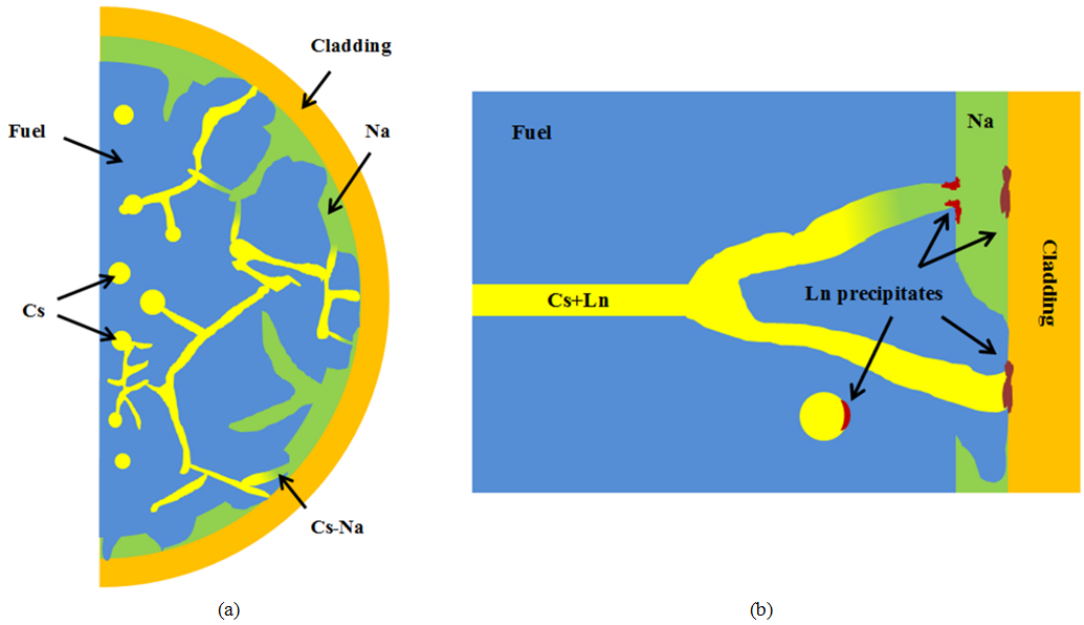


**Figure 3. Schematic of 'liquid-like' transport mechanism of lanthanides through the interconnected porosity to the gap between fuel and cladding.**

The other contribution to the liquid-like transport is the abundance of surface area on the pores and fissures of fuel. Since lanthanide has low solid-solubility in the fuel matrix, lanthanide would be expressed from the fuel matrix over time, owing to substantial kinetic energy available from locally high temperature and burnup. Once on the surface of pores, where the lanthanide surface states are weakly bound, lanthanide migration toward the cladding surface will be much more rapid than the solid-solid diffusion would allow. Once the lanthanide contacts cladding, a strong chemical interaction occurs. Thus, once on the fuel periphery, their transport to colder axial zones is also halted. This mode of transport would be enhanced by the presence of liquid Cs, as suggested by the moderate solubility of dysprosium (Dy) in Cs. Further, this mode of transport underscores how vapor phase transport is very unlikely; specifically, vapor phase lanthanide would tend to be more uniform (or disposed to colder regions) because of vapor mobility and immediate strong chemical interaction that pins the lanthanide on the cladding.

The precipitation of the lanthanides at the periphery of the fuel can be explained by the temperature gradient in the fuel and by the liquid alkali metals. Typically, in liquid metals, the solubility of other metals, such as lanthanides, decreases with decreasing temperature. Thus the amount of lanthanides which can dissolve in the liquid alkalis at the interior of the fuel should be higher than the concentration of the lanthanides which may be dissolved at the periphery due to the solubility difference from the temperature gradient of the fuel.

The other aspect of the precipitation at the periphery is based on the concentration of cesium and sodium in the liquid alkali metal solution at the pores and gap. At the interior of the fuel, the liquid alkali metal solution in the pores should have a higher concentration of cesium than sodium. This is due to the cesium being produced as a fission product in this region and preferentially existing in the open space of the pores due to the low solubility in the U-Zr matrix. On the other hand, the sodium has to intrude from the gap through the tortuosity of the interconnected porosity. However, at the peripheral of the fuel, near the gap, it would be expected to have a considerably higher concentration of sodium than cesium, as this is the region which the bond sodium originated. Based on general trends in solubility in liquid sodium and liquid cesium, the solubility in liquid cesium is expected to be considerably higher than in liquid sodium. Based simply on the concentration of cesium and sodium in the liquid alkali metal, there is expected to be a higher concentration of lanthanide solutes in the liquid alkali metal at the interior of the fuel than at the peripheral.

The precipitation of the lanthanide slugs at the periphery of the fuel can be also explained by this combination of the temperature gradient and the concentration difference of cesium and sodium. Both the temperature gradient and the alkali concentration suggest a higher lanthanide solute concentration in the liquid alkali metal at the interior of the fuel's pores than at the periphery. Thus as lanthanide solutes migrate away from the lanthanide precipitates at the interior fuel pores, their solubility in the liquid alkali metal decreases. Upon reaching the peripheral of the fuel, the lanthanide concentration transported from the interior of the fuel is above solubility of the liquid alkali at the gap. This saturation of lanthanide results in a fast precipitation and the formation of the slug-like precipitates as found at the peripheral of the fuel.

The "liquid like" transport theory has been validated through experimental measurements [8] and modeling simulations [66] (these two references are publications of the present study). Investigations were focused on lanthanide solubility and diffusivity in liquid Cs, Na and Na-Cs mixtures. Solubility of Nd, Ce and La in the liquids were measured at different temperatures [8]. One example of solubility of Nd in the liquids is shown in Figure 4. It indicates that the Nd solubility in liquid Cs is much higher than that in Na. At 723 K, the solubility in Cs is more than two orders larger than that in Na, the temperature drop also makes solubility decreases in orders (Figure 4a). In the liquid Na-Cs mixture, the solubility decreases with the increase of Na concentration (Figure 4b). Under irradiation, the concentration of Cs in the interconnected pores and fissures is higher in the fuel interior region than the outer as Cs is produced as a fission product and the amount is affected by burnup; meanwhile, the concentration of Na in the outer region is higher than Cs, considering Na is the gap filler. Accordingly, lanthanides produced during irradiation primarily dissolve in the liquid Cs, and then transport outside driven by the concentration gradient. With the

increase of Na in the outer region, lanthanides become difficult to dissolve and thus precipitate. As observed on the fuel surface, lanthanide precipitates have an appearance of "sludge-like", indicating swift solidification with no exhibition of crystal characteristics [31], this is in contrast to other fission product precipitates with uniformly shaped cubic structures [ 67 ]. These behaviors indicate lanthanide precipitation is a rapid process, the sudden drop of solubility caused by the increase of Na concentration and the decrease of temperature cannot afford enough time for lanthanides to form a crystal structure.

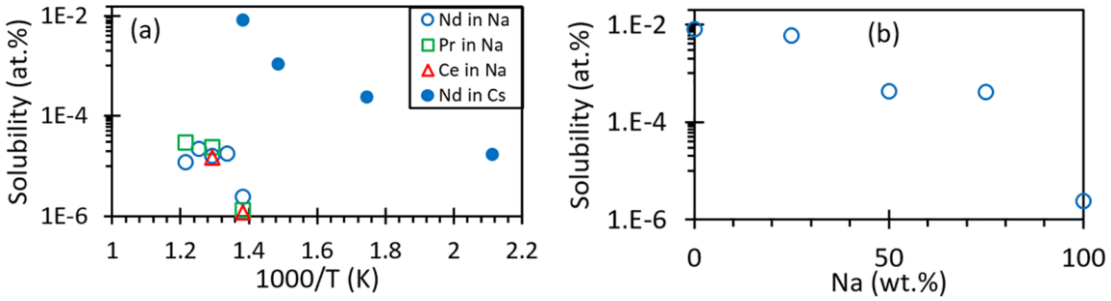


**Figure 4 (a) solubility of Nd, Pr and Ce in liquid Na and liquid Cs at different temperatures, (b) solubility of Nd in liquid Cs-Na mixtures at 723 K [8].**

The lanthanides that migrate to the fuel surface have two ways to transport to the cladding surface, one is *fuel swelling that makes lanthanide-cladding directly contacted*, the other is *lanthanide diffusion through the Na-filled gap*. A simulation model based on *ab-initio* molecular dynamics has been developed to calculate the diffusion coefficients of Nd, Ce and Pr in liquid Na and Cs [66,68]. Results are summarized in

Figure 5. Diffusion coefficients (obtained in the present study) are in the order of $10^{-5}$ $cm^2/s$. The diffusion coefficient of a give lanthanide is always higher in liquid Na than Cs, the higher diffusion coefficient in liquid Na makes it possible for lanthanides to pass through the Na-filled gap. The diffusion coefficient decreases with decreasing temperature, so the lanthanide will finally deposit on the cladding surface. The simulation using BISION code showed the transport of lanthanide from the fuel center to the edge through Cs-filled cracks, and the deposition of lanthanide on fuel and cladding surfaces [66].

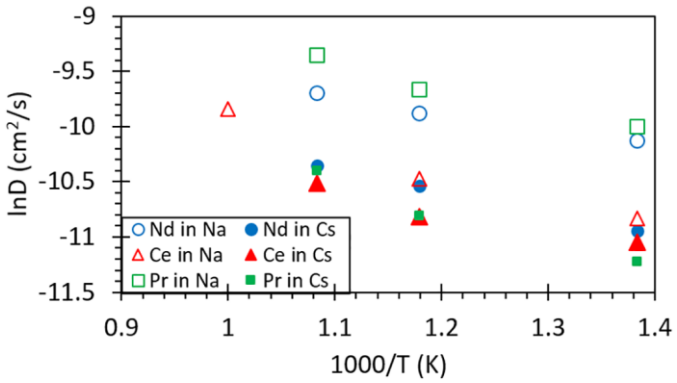


**Figure 5 Diffusion coefficients of Nd, Ce and Pr in liquid Na and Cs [66].**

In summary, lanthanides primarily dissolve in the liquid Cs-filled pores and fissures of fuel, transport from the inner region to the outer driven by concentration and temperature gradients, some of them rapidly precipitate in the fuel outer region (note the "sludge-like" lanthanide precipitates) because of the sudden drop of solubility caused by the increase of liquid Na concentration. The lanthanides on the fuel surface will either directly contact with cladding by fuel swelling, or deposit on cladding through diffusion in the Na-filled gap.

# 3. Review on Available Solubility Measurements

## 3.1 Previous Experimental Techniques

The reactivity of the alkali metals and the miniscule concentration of the typical solubility cause several limitations in experimentally determining the solubility of metals in liquid alkali metals. These limitations have resulted in several prominent experimental methods being traditionally used. The methods include a dipping sampling method [69] [70], a pressure driven sampling method [71] [72], and an inversion crucible method [73] [74]. All of these methods are typically performed in an inert gas filled glovebox with the oxygen and water concentrations controlled.

Dipping Sampling Method

The dipping sampling method is setup with a bath of liquid alkali metal within a furnace. A solute piece of the metal of interest is added to the liquid alkali bath. The bath is closed and the temperature of interest is maintained for a time period to allow the solution to reach equilibrium. After equilibrium has been reached, the lid of the bath is removed and a sampling cup is manually dipped into the bath to remove a liquid alkali sample. The bath is then raised in temperature and this process is repeated over a range of temperatures. In addition to the problems associated with having an open high temperature alkali bath when sampling, the bath must be stirred to ensure the area sampled will be representative of the entire solution. Issues have previously been reported of this stirrer acting as a mass transfer [70].

Pressure Driven Sampling

A similar technique to the dipping method is a pressure driven sampling method. This method allows a large bath of liquid alkali metal to equilibrate with a solute. Once equilibrium is reached, instead of sampling manually by dipping a sampling cup, the sample is taken from the bath with a tube inserted into the bath. The tubing apparatus transports the sample from the bath to a sampling container by a pressure gradient to create suction. The bath is then equilibrated at a higher temperature and the sampling is repeated into a different sampling container. This process is then repeated over a range of temperatures. This method is most commonly performed at lower temperatures where glass can be used for the tubing in the pressure driven sampling system. Unlike the dipping sampling method this method does not typically contain a stirring mechanism. This reduces the issues associated with possible mass transfer described in the dipping sampling method. However, the lack of mixing has been identified as a possible source of error within the solubility measurements [72].

Inversion Crucible

Another commonly used method is the "inversion crucible" method [75]. This technique places a solute piece and a small amount of liquid alkali metal within a small-enclosed cylindrical crucible. This crucible is placed in a furnace, heated and maintained at the temperature of interest. After equilibration, the crucible is inverted for gravity to drive the flow of the liquid solution from one end of the crucible, through a filter, to the other end of the crucible. This creates a sample at the new end of the crucible while the solute is left behind at the filter. While only a small amount of alkali metal and solute is needed for each test, this method loses the continuity across temperatures associated with the sampling from the same bath in the other techniques.

It was decided to perform solubility experiments using the inversion crucible method. One reason for this decision was due to the issues in having an open high temperature liquid alkali bath. Another was to test multiple alkali solution concentrations. In using smaller bath sample sizes more tests could be performed by either varying the solute used or the concentration of sodium or cesium in the liquid solution.

## 3.2 Previous Experimental Data

One of the few solubility experiments involving lanthanides was conducted and published by Lamprecht [76]. This experiment investigated the solubility of cerium in liquid sodium using a version of the pressure driven sampling method and the radioisotope Ce-141. This work experimentally studied the cerium solubility from 130˚C to 450˚C and the solubility ranged from $2.8 \times 10^{-7}$ to $1.4 \times 10^{-6}$ at. %. One interesting note from the results was there was a slightly negative temperature dependence of the solubility. This negative temperature dependence is unexpected for most metals in liquid sodium [77]. The authors suggested this negative dependence was due to the reference cerium probably being $Ce_2O_3$ instead of metallic cerium due to a high oxygen concentration in their experiment. Another previous work found the solubility of cerium in liquid sodium at 700˚C was near their detection limit of 10-4 at. % [78]. It was concluded the solubility was not much below this and the solution had reached equilibrium prior to 5 hours.

As for the interaction between the lanthanides and cesium, a previous experimental work from Griffin investigated the interaction of cesium and praseodymium [79]. Griffin's work focused on the praseodymium-rich alloys and studied the change of transformation temperatures with the addition of cesium. It also reported finding cesium formed an immiscible liquid with praseodymium. This study was the basis for a partly speculative phase diagram of cesium-praseodymium [80]. The speculated phase diagram shows both elements have no mutual solubility as solids and in the liquid state they are nearly immiscible. In this tentative phase diagram, the solubility of praseodymium in liquid cesium was up to about 9 at. % at the praseodymium melting

temperature. However, the solubility line of praseodymium in liquid cesium has been predicted to be much lower than this original speculative line based on general trends of the solubility of metals in various liquid alkali metals [81]. This revision concluded the solubility of praseodymium in liquid cesium might not be higher than 1 at. % at the praseodymium melting temperature and is shown in Figure 6.

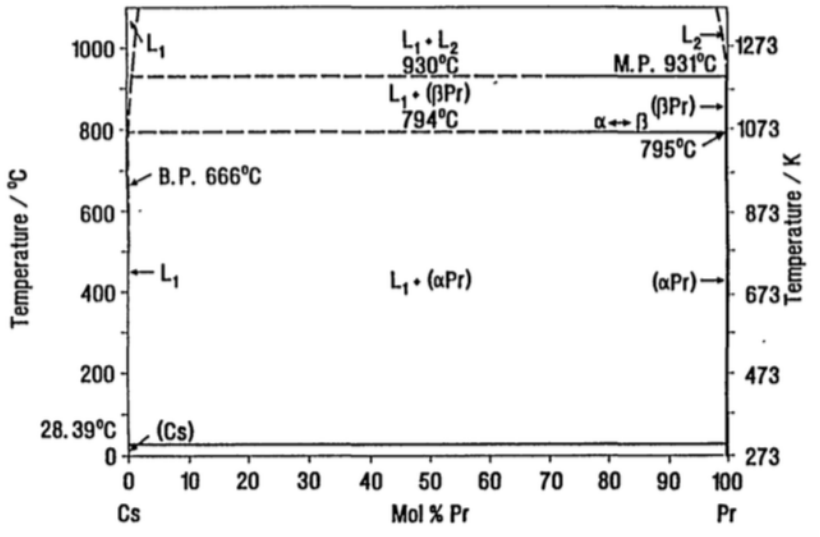


**Figure 6. Cs-Pr Phase Diagram**.

The chemical properties of the elements within the alkali group, like sodium and cesium, have been shown in general to be very similar [82]. The binary phase diagrams of the alkali metals with both the transition metals and the rare earth elements have been typically characterized by the lack of intermediate phases and having large regions of immiscibility. The elements in the row of lanthanides also show considerable chemical and physical similarity with one another, especially between adjacent elements. This is due to the relatively small radial extension of the 4f electron orbitals and its effect on chemical bonding changes little between adjacent elements [82].

# 4. Experimental Solubility Results

## 4.1 Experimental Procedure

To measure the solubility, the inversion crucible technique was used. In this method cylindrical crucibles of either stainless steel 304 or tantalum of 3" in length and ¾" in diameter were used. These cylinders were capped at one end and approximately 2 grams of solid alkali metal and a 2-gram piece of lanthanide were placed within the cap. The lanthanide pieces of cerium, praseodymium, and neodymium were acquired from ESPI Metals and had a purity of 99.9 %. For the alkali metals, ESPI Metals supplied the sodium metal with a purity of 99.95% and the cesium metal was from Alfa Aesar with a purity of 99.98%. The experiments were performed within a glovebox filled with argon gas and maintained $O_2$ and $H_2O$ concentrations below 3 parts per million throughout testing.

The alkali metal and the lanthanide piece were placed within one cap of the cylindrical crucible, a metal mesh was inserted approximately halfway in the cylindrical tube. This metal mesh, made from the same material as the crucible and with a mesh sieve of 300-µm, would act as a filter within the experiment. After inserting the mesh, the open end of the crucible was capped and labeled the collector, creating an enclosed crucible. On the left of Figure 7 is an experiment using an enclosed stainless steel crucible while the right is a schematic of the inside of the enclosed crucible.

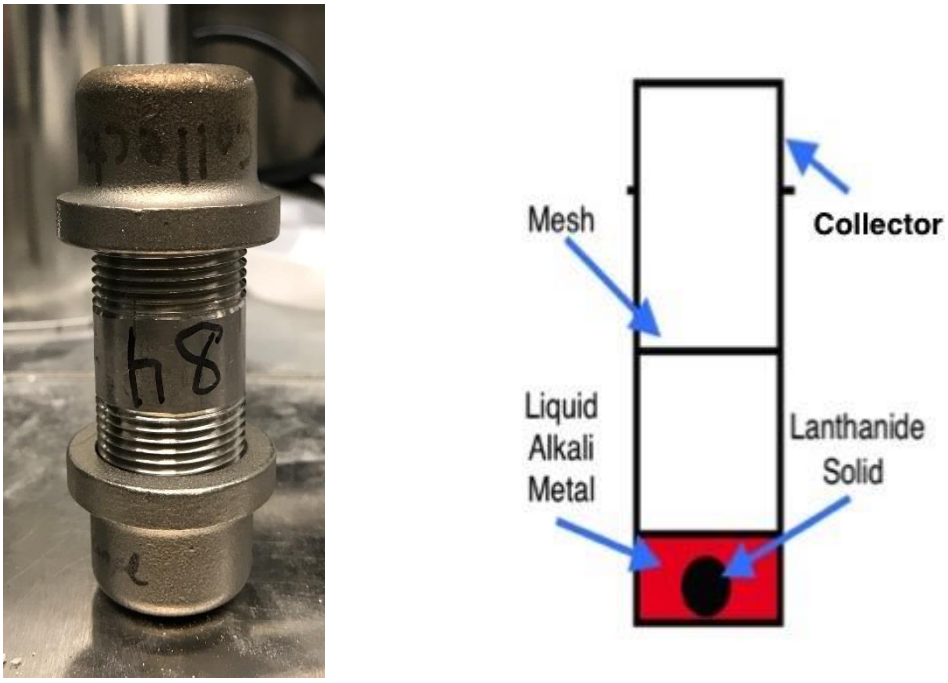


**Figure 7. Solubility Experiment with stainless steel crucible (Left: Experimental Test crucible; Right: Schematic of experimental test setup)**

The closed crucible was then placed within a furnace with the end containing the alkali metal and lanthanide at the bottom of crucible, in the configuration shown in the right image of Figure 7. The furnace was heated to the temperature of interest to melt the alkali metal. This temperature was then maintained for an equilibration time, a set time to allow the system of the liquid alkali metal and lanthanide solid to reach equilibrium. At the equilibration time the crucible was inverted 180˚, end for end, and a schematic of this new configuration is shown in Figure 8.

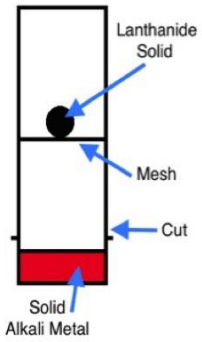


**Figure 8. Schematic of experimental solubility test after inversion.**

This inversion of the crucible causes the liquid alkali to flow from one end of the crucible to the collector due to gravity. As the liquid alkali flows to the collector, it flows through the mesh in the crucible, which acts as a filter. The mesh prevents the solid lanthanide piece from reaching the collector. By separating the solid lanthanide piece from the liquid alkali at the mesh, the liquid alkali in the collector has a lanthanide concentration representing the solubility in the liquid alkali at that temperature.

After the inversion was completed, the furnace was turned off and the crucible was furnace cooled to solidify the alkali metal. Once at room temperature the crucible was dismantled and the collector containing the solid alkali metal, with a lanthanide concentration of the solubility, was analyzed. The collector was removed from the glovebox and isopropyl alcohol was added to the collector to neutralize the alkali metal. This neutralized alkali metal was then prepared and analyzed by Inductively Coupled Plasma – Mass Spectroscopy (ICP-MS).

## 4.2 Impurity Concentration

The impurity concentration of various elements in the alkali metals received from the manufacturer was determined using the same analytical procedure for analysis as the solubility tests. In Table 1 is the average impurity concentration of several elements in

the alkali metals as determined by ICP-MS.

**Table 1. Average impurity concentrations in received alkali metals.**

| | Sodium (at. %) | Cesium (at. %) |
|---|---|---|
| Cerium | $1.9 \times 10^{-7}$ | $2.0 \times 10^{-7}$ |
| Praseodymium | $0.61 \times 10^{-7}$ | $2.4 \times 10^{-7}$ |
| Neodymium | $2.2 \times 10^{-7}$ | $6.0 \times 10^{-7}$ |
| Iron | $9.1 \times 10^{-5}$ | $10. \times 10^{-5}$ |
| Nickel | $1.6 \times 10^{-5}$ | $0.77 \times 10^{-5}$ |
| Chromium | $5.3 \times 10^{-5}$ | $3.0 \times 10^{-5}$ |

Table 1 shows the lanthanides of interest are approximately 0.61 to $6.0 \times 10^{-7}$ at. % in both alkali metals while the elements of the crucible material show a significantly higher concentration in the received alkali metals than lanthanides. As the focus of the thesis is the lanthanide concentration it is advantageous for them to have the lowest impurity concentrations.

## 4.3 Time Dependence

To determine the equilibration time, the concentration of neodymium in liquid sodium and in liquid cesium was measured as a function of time the sample was heated. Samples were allowed to remain in the furnace between 1 and 72 hours at their lowest temperature of interest, liquid cesium was 200˚C and liquid sodium was 450˚C. When a constant concentration was reached this was considered the equilibration time, the time for the solubility concentration.

Figure 9 of the time dependence of the concentration of neodymium in liquid sodium at 450˚C shows the data forms two regions: one around the impurity concentration of the received alkali metal and another region at the elevated concentration of $3.8 \times 10^{-6}$ at. %. The lower concentration region of data consists of 3 tests, which are all within the standard deviation of the average impurity concentration. These concentrations suggest failed tests, as they were the only tests without increased concentrations of neodymium. As some of the first experimental tests conducted this was thought to have played a role in their failure. It was noticed at the conclusion of these tests more sodium was found at the mesh than in the other tests. In subsequent tests, during inversion, the crucibles were slightly jiggled to agitate the liquid and allowing it to pass through the filter easier. Subsequent tests with agitation showed only a miniscule amount of sodium at the mesh and greater consistency in the concentration measurements. The surface tension of some of the lighter liquid alkalis has been shown previously to cause issues in the passing of the liquid through the metal mesh and alterations such as the added

agitations were necessary [ 83 ]. From this data it was concluded the elevated concentration represented the actual solubility and was used in the determination of the equilibration time.

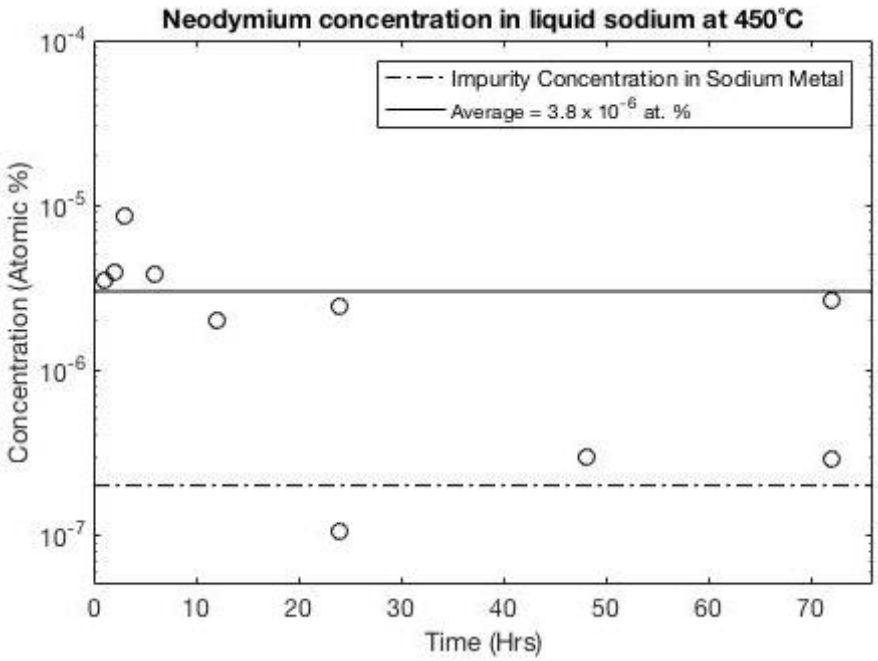


**Figure 9. Time dependence of neodymium concentration in liquid sodium at 450 ˚C.**

Figure 9 shows a relatively constant concentration with equilibration time between 1 and 72 hours at this elevated concentration. This constant concentration suggests that the solubility concentration was reached prior to 1 hour. The constant concentration in Figure 9 was used to calculate the solubility of neodymium in liquid sodium at 450˚C to be $3.8 \times 10^{-6}$ at. % $\pm$ $2.0 \times 10^{-6}$ at. %.

Figure 10 shows the time dependence of neodymium in liquid cesium at 200˚C. Similarly to the liquid sodium results in Figure 10, the concentration results are relatively constant over the time frame. This shows the solubility concentration in liquid cesium is reached prior to 0.5 hours. Using the data from Figure 10 the average solubility of neodymium in liquid cesium at 200˚C is $1.7 \times 10^{-5}$ at. % $\pm$ $0.5 \times 10^{-5}$ at. %.

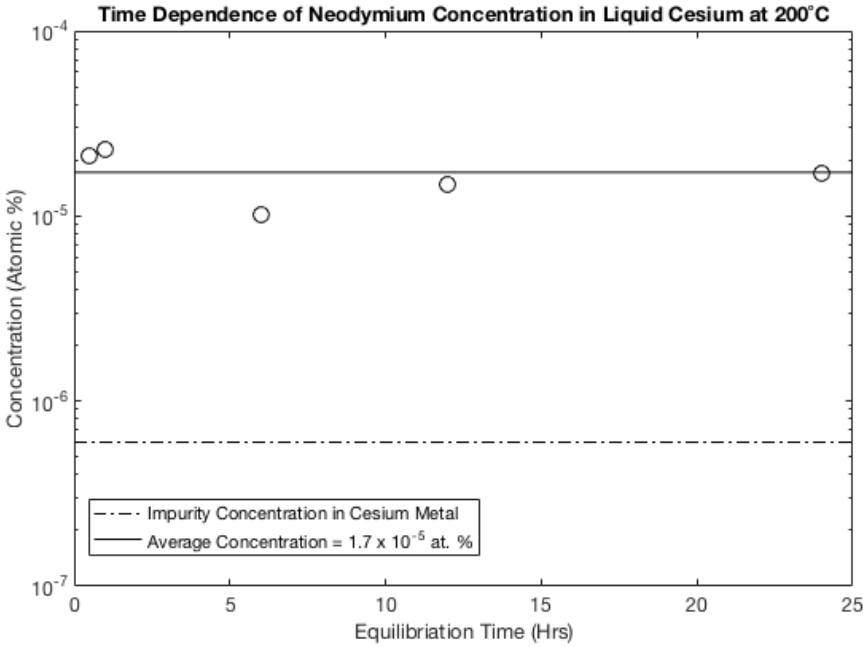


**Figure 10. Time dependence of neodymium concentration in liquid cesium at 200˚C**

While the lowest temperature tested for both the liquid alkali metals reached their solubility concentrations prior to 1 hour, 24 hours was used as the equilibration time. This equilibration time was chosen to ensure equilibrium was reached and to provide consistency throughout experiments. In addition, an equilibration time of 24 hours has been previously shown to be adequate for equilibration by previous liquid alkali metal solubility tests [73] [84]. Unless noted, the data shown through the rest of this chapter is for tests conducted at 24 hours.

## 4.4 Temperature Dependence

The solubility of lanthanides in liquid sodium was tested over the temperature range of 450 to 550˚C. Figure 11 shows the temperature dependence of the lanthanides in liquid sodium.

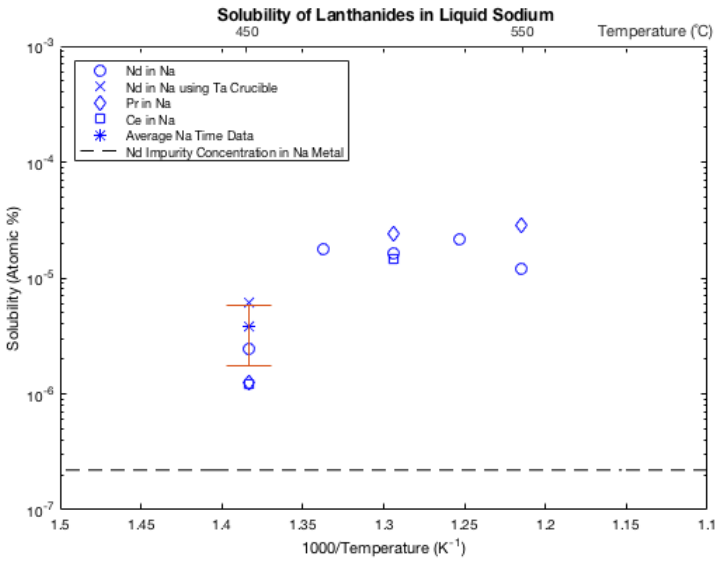


**Figure 11. Temperature dependence of lanthanides in liquid sodium.**

Figure 11 shows approximately an order of magnitude increase in solubility across the temperature range. However, this difference is solely due to the data at 450˚C as the rest of the data shows negligible temperature dependence. Thus while the data as a set shows an increase of the solubility with temperature, the conservative statement is the solubility temperature is within the range of $1 \times 10^{-6}$ to $2.5 \times 10^{-5}$ at. % for the lanthanides in liquid sodium in the range of 450 to 550˚C.

While the data of cerium and praseodymium is more limited than neodymium, it shows good agreement with the neodymium data. At 450˚C, the cerium and praseodymium data is just outside the standard deviation for neodymium based on the time dependent data. The cerium and praseodymium data at the elevated temperatures showed nearly the same deviation from the neodymium data as at 450˚C. With the agreement between the lanthanides data and the knowledge the lighter lanthanides have similar chemical properties [82], the solubility tests in the other liquid alkalis focused on neodymium to be representative of the lanthanides.

The experimental data of the solubility of neodymium in liquid cesium between 200˚C to 450˚C is shown in Figure 12. Due to the loss of liquid cesium from the crucible as gas at elevated temperatures, a maximum of 450˚C was used in liquid cesium testing.

Unlike the liquid sodium results, Figure 12 shows a clear trend of increasing neodymium solubility in liquid cesium over the temperature range of study. The data suggests an increase in solubility of neodymium from 200 to 450˚C of slightly less than 3 orders of magnitude. The fit of the data for the solubility of neodymium in liquid cesium from 200 to 450˚C is shown in Equation (1).

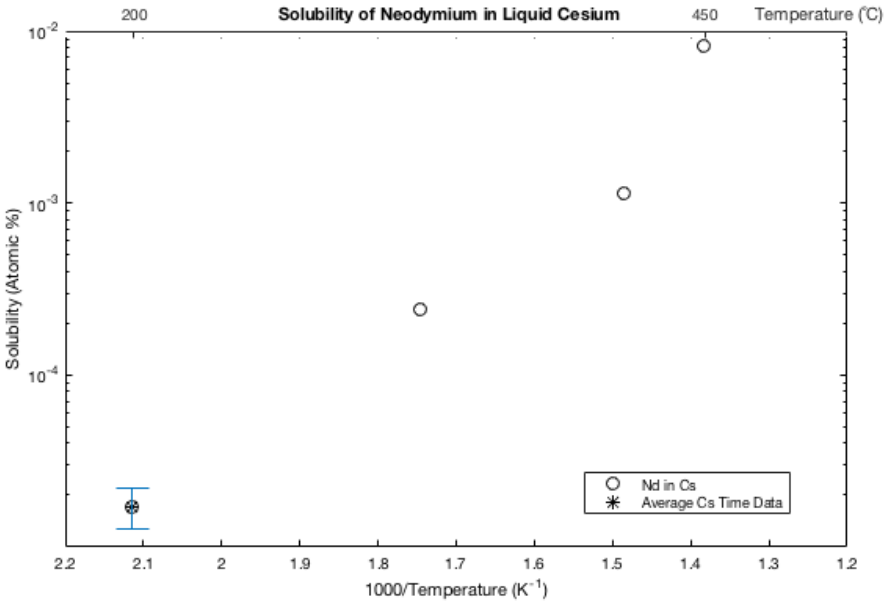


**Figure 12. Temperature dependence of neodymium in liquid cesium.**

$$\ln X_{Nd\ in\ Cs}\ (at.\%) = \ 5.502 - \frac{7864}{T(K)} \qquad (1)$$

The fit in Equation (1) had a $R^2$ of 0.966. Based on this fit in Equation (1) the excess partial molar entropy is $45.74J/(K\ mol)$ and the excess partial molar enthalpy is $65.39kJ/mol$.

Figure 13 provides the temperature dependent solubility data in both liquid alkalis to provide a comprehensive comparison. The averages and the standard deviations of the data in the time dependent tests are included. All the other results included were taken after allowing the tests to equilibrate for 24 hours. Included in Figure 13 are the also the previous results from the experimental solubility of cerium in liquid sodium [76] [78].

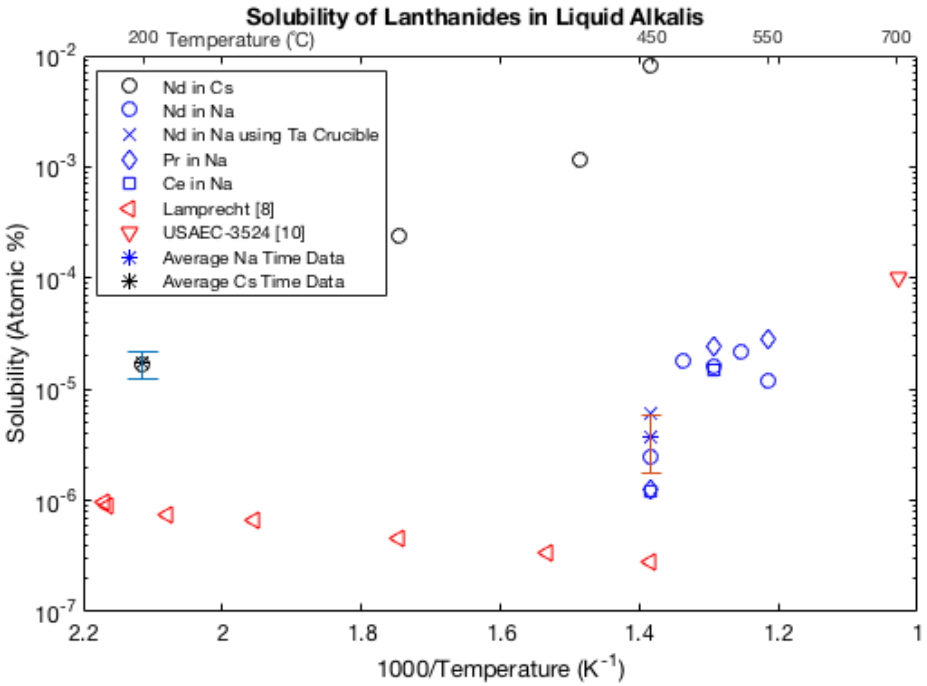


**Figure 13. Experimental solubility results for both liquid sodium and liquid cesium.**

There are several points to be taken from Figure 13. For the purposes of this thesis the most important is the difference in solubility in the liquid cesium compared to the liquid sodium. The solubility at 200˚C in liquid cesium is approximately the order of magnitude in liquid sodium at the elevated temperature of 550˚C. The strong temperature dependence of solubility in the liquid cesium results in the solubility difference being evident between the two liquid alkalis at 450˚C.

Another aspect is the uncertainty associated with the time dependence test results. The standard deviation associated with the liquid sodium tests is a greater fraction of the average value than the liquid cesium tests. The reason for this difference is traced back to the lower concentration measured in the liquid sodium. The standard deviation from the time dependence tests for the liquid cesium, at $5 \times 10^{-6}$ at. %, was actually greater than the liquid sodium results, $2 \times 10^{-6}$ at. %. While the deviation in Figure 13 appears larger for the liquid sodium, this is simply due to the effect of the log plot.

Figure 13 also shows the cerium in liquid sodium experimental data from previous works [76] [78]. The data from this thesis lies in the temperature regime between these works and subsequently the solubility measured is between these two works. The expected temperature dependence of lanthanides in liquid sodium is lacking in each of the individual works for various reasons. However, when the three experiments are viewed together, the increasing trend of solubility with temperature is noticeable.

## 4.5 Concentration Dependence

The solubility of neodymium in liquid alkali metal was also investigated based on the concentration of sodium or cesium in the liquid alkali solution. Figure 14 shows the change of solubility of neodymium at 450˚C with the increasing of sodium in the liquid alkali metal solution.

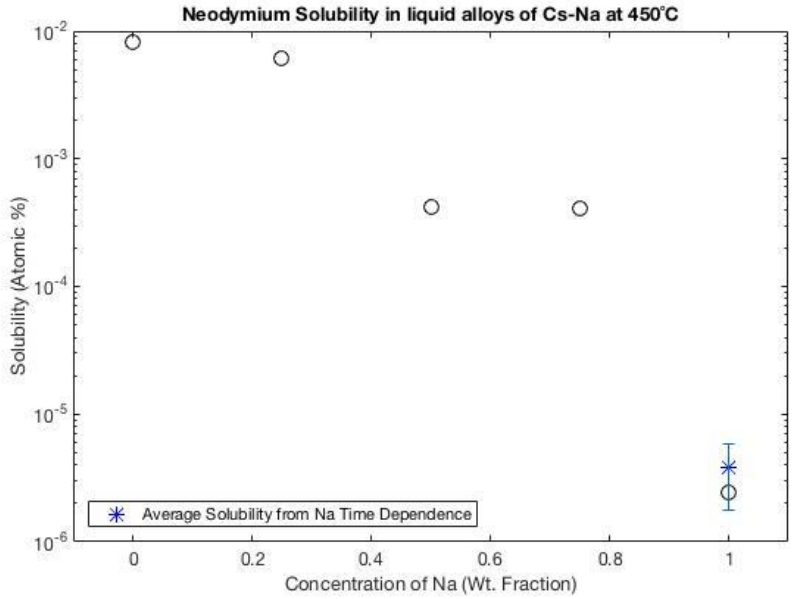


**Figure 14. Solubility of neodymium at 450˚C in liquid alkali mixtures.**

Figure 14 shows a continual drop in the neodymium solubility with the increase of sodium in the mixture of sodium and cesium. The drop is most obvious when comparing the solubility of the pure liquid cesium to the pure liquid sodium with the solubility decreasing nearly 3 orders of magnitude.

## 4.6 Control Tests

To provide a control group in this experiment, tests were conducted without a lanthanide solute but with liquid sodium. These tests were conducted identically to the previous tests but without a lanthanide solute piece added to the test. In these tests, the concentrations of crucible materials and lanthanides were analyzed. The lanthanide concentrations could then be compared to help ensure the concentration measured previously was due to the lanthanide solute rather than other factors. Also the major components of the stainless steel cladding could be tested for their concentration in this method and compared to previous literature solubility works to investigate the

crucible's effect on the liquid alkali metal solution.
Shown in Figure 15 is the comparison of the lanthanide concentrations in tests with and without lanthanide solutes.

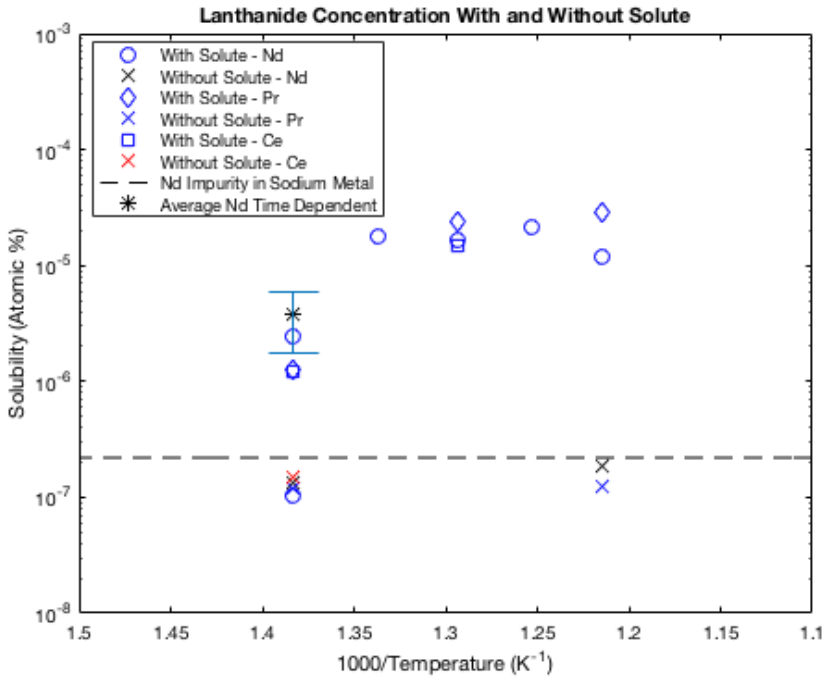


**Figure 15. Lanthanide concentration in tests with and without solute piece.**

As expected the tests with solutes all show increased lanthanide concentrations compared to the tests conducted without solutes, with the exception of one of the early time dependent tests discussed earlier. In addition, the majority of the tests without solutes were at or below the concentration of the impurity of neodymium in the received sodium. Figure 15 also provides additional evidence for the failure of the early non-agitated tests as the one conducted at 24 hours has the same neodymium concentration as a test without a solute.

In tests without solute pieces the concentrations of the three major elements of the stainless steel crucible (iron, chromium and nickel) were measured. This inversion crucible method of measuring the crucible element concentrations in the sodium was how many of the previous solubility experiments were performed [84]. Shown in Figure 16, Figure 17, and Figure 18 are the measurements for these three elements compared to previously published solubility data.

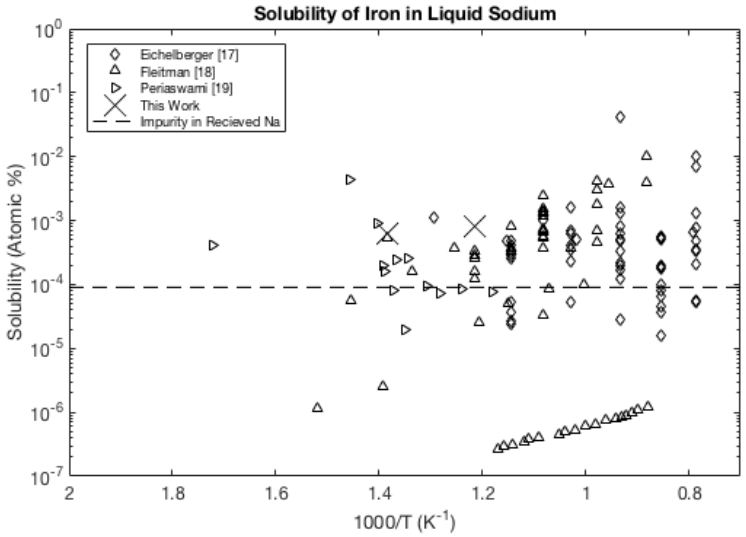


**Figure 16. Concentration of iron in tests without a solute piece compared to previous experimental solubility tests.**

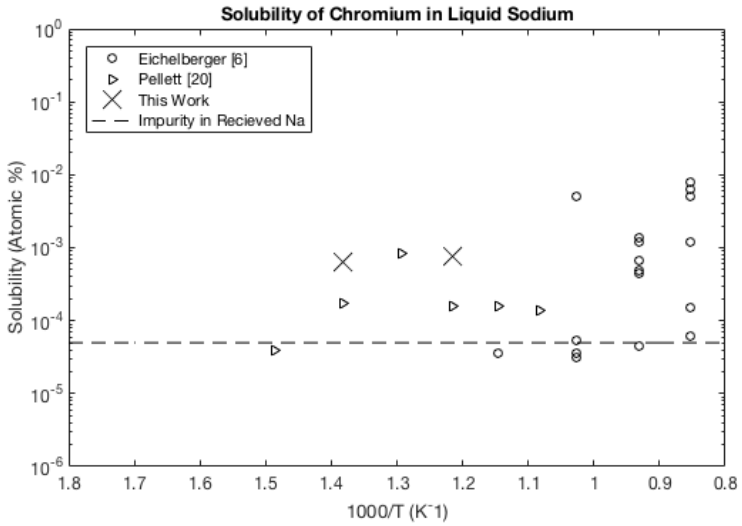


**Figure 17. Concentration of chromium in tests without a solute piece compared to previous experimental solubility tests.**

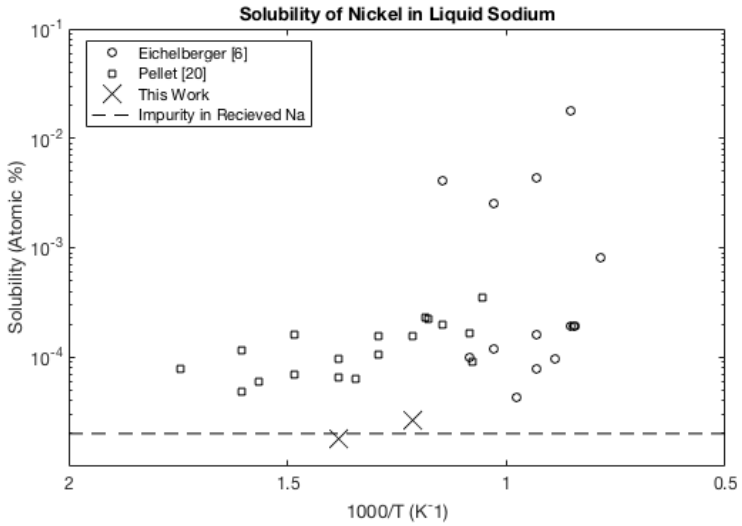


**Figure 18. Concentration of nickel in tests without a solute piece compared to previous experimental solubility tests**

For iron and chromium, the concentrations measured in this work are within the scatter of previous experimental solubility data. These elements show an increase in concentration from the impurity concentration in the received sodium used in this thesis and thus the crucible appears to have caused them to reach their solubility in the liquid sodium. Nickel shows no increase from the impurity concentration and is lower than the solubility experiments for nickel in liquid sodium. As nickel has a smaller concentration within the crucible (8-12 %) compared to chromium (18-20 %) or iron (64 - 70 %) it is logical the nickel's concentration would increase the least in the liquid sodium.

# 5. Phase Diagram Optimization

## 5.1 Differential Scanning Calorimetery (DSC) Procedure

Neodymium powders were acquired from Alfa Aesar with a purity of 99.9% and tin powder, acquired from Strem Chemicals Inc., had a purity of 99.999%. The sodium and cesium used in this section were previously described in the section on experimental solubility experiments. Due to the reactivity of the alkali metals, samples for DSC testing were made within the argon filled glovebox. Samples were made with either a mixture of sodium and tin, sodium and neodymium, or cesium and neodymium with the concentration of the reactants known for each sample. The samples weights were recorded and were within the range of 3 to 20 mg. Prepared samples were then placed within aluminum crucibles and the crucibles were hermetically sealed. This allowed the reactants to remain in an inert environment throughout preparation and experimentation. Upon ensuring the crucibles were sealed, they were removed from the glovebox to be used in the DSC instrumentation.

Prior to testing, the DSC instrumentation was calibrated using the classical three-step procedure of calibrating the heat flow rate baseline, calibrating with a known substance's heat capacity and then calibrating temperature with several known substances. For each crucible, the sample was placed in the DSC and tested against a reference empty aluminum crucible. With a heating rate of 10 ˚C/min, three heating cycles were conducted for each test, with three tests completed per sample. Each heating cycle went from 125˚C to the maximum temperature, with the first cycle starting at room temperature. The first test for each sample was performed to ensure mixing of the sample. The last two tests of each sample were used to ensure replicating results. The lowest cycling temperature of 125˚C was a limitation of the instrument.

For the systems of Na-Sn and Na-Nd the maximum heating temperature was 550˚C. This temperature was chosen to provide adequate safety margins from the melting temperature of the aluminum crucible, 660˚C during testing. The highest temperature for the system of Cs-Nd was 400˚C. The reduction for the Cs-Nd system was due to the failure of the hermetic seal at higher temperatures due to the cesium vapor pressure. This can be seen in Figure 19, where the hermetic seal failure seen by the significant weight loss in the sample at temperatures above 400˚C. The failure of the hermetic seal not only presented a safety hazard, due to the release of high temperature cesium gas, but also would result in changing mixture concentrations of the sample. Thus the Cs-Nd system was only investigated to 400˚C.

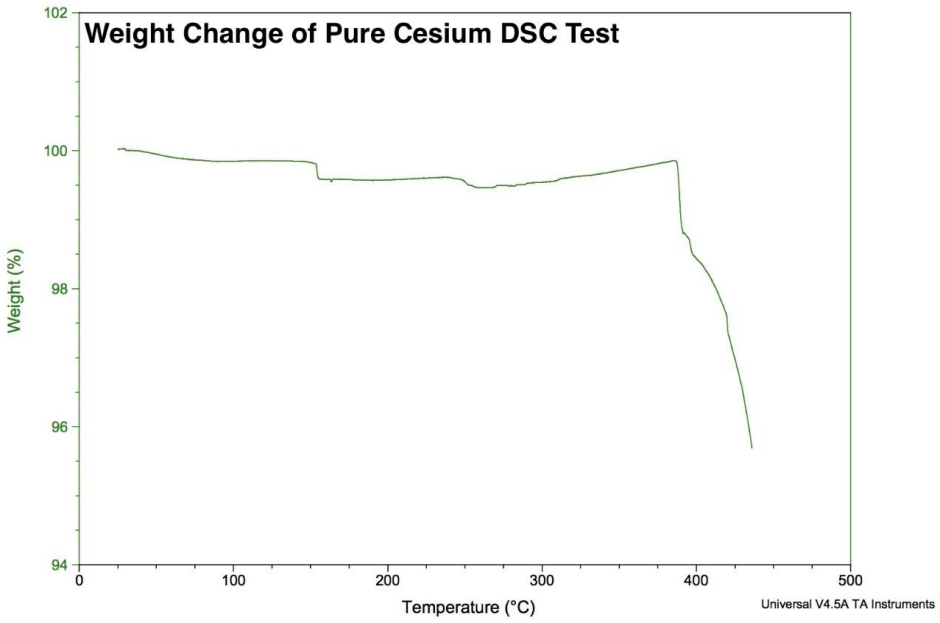


**Figure 19. Weight loss of high temperature DSC test of pure cesium.**

Upon the conclusion of each test, the weight changes and heat flow rate were recorded as a function of temperature. This was repeated for a range of concentrations to cover the mixing fractions of the phase diagram. The data collected by DSC was then used towards the phase diagrams of interest.

## 5.2 Na-Sn Results

To provide a comparison of the procedure used in this work, the phase diagram of Na-Sn was investigated. Shown in Figure 20 is the DSC heating curve of 95.8 at. % Na – 4.2 at. % Sn. Annotated on Figure 20, are the peaks of the curves of interest.

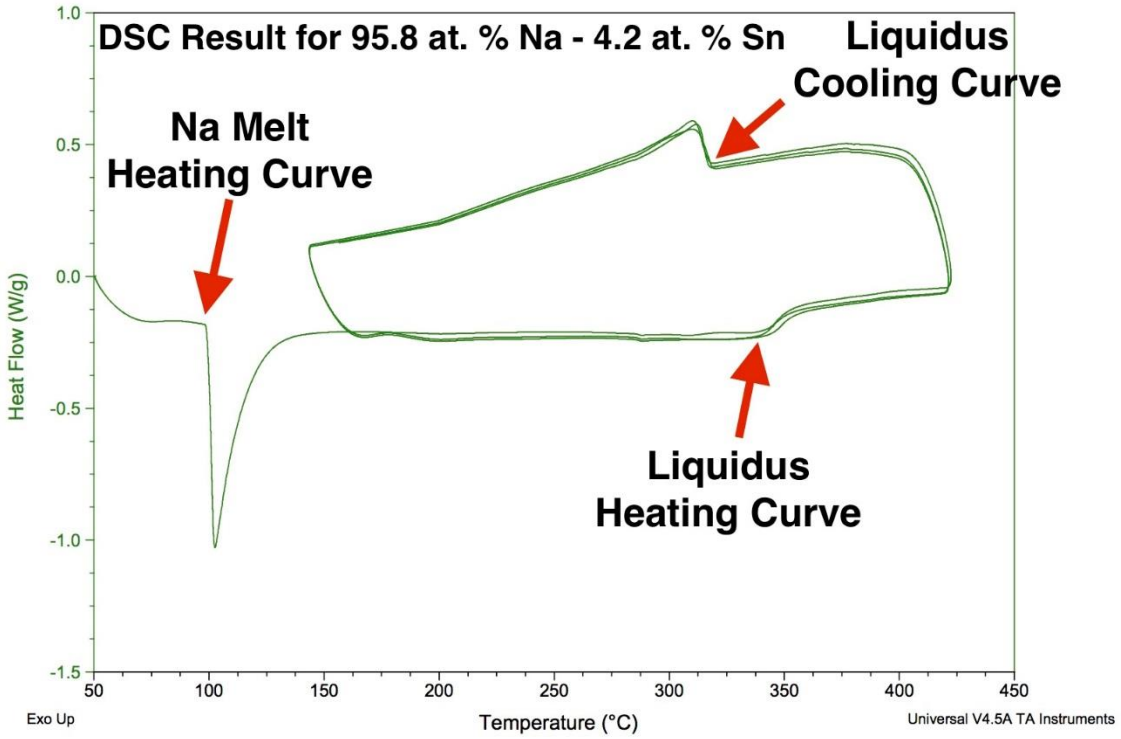


**Figure 20. DSC curves of 95.8 at. % Na – 4.2 at. % Sn.**

As can be seen the Na solid melting phase can be clearly seen in the first heating curve at 99.59˚C. The changes in the slopes of the heating and cooling curves in the temperature range of 300 to 350˚C represent the liquidus temperature on the phase diagram for this composition. All three cycles reproduce this feature quite clearly. From this result the temperature from the heating curve was 343.77 $\pm$ 0.52˚C while the cooling curve was 317.94 $\pm$ 0.35˚C. This deviation between the heating and cooling curve measurements from the equilibrium value can be explained by the kinetics involved in the experimentation compared to thermodynamic values [89].

To provide evidence of the procedure's ability in detailing more complex regions of the phase diagram the results of 71.3 at. % Na – 28.7 at. % Sn is shown in Figure 21. At this composition of the phase diagram there exists multiple phase transformations at relatively close temperatures. Figure 21 is one of the cooling curves with the transformation temperature results indicated. While some peaks are less distinct, the various phase transformations and their temperatures are evident in Figure 21.

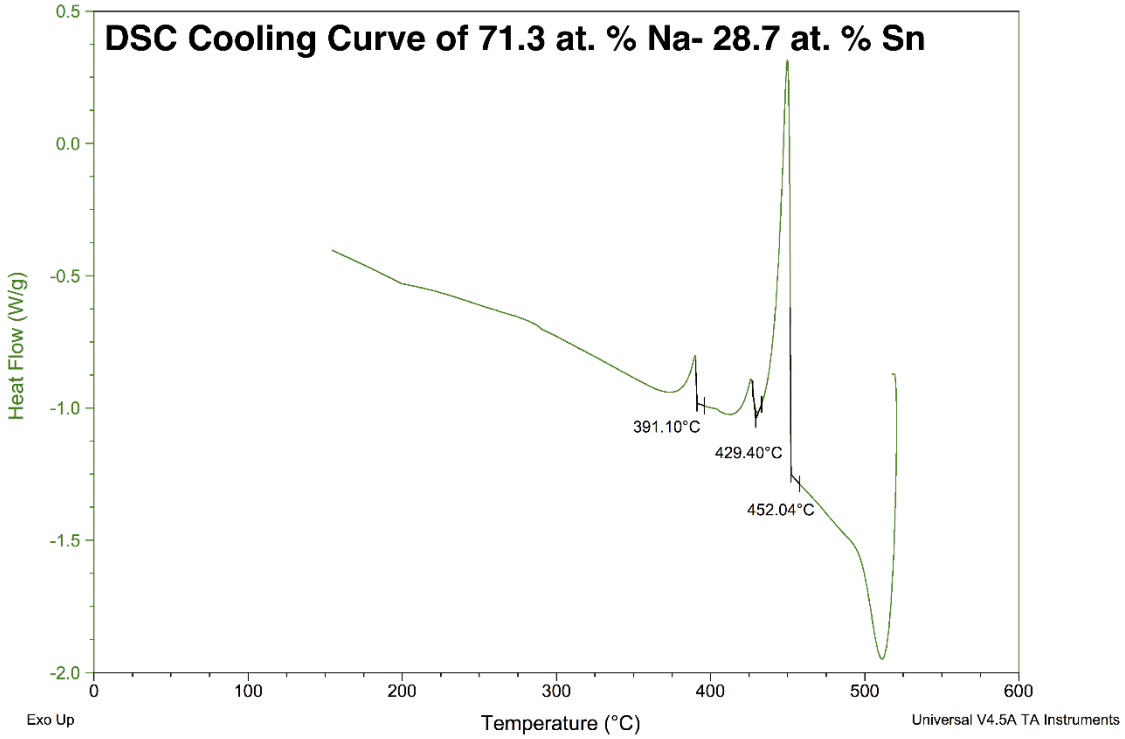


**Figure 21. Single DSC cooling curve for 71.3 at. % Na – 28.7 at. % Sn**

The most important portion of the phase diagram, for the purpose of this investigation, is the Na-rich side of the phase diagram. In Table 2 and Table 3 are the experimental measurements taken of the two major equilibrium lines on the Na-rich side of the assessed phase diagram [90]. Table 2 shows the liquidus line on the Na-rich side from the heating and cooling curves from this work and from the assessed phase diagram for those specific concentrations. The liquidus line is the solubility of tin in liquid sodium and thus is akin in the lanthanide-alkali metal phase diagrams to the solubility of the lanthanides in the liquid alkali metals. Table 3 shows this same comparison but for the temperatures of the equilibrium line of $Na\ solid + Na_{15}Sn_4 \leftrightarrow Liquid + Na_{15}Sn_4$.

**Table 2. Measurements of the liquidus line of the Na-rich side of Na-Sn.**

| Sn at. % | This Work | | Assessed Phase Diagram Temperature (˚C) [**40**] | Reference to Heating/Cooling Range (˚C) |
|---|---|---|---|---|
| | Heating (˚C) | Cooling (˚C) | | |
| 1.7 | 249.49 ± 0.95 | 241.52 ± 0.12 | 255 | 5.51 |
| 4.2 | 343.77 ± 0.52 | 317.94 ± 0.35 | 320 | Within |

| | | | | |
|---|---|---|---|---|
| 5.3 | 352.15 ± 0.76 | 334.85± 0.18 | 327 | -7.85 |
| 6.3 | 351.50 ± 0.62 | 336.09 ± 0.85 | 338 | Within |
| 8.8 | 364.34 ± 0.41 | 354.01 ± 1.16 | 355 | Within |
| 9.3 | 352.71 ± 1.13 | 340.77 ±1.18 | 358 | 5.29 |
| 12.4 | 382.30 ± 1.04 | 373.17 ± 1.04 | 380 | Within |
| 13.8 | 387.31 ± 0.30 | 377.04 ± 0.50 | 385 | Within |
| 28.7 | 478.26 ± 0.91 | 451.21 ± 0.69 | 475 | Within |
| 43.1 | 470.11 ± 0.79 | 461.36 ± 0.23 | 480 | 9.89 |

**Table 3. Measurements of $Na\ \ solid + Na_{15}Sn_4 \leftrightarrow Liquid + \ Na_{15}Sn_4$ transformation.**

| Sn at. % | This Work - Heating (˚C) | Phase Diagram Transformation Temperature (˚C) [**40**] | Difference (˚C) |
|---|---|---|---|
| 1.7 | 99.18 ± 0.73 | 98 | 1.18 |
| 4.2 | 99.59 ± 0.15 | | 1.59 |
| 5.3 | 98.92 ± 0.78 | | 0.92 |
| 6.3 | 98.80 ± 0.23 | | 0.80 |
| 8.8 | 99.09 ± 0.14 | | 1.09 |
| 9.3 | 99.56 ± 0.01 | | 1.56 |
| 12.4 | 99.48 ± 0.75 | | 1.48 |
| 13.8 | 99.27 ± 0.45 | | 1.27 |

For Table 2, a large portion of the data is within the temperature measurements by heating and cooling curves. Some of the largest differences are at the lower concentration where the liquidus line is the steepest. Thus a small change in the concentration in the sample is amplified by a large temperature difference. However, as a set of measurements, they produce the liquidus line quite accurately. For Table 3 only the initial heating cycle of each test could detect the equilibrium line as this temperature

was below the possible cycling temperature of the instrument. Both Table 2 and Table 3 show most deviations in the measurements are less than ± 1˚C. Some of the measurements do show deviations greater than ± 1˚C and this is most likely due to testing at the upper limit of acceptable heating rates at 10 ˚C/min and the large sample weights of greater than 10 mg. Both of these factors can create thermal gradients within the sample and cause error in the measurements. However, the main focus of this thesis for the Na-Nd and Cs-Nd phase diagrams is the alkali-rich liquidus line and detecting phase transformations in these systems. Hence while some measurements do show a lack of precision, it is not as crucial for this study as the transformations detection and accuracy, which this method has shown.

Shown in Figure 22 is the phase diagram of Na-Sn with the experimental data from this work. While the entire data set shows accurate results compared to the accepted values, the portion of the most importance for this work, the Na-rich liquidus line, shows very good accuracy to measure the solubility in Na-rich liquids.

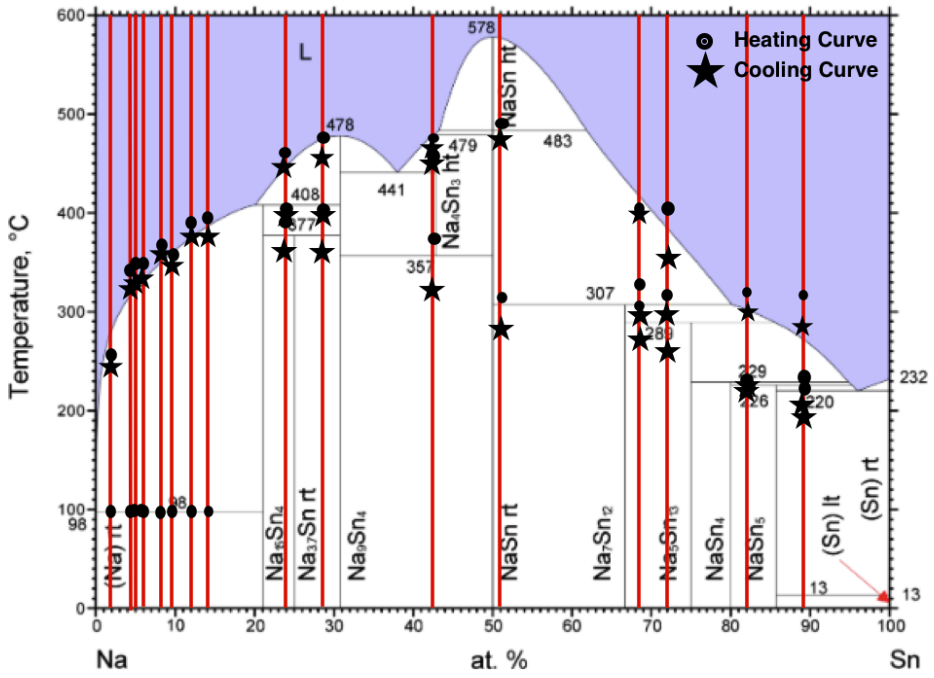


**Figure 22. Phase Diagram of Na-Sn with Experimental Data**

## 5.3 Na-Nd Reults

Shown in Figure 23 and Figure 24 are two of the results of the DSC curves for Na-Nd. Figure 23 represents the Na-rich side with a composition of 76.5 at. % Na – 23.5 at. % Nd. Figure 24 represents the Nd-rich side with a composition of 22.2 at. % Na - 77.8

at. % Nd.

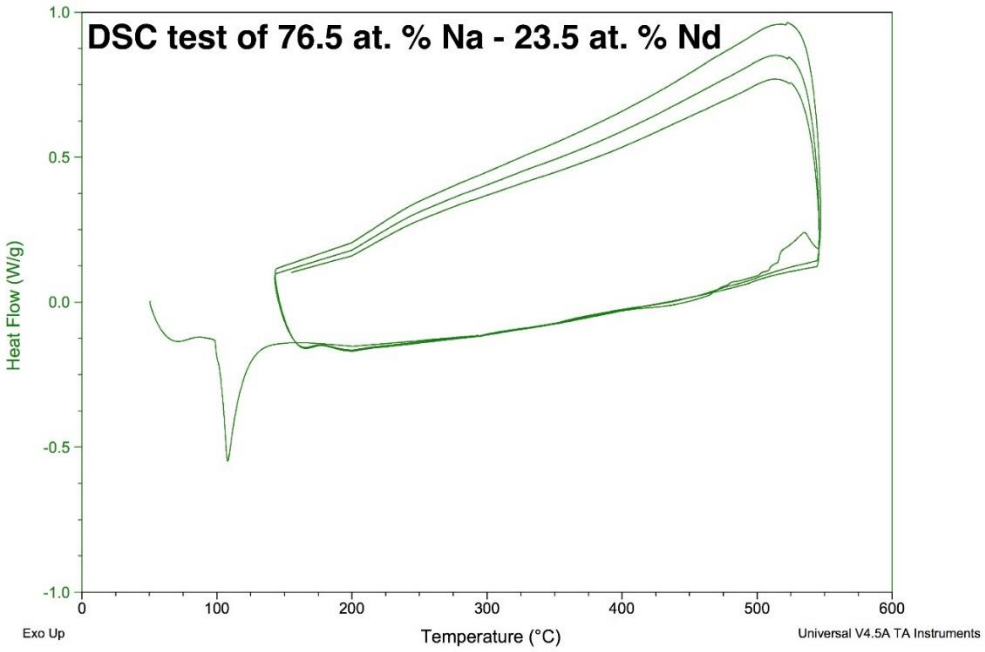


**Figure 23. DSC test of 76.5 at. % Na – 23.5 at. % Nd**

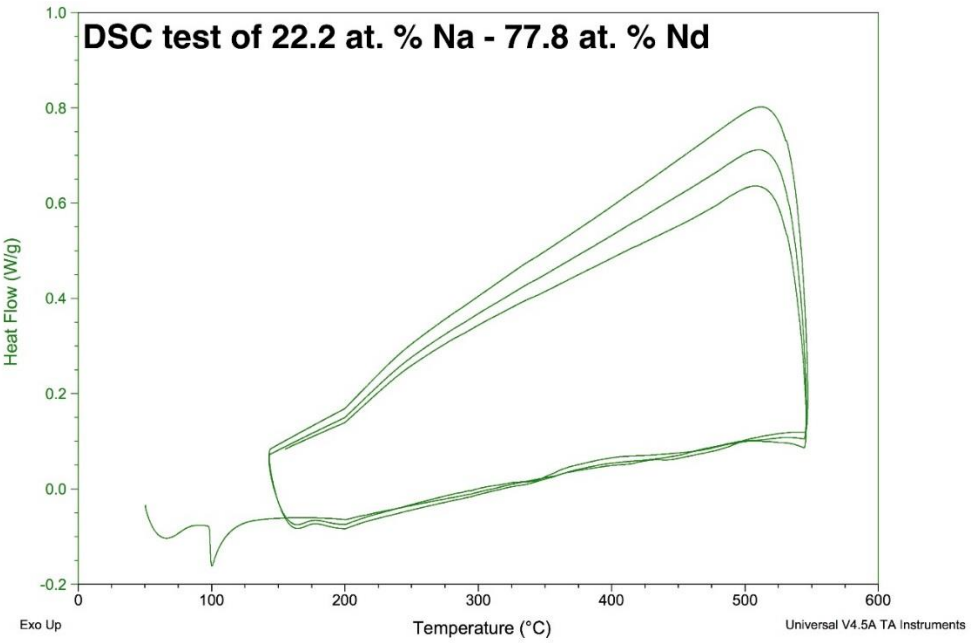


**Figure 24. DSC test of 22.2 at. % Na – 77.8 at. % Nd**

Both DSC curves in Figure 23 and Figure 24 show only one peak, at nearly the same temperature, over the temperature range investigated. This suggests over this temperature range only one phase transformation occurs, at 98.7˚C in Figure 23 and

97.7˚C in Figure 24. This single peak is very similar to the melting temperature of pure sodium at 98˚C and was measured in every test containing sodium, as shown in Table 4. The lack of additional peaks suggests no other phase transformations occur. This information helps lead to the conclusion of sodium and neodymium form immiscible solutions.

**Table 4. Transformation temperatures of the melting of sodium in each Na-Nd test containing sodium.**

| DSC Transformations for Na-Nd Samples | |
|---|---|
| Nd At. % | Temperature (˚C) |
| 94.9 | 99.63 ± 0.54 |
| 87.9 | 98.67 ± 0.35 |
| 77.8 | 98.60 ± 0.88 |
| 69.6 | 98.58 ± 0.14 |
| 53.4 | 98.87 ± 0.12 |
| 50.7 | 98.55 ± 0.20 |
| 39.0 | 98.19 ± 0.44 |
| 33.9 | 98.77 ± 0.47 |
| 23.5 | 99.41 ± 0.75 |
| 14.9 | 99.87 ± 0.18 |
| 9.7 | 99.32 ± 0.01 |
| 5.3 | 100.11 ± 0.11 |
| 2.8 | 100.68 ± 0.03 |
| 2.1 | 99.32 ± 0.09 |
| 2 | 99.18 ± 0.09 |
| 0.3 | 100.48 ± 0.11 |
| 0 | 100.23 ± 0.01 |

Additional emphasis was also placed on performing DSC tests on samples at the Na-rich side of the phase diagram. The emphasis was to investigate further the results from the solubility experiments. Based on the solubility results, the liquidus line over the temperature range tested should be at a concentration considerably smaller than achievable by this sample preparation method. Thus these DSC tests were performed to ensure consistent conclusions between the results. In Figure 25 is one of the smallest neodymium concentrations (99.7 at. % Na - 0.3 at. % Nd) to be practically prepared by this method.

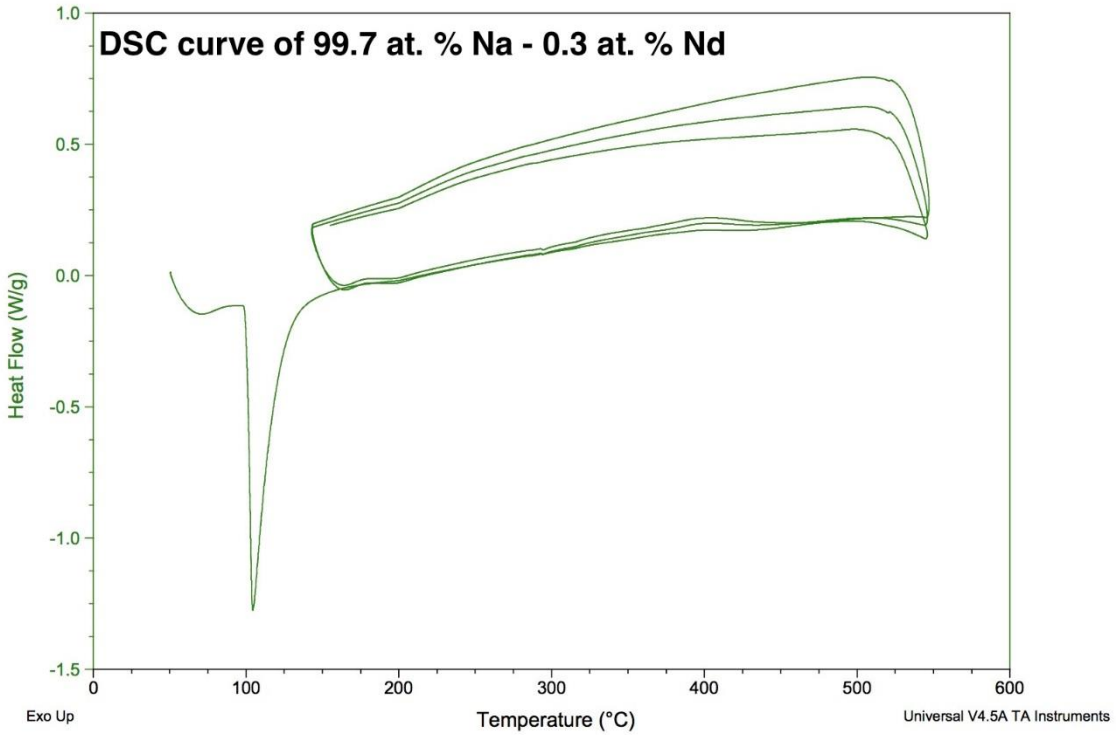


**Figure 25. DSC test of 99.7 at. % Na – 0.3 at. % Nd.**

In Figure 25 the only transformation that appears to occur at this concentration is the melting of the sodium solid phase. Any additional transformations, such as the transformation associated with liquidus line in Figure 20, is lacking at this composition. This results aids in determining the liquids line, and thus solubility, up to 550˚C occurs at a concentration below 0.3 at. % Nd.

## 5.4 Cs-Nd Results

Shown in Figure 26 is one of the results of the DSC curves for Cs-Nd. Figure 26 is the DSC curve for the sample of 29.6 at. % Cs – 70.4 at. % Nd. At the beginning of the test, at 29.59˚C a transition peak can be identified.

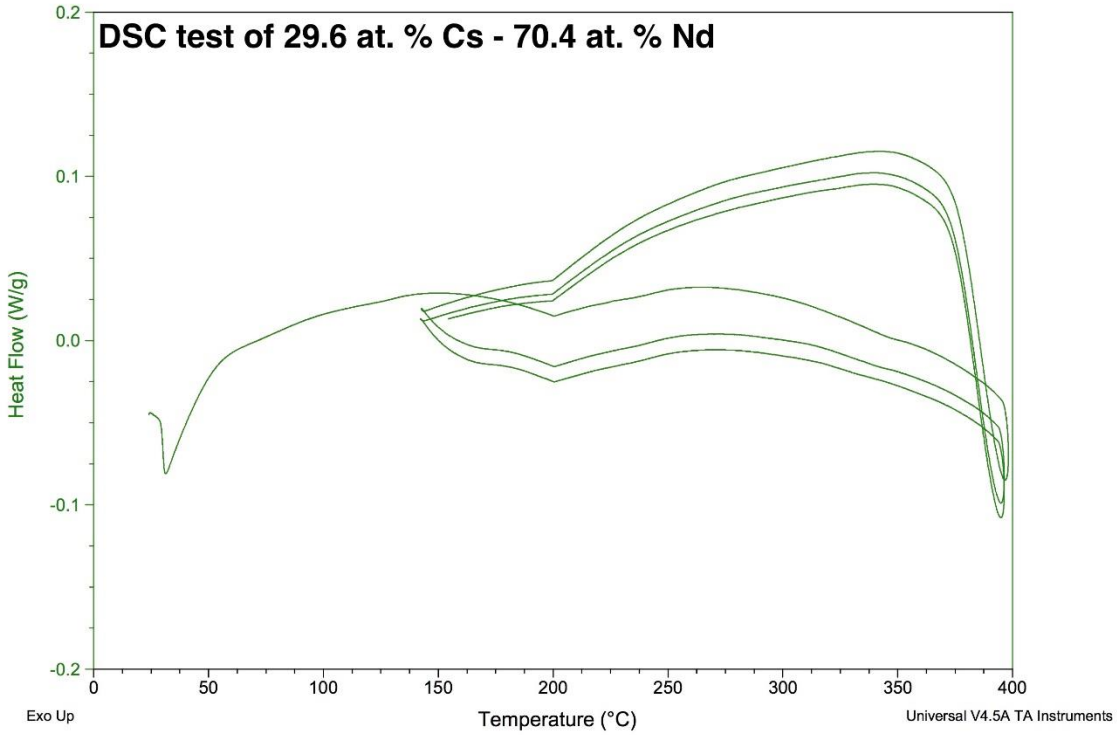


**Figure 26. DSC test of 29.6 at. % Cs – 70.4 at. % Nd**

A single transition peak at approximately 30˚C was identified in every tests containing cesium as shown in Table 5. This peak most likely corresponds to the cesium solid phase melting in the mixture, as the melting of pure cesium occurs at 28.5˚C. Based on the immiscible solutions for cesium and praseodymium reported previously by Griffin [**79**], and the DSC results, it was concluded the cesium and neodymium form immiscible solutions.

**Table 5. Transformation temperatures of the melting of cesium in each Cs-Nd test containing cesium.**

| DSC Transformations for Cs-Nd Samples | |
|---|---|
| Nd at. % | Temperature (˚C) |
| 95.2 | 29.03 ± 0.28 |
| 88.9 | 29.40 ± 0.32 |
| 85.4 | 30.24 ± 1.09 |
| 80.1 | 30.00 ± 0.77 |
| 76.5 | 28.45 ± 0.64 |
| 70.4 | 29.71 ± 0.12 |
| 66.5 | 32.54 ± 0.53 |
| 57.5 | 29.29 ± 0.16 |
| 51.2 | 28.57 ± 0.50 |

| | |
|---|---|
| 45 | 29.08 ± 0.28 |
| 40.7 | 28.64 ± 0.19 |
| 35.5 | 29.12 ± 0.38 |
| 24.6 | 28.80 ± 0.33 |
| 11.1 | 27.84 ± 0.20 |
| 1.3 | 29.64 ± 0.26 |
| 0 | 28.18 ± 0.53 |

A noticeable feature in Figure 26 is the change of slope that consistently occurs at slightly above 200˚C. This inflection point was noticed on every sample that contained cesium. While this feature was not present in the pure neodymium DSC curve, it was seen in the pure cesium metal tested in the aluminum hermetically sealed crucible, as shown in Figure 27.

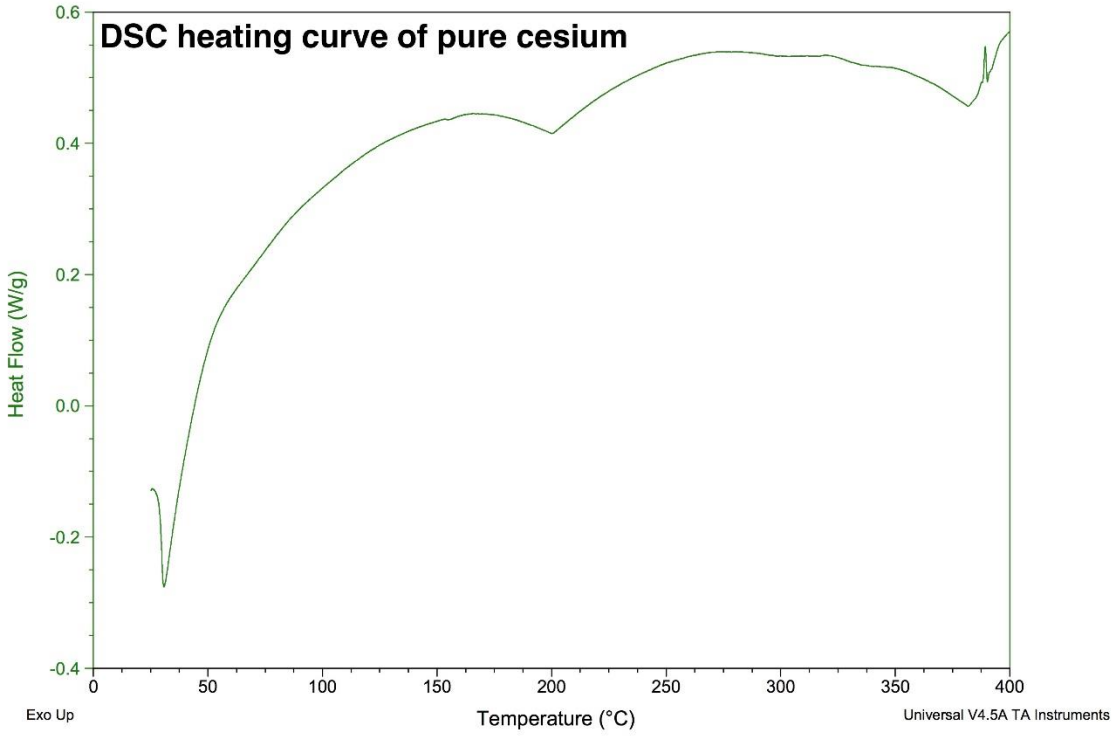


**Figure 27. DSC test of pure cesium in aluminum crucible**

Based on the phase diagram of aluminum-cesium no interaction should occur between the crucible and cesium [91]. Thus the curved response and abrupt slope change at 200˚C should not be due to the interaction between the crucible and the liquid cesium. It is likely this is simply the characteristic response behavior of the liquid cesium in the sealed crucible. This would explain why this feature is seen in every sample containing cesium. If cesium and neodymium are immiscible, as this thesis and other lanthanide-cesium diagrams indicate [79], then the response curves for the mixtures would be

composed of contributions of both pure cesium and pure neodymium alone, as no features from the interactions of cesium and neodymium would be present. Thus the DSC curves would retain certain aspects of the individual components of cesium and neodymium.

## 5.5 Phase Diagrams

Based on this work, the previously untested phase diagrams of the sodium-neodymium and cesium-neodymium are expected to resemble Figure 28 and Figure 29. Figure 28 and Figure 29 are the phase diagrams plotted using Thermo-Calc and include the experimental results from this work's DSC experiments and solubility experiments. Though at the composition resolution for phase diagrams the solubility results simply pin the liquidus line on the alkali metal rich side of the diagram to the edge, while the accuracy of the results from the DSC experiments can be seen.

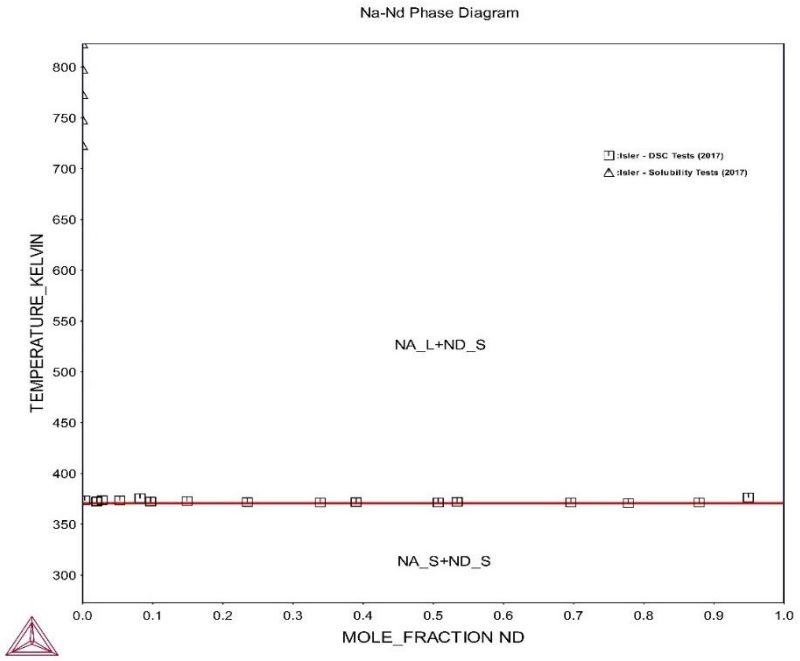


**Figure 28. Phase diagram of sodium-neodymium.**

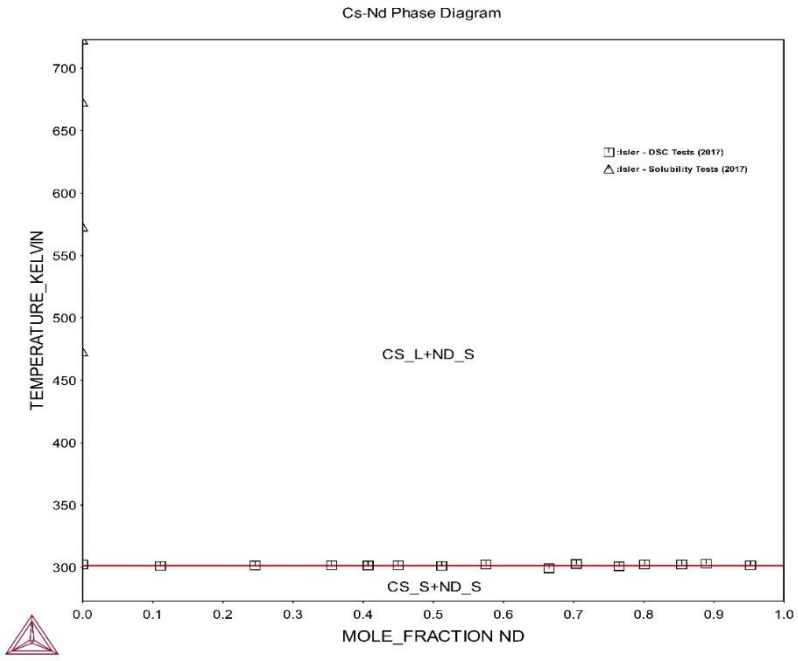


**Figure 29. Phase diagram of cesium-neodymium**

Both systems show no mutual solid solubilities, form no intermetallic phases, and have lanthanide solubility in the liquid alkali metal at less than 1 at. % at the greatest testing temperatures. Both phase diagrams are in good agreement with the partly speculative phase diagram of cesium-praseodymium [81].

# 6. Analytical Solution for Investigation of Soret Effects

## 6.1 Background

The Soret diffusion model may be used to describe a variety of transport phenomena when the temperature gradients play an important role. In the present study for FCCI phenomenon, this effect represents a major concern and a limiting factor in the operational lifetime of sodium cooled reactors. Hence, it is important to develop a fundamental understanding of the phenomena and time-scales involved in the transport process and further examine the effects of temperature gradients on the transport process. In this section, a model for the one-dimensional transport of a dilute species is considered for a situation with a steady state linear temperature profile which is instantly reached. General analytical solutions for the model are developed using the Green's function method and compared with numerical solutions for a specific situation. The analytical solutions may be useful for benchmarking purposes and comparison with experiment. Finally, it is found that a large Soret coefficient corresponds to fast mass transport and the role of the Soret effect is discussed.

This effect is typically characterized by a quantity known as the Soret coefficient $S_T = \frac{D_T}{D}$ which is defined as the ratio of the thermodiffusion coefficient ($D_T$) measured in $m^2/(s\ K)$ to the isothermal molecular diffusion coefficient (measured in $m^2/s$) and has units of (1/K). A positive value for this quantity drives transport towards the colder temperature region and vice versa. The observed values for the Soret coefficient depend on the system under study.

## 6.2 Mathematical Formulation of the Problems

For a binary mixture, the mass flux taking the Soret effect into account assumes the form [92]:

$$\boldsymbol{J} = -\rho D\ (\boldsymbol{\nabla} C + S_T C(1-C)\ \boldsymbol{\nabla} T) \qquad \text{Eq. 1}$$

In equation 1, the first term describes species flux due to the concentration gradient across the domain of interest and the second term captures the Soret effect which describes the contribution of the temperature gradient to the transport process. In equation 1, $C$ is the mass fraction of the solute species (component 1), $\rho$ is the mixture mass density, and D is the mass diffusion coefficient. When the solute (component 1) is dilute ($C \to 0$), then the nonlinear term in equation 1 may be ignored (since $(1 - C) \approx 1$) and the mass flux in the dilute limit reduces to:

$$J = \ -\rho D \ (\nabla C + S_T C \ \nabla T) \qquad \text{Eq. 2}$$

Hence, and by employing Fick's law the governing equation may be cast for one dilute species as:

$$\rho \frac{\partial C(x,t)}{\partial t} = \ \nabla . \left( \rho D(x,t) \left( \nabla C(x,t) + S_T C \ (x,t) \nabla T(x,t) \right) \right) + P(x,t) \qquad \text{Eq. 3}$$

This equation represents the governing equation for the problem at hand. The last term on the right hand side (*P(x,t)*) is a source term for the equation which physically represents generation of the species in the domain. In the case of nuclear metallic fuels for instance, this term would represent the fission process which is constantly yielding additional amounts of fission products.

When the temperature gradient and the transport process occur along the x-direction (in a domain with length *L*), and assuming that the density of the mixture is uniform then equation (3) may be recast in one dimension as:

$$\frac{\partial C(x,t)}{\partial t} = \frac{\partial}{\partial x} \left( D(x,t) \left( \frac{\partial C(x,t)}{\partial x} + S_T C(x,t) \frac{\partial T(x,t)}{\partial x} \right) \right) + Q(x,t) \ \ for \ \ 0 \le x \le L \qquad \text{Eq. 4}$$

In equation (4) we define $(Q(x,t) = P(x,t)/\rho)$(measured in (1/(m$^3$s)) . Moreover, when the temperature profile is linear, i.e. $T(x) = \ -ax + b$, and the diffusivity and Soret coefficient are assumed to be constant throughout the simulation. This assumption implies that thermal steady state is reached instantaneously, and the equation may be recast as:

$$\frac{\partial C(x,t)}{\partial t} = D \frac{\partial^2 C(x,t)}{\partial x^2} - aDS_T \frac{\partial C(x,t)}{\partial x} + Q(x,t) \quad for 0 \le x \le L \qquad \text{Eq. 5}$$

In this work we will present a generalized methodology for obtaining closed-form analytical solutions for the above equation with generalized boundary conditions and an initial condition of the form:

$$B_{11} \frac{\partial C(x,t)}{\partial x}\bigg|_{x=0} + B_{12} C(0,t) = \ f_1(t) \qquad \text{Eq. 6}$$

$$B_{21}\left.\frac{\partial C(x,t)}{\partial x}\right|_{x=L} + B_{22}C(L,t) = \ f_2(t) \qquad \text{Eq. 7}$$

$$C(x, t=0) = F(x) \qquad \text{Eq. 8}$$

where ($B_{ij}$) are real constant coefficients, f(x) is a function describing the initial distribution of the solute. In this case we will follow the Green's function approach [93] and first solve the homogeneous version of this problem.

## 6.3 Solution Methodology

In this case we introduce the substitution [94]:

$$C(x,t) = u(x,t)e^{\alpha x+\beta t} \qquad \text{Eq. 9}$$

By introducing this substitution to the problem we arrive at:

$$\frac{1}{D}\frac{\partial u(x,t)}{\partial t} = \frac{\partial^2 u(x,t)}{\partial x^2} + (2\alpha - m)\frac{\partial u(x,t)}{\partial x} + \left(\alpha^2 - m\alpha - \frac{\beta}{D}\right)u(x,t) + \frac{Q(x,t)}{D}e^{-\alpha x-\beta t} \qquad \text{Eq. 10}$$

where we introduced $m = aS_T$. We pick the two parameters α and β such that:

$$\alpha = \frac{m}{2} \qquad and \qquad \beta = -D\frac{m^2}{4} \qquad \text{Eq. 11}$$

With these values of the parameters, the governing equation reduces to:

$$\frac{1}{D}\frac{\partial u(x,t)}{\partial t} = \frac{\partial^2 u(x,t)}{\partial x^2} + \frac{Q(x,t)}{D}e^{-\alpha x-\beta t} \qquad \text{Eq. 12}$$

In addition, applying the substitution to the initial and the homogeneous boundary conditions yields:

$$B_{11}\left.\frac{\partial u(x,t)}{\partial x}\right|_{x=0} + (\alpha B_{11} + B_{12})\ u(0,t) = f_1(t)e^{-\beta t} \qquad \text{Eq. 13}$$

$$B_{21}\left.\frac{\partial u(x,t)}{\partial x}\right|_{x=L} + (\alpha B_{21} + B_{22})\ u(L,t) = f_2(t)e^{-\alpha L-\beta t} \qquad \text{Eq. 14}$$

$$u(x,t=0) = F(x)e^{-\alpha x} \qquad \text{Eq. 15}$$

In order to solve this problem, we will first solve the homogeneous version of the problem in order to find the appropriate Green's function for the problem. Once we arrive at the Green's function, then the solution of the general problem can be easily found. The homogeneous problem may be solved using the method of separation of variables and yields a Sturm-Liouville problem in space. Thus the solution to the homogeneous problem may be found analytically yielding the Green's function for the transformed problem as [93]:

$$G(x,t|y,s) = \sum_{n=1}^{\infty} \frac{1}{N(\lambda_n)} X_n(y)X_n(x)\ e^{\left(-\lambda_n^2 D+\beta\right)(t-s)} \qquad \text{Eq. 16}$$

where $X_n$ are the eigenfunctions corresponding to eigenvalue $\lambda_n$ and the normalizing factor is defined as:

$$N(\lambda_n) = \int_0^L X_n(x) * X_n(x)dx \qquad \text{Eq. 17}$$

Therefore, the final solution of the transformed problem may be written as:

$$\begin{aligned} u(x,t) = & \int_0^L G(x,t|y,0)F(y)e^{-\alpha y}dy \\ & + \int_0^t \int_0^L G(x,t|y,s)\frac{Q(y,s)}{D}e^{-\alpha y-\beta s}dyds \\ & + \int_0^t G(x,t|0,s)e^{-\beta s}f(s)\,ds \\ & + \int_0^t G(x,t|L,s)e^{-\alpha L-\beta s}f(s)\,ds \end{aligned} \qquad \text{Eq. 18}$$

Finally, the solution to the original problem is expressed as:

$$C(x,t) = \ u(x,t)e^{\alpha x+\beta t} \qquad \text{Eq. 19}$$

## 6.3 Application of the Solution

We now implement the derived analytical solution for a specific case and compare it with the numerical solution. We pick the case where $B_{11} = 0, B_{12} = 1,\ B_{21} = -D, B_{22} = -k, f_1(t) = f_2(t) = 0$ where (k) is a reaction rate (typically measured in m/s).

These boundary conditions corresponds to a physical situation where the species can diffuse out of the domain of interest at one end (at $x = L$). We further consider the case where the flux at this boundary is proportional to the concentration in that region. Physically, this may be reminiscent of heat convection (when the ambient temperature is zero), or the case where a reaction occurs at the x=L end of the domain with a reaction rate (k). This may include an adsorption type reaction, a chemical reaction or a redox reaction which leads to the depletion of the species of interest. This is exactly what occurs on the surface of the metallic fuel rod and may ultimately result in FCCI.

Non-Dimensionalization:

To facilitate the analysis, we choose to non-dimensionalize the system using the following quantities:

$$x^* = \frac{x}{L}\ ;\ t^* = \frac{tD}{L^2}\ ;\ T^*(x^*) = \frac{T(x)}{T_0}\ ;\quad S_T^* = S_T T_0\ ;$$
$$Q^*(x^*, t^*) = \frac{Q(x,t)L^2}{D}\quad ;\quad k^* = \frac{kL}{D}$$

Note that C is already in non-dimensional form as it is a mass fraction. Hence, the non-dimensional version of the problem assumes the form:

$$\frac{\partial C(x^*, t^*)}{\partial t^*} = \frac{\partial^2 C(x^*, t^*)}{\partial x^{*2}} + S_T{}^* \left(\frac{dT^*(x^*)}{dx^*}\right)\left(\frac{\partial C(x^*, t^*)}{\partial x^*}\right) + Q^*(x^*, t^*) \qquad \text{Eq. 20}$$

Along with the following initial and boundary conditions:

$$C(x^*, 0) = F^*(x^*) \qquad \text{Eq. 21}$$

$$C(0, t^*) = 0 \qquad \text{Eq. 22}$$

$$\left.\frac{\partial C(x^*, t^*)}{\partial x^*}\right|_{x^*=1} + k^*\ C(1, t^*) = 0 \qquad \text{Eq. 23}$$

Using the methodology outlined in the section above, we first assume:

$$C(x^*, t^*) = \ u(x^*, t^*)e^{\alpha x^* + \beta t^*} \qquad \text{Eq. 24}$$

From now on, all the stars on the variables will be dropped for ease of notation but all the shown work will be done in dimensionless quantities unless otherwise stated. By following the methodology outlined in the previous section we arrive at the solution:

$$u(x,t) = \int_0^L G(x,t|y,0)F(y)e^{-\alpha y}dy + \int_0^t \int_0^L G(x,t|y,s)Q(y,s)e^{-\alpha y - \beta s}dyds \qquad \text{Eq. 25}$$

where, $\alpha = \frac{a\ S_T^*}{2T_0}$ and $\beta = -D\alpha^2$ the Green's function is given by:

$$G(x,t|y,s) = \sum_{n=1}^{\infty} \frac{1}{N(\lambda_n)} e^{\alpha(x-y)} X_n(y) X_n(x)\ \ e^{(-\lambda_n^2 + \beta)(t-s)} \qquad \text{Eq. 26}$$

For this particular case, we have:

$$X_n(x) = sin(\lambda_n x) \qquad \text{Eq. 27}$$

And the eigenvalues for the problem are the roots of the transcendental equation:

$$(\alpha + k)tan(\lambda_n) + \lambda_n = 0 \qquad \text{Eq. 28}$$

And the normalization factor is given by:

$$N(\lambda_n) = \left[\frac{1}{2} - \frac{sin(2\lambda_n)}{4\lambda_n}\right] \qquad \text{Eq. 29}$$

Results and Discussion:

The solution in the section above was run for the following non-dimensional parameters:

$$k^* = 2, S_T^* = 2 \ , \qquad a^* = \frac{aL}{T_0} = \frac{1}{3}$$

The slope parameter ($a^*$) may correspond to a temperature difference of 100 K between the two boundaries and using room temperature (300 K) as reference temperature. In addition, we choose:

$$F^*(x^*) = {F_0}^*\left(x^* - {x^*}^2\right)$$

$$Q^*(x^*, t^*) = {Q_0}^* \ sin(x^*) \ e^{-\gamma t^*}$$

In order to illustrate the analytical solution for a specific case and compare it with the numerical solution, we choose the values ${F_0}^* = 1$ and ${Q_0}^* = 10$ and $\gamma = 0.1$ for the non-dimensional constants. In addition, the integrals were performed numerically using the global adaptive quadrature method as implemented in MATLAB. The infinite series of the analytical solution was truncated after including the first 200 terms. The results are shown below for five different non-dimensional times in the simulation.

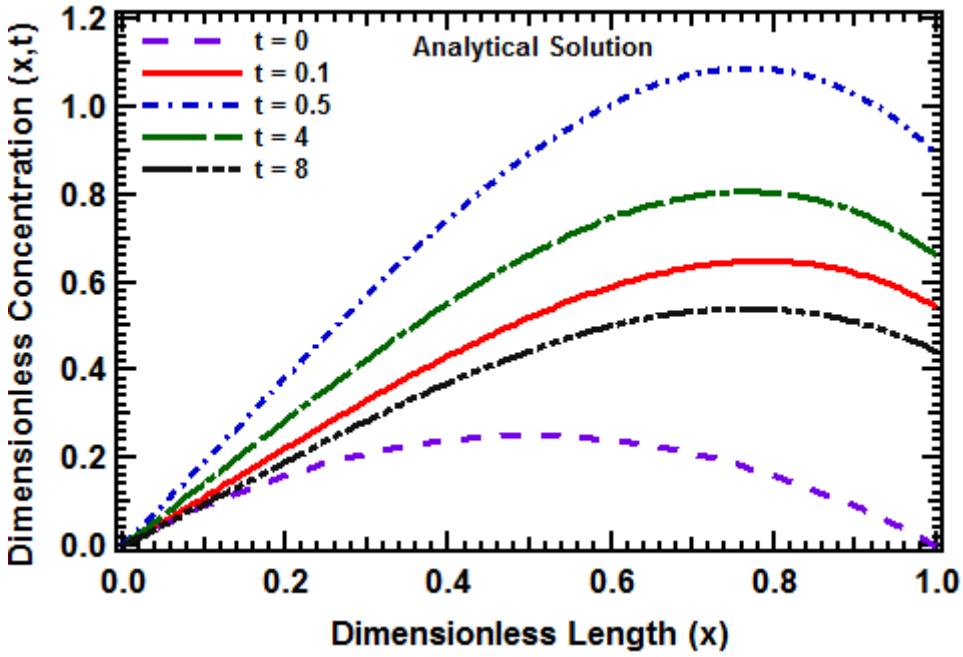


**Figure 30. The analytical solution of the problem shown for five different times in dimensionless units**

From Figure 30, we observe that the distribution first increases (for t=0.1 and t=0.5) as a result of the source term which decays with time. For time steps (t=4 and t=8) we observe the distribution decaying as a result of the flux at the x=1 boundary.

Next, and to verify the analytical solution, the problem was solved numerically. This was accomplished using the explicit forward Euler method. Moreover, ghost points

were used at the boundary ($x = 1$) in order to achieve a higher degree of accuracy in calculating the derivative. The system was simulated for the same parameters as above. A mesh size of 0.0067 and a time step of $2\times10^{-5}$ were used. The results are plotted in Figure 31 below.

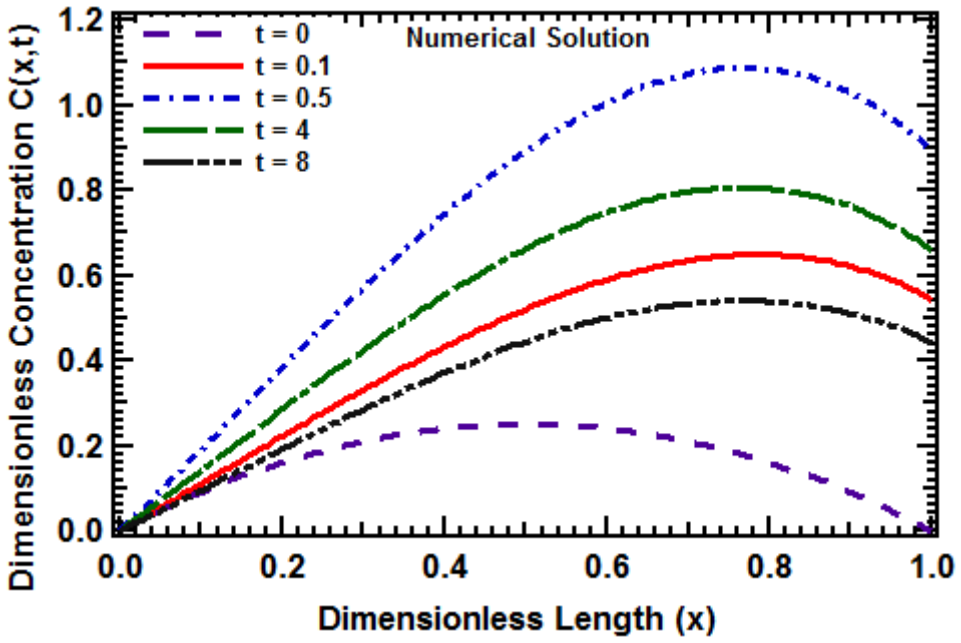


**Figure 31. The numerical solution of the problem shown for five different times in dimensionless units**

Finally, and to better compare the numerical and analytical solutions, the error was defined as:

$$Error(x,t) = C_{Numerical}(x,t) - C_{Analytical}(x,t) \qquad \text{Eq. 30}$$

This difference is plotted below in Figure 32.

From this analysis, we observe that the analytical solution agrees very well with the numerical solution with the relative error not exceeding 0.01% (except at the x=1 boundary for the initial distribution). The higher discrepancy for the initial distribution at the x=1 boundary may be explained by the fact that the chosen initial distribution doesn't satisfy that boundary condition.

The slight discrepancy between the numerical and analytical solutions may be explained by the errors produced through the numerical approximation of derivatives in the numerical solution and also by the errors due to the truncation of the infinite series in the analytical solution.

**(a)**

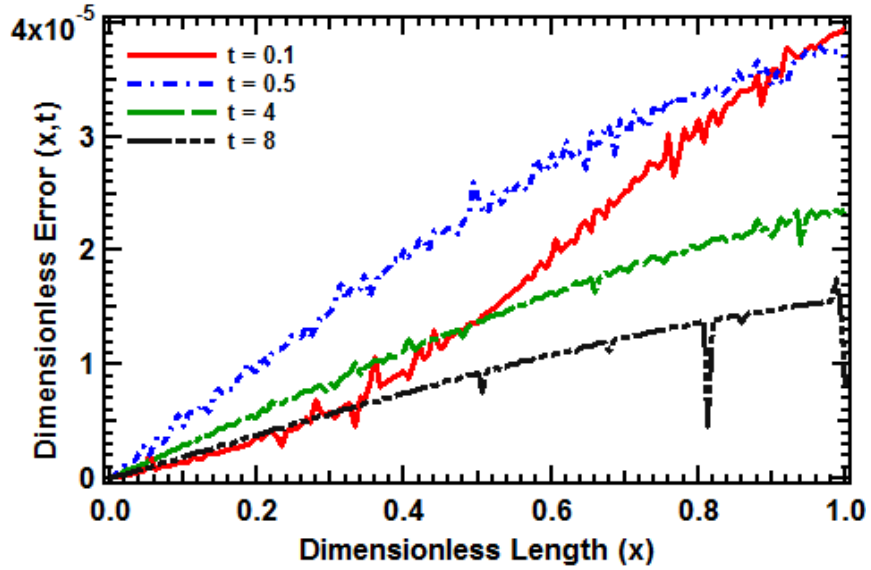


**(b)**

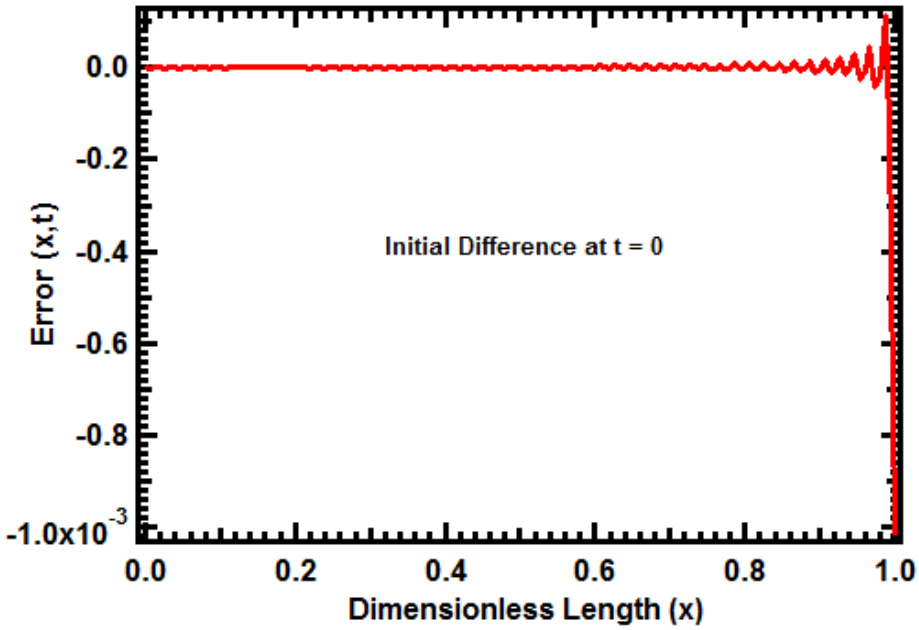


**Figure 32. The difference between the numerical and analytical solutions of the problem shown for five different times in dimensionless units. The initial difference at t=0 was plotted separately in (b).**

Next, we analyze the behavior of the solution with respect to the Soret term in order to better understand the role it possesses in governing the transport phenomenon. This was accomplished by running the simulation for different values of the non-dimensional Soret coefficient. This included the value of ($S_T = 0$) to gain some insight into the transport phenomenon in the absence of the Soret term. The results are shown in Figure 33 below.

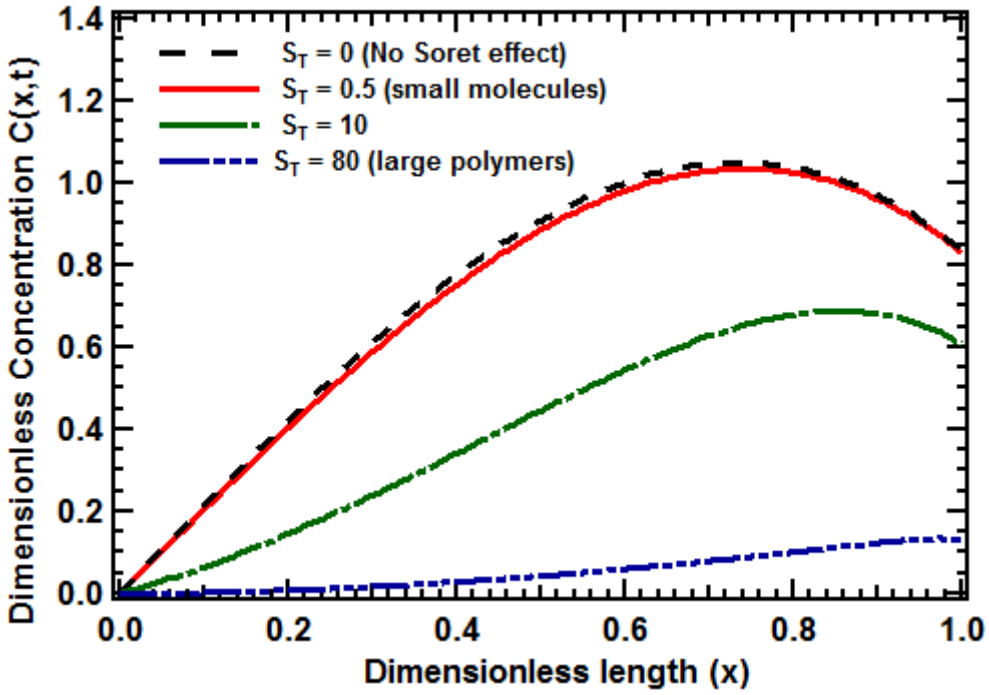


**Figure 33. The results of the analytical solution shown at non-dimensional time t = 2 for multiple values of the Soret coefficient.**

From examining Figure 33, it is clear that the Soret term plays an important role in the transport phenomenon. The transport of the species across the length of the domain may be significantly accelerated through the temperature gradient. In many science and engineering applications, the Soret effect is not considered, however, this may not be accurate as evidenced by the important role the Soret term may play. The Soret effect plays a different role for small molecules and fission products (with $S_T$ on the order of $10^{-3}$ $K^{-1}$) than it does in large colloids and large spent fuel elements (with a Soret coefficient on the order of 1 $K^{-1}$) as evidenced by the figure. Therefore, the Soret term may play an important role in transport phenomena and it should be treated with care and ignored after careful consideration. The strength and extent of this effect will depend on the materials being considered and the environment. Finally, it should be mentioned that a larger number of terms in the infinite summation of the analytical solution were needed for larger values of the Soret coefficient.

In closing, it must be emphasized that the current study considered the diffusivity and the Soret coefficient to be constants. However, this is not entirely accurate as these terms are known to display concentration and temperature dependences. Nevertheless, in some cases it may be an acceptable assumption to ignore those dependences if the values of these transport coefficients don't change too drastically in the concentration and temperature values of interest. In such cases, the derived analytical solutions may be useful to enable a simple interpretation of experimental data and may also be used

for benchmarking purposes.

General analytical solutions for the planar Soret diffusion of a dilute species in a linear temperature profile were developed. This entailed using a substitution, along with the method of Green's functions and Sturm-Liouville theory. The solution methodology was verified against a benchmark solution to the dilute Soret cell problem. The derived analytical solutions were also implemented for a specific case and displayed good agreement with the numerical solutions. Furthermore, it was found that the Soret term could significantly enhance the diffusion of the species.

# 7. Fundamental Data Calculations

## 7.1 Miedema Idea Model for Solubility Calculation

### 7.1.1 Thermodynamic Fundamental

The solubility of a metal A in a liquid metal B can be described by the equilibrium partial reaction:

$$A_{metal} \leftrightharpoons A_{in\ liquid\ metal\ B} \quad \text{Eq. 31}$$

For a real solution with a dilute quantity of A in the liquid metal B, the partial molar Gibbs free energy of A in the liquid metal B can be defined as the sum of the ideal solution partial molar Gibbs free energy and the deviation from the ideal solution, known as the excess partial molar Gibbs free energy:

$$\Delta\bar{G}_A = \Delta\bar{G}_A^{ideal} + \Delta\bar{G}_A^{Ex} \quad \text{Eq. 32}$$

Both the ideal partial molar Gibbs free energy of A in the liquid metal B and the excess partial molar Gibbs free energy of A in the liquid metal B can be expanded to include their respective enthalpy and entropy terms as shown:

$$\Delta\bar{G}_A^{ideal} = \Delta\bar{H}_A^{ideal} - T\Delta\bar{S}_A^{ideal} \quad \text{Eq. 33}$$

$$\Delta\bar{G}_A^{Ex} = \Delta\bar{H}_A^{Ex} - T\Delta\bar{S}_A{}^{Ex} \quad \text{Eq. 34}$$

For the ideal solution, the partial molar Gibbs free energy of A in the liquid metal B can be related to the mole fraction of component A, $x_A$, then:

$$\Delta\bar{G}_A^{ideal} = RTln(x_A) \quad \text{Eq. 35}$$

In an ideal solution the partial molar enthalpy of A in the solution, $\Delta\bar{H}_A^{ideal}$, is zero. Therefore, the ideal partial molar entropy of A in the solution, $\Delta\bar{S}_A^{ideal}$, can be expressed as:.

$$\Delta\bar{S}_A^{ideal} = -Rln(x_A) \quad \text{Eq. 36}$$

Then the partial molar Gibbs free energy of A in solution can be written as:

$$\Delta\bar{G}_A = \Delta\bar{H}_A^{Ex} - T\Delta\bar{S}_A^{Ex} + RTln(x_A) \quad \text{Eq. 37}$$

When the concentration of A in the liquid metal B is the solubility concentration then the dissolution reaction is in equilibrium and the partial molar Gibbs free energy of the A in the solution is zero. At equilibrium:

$$\Delta\bar{H}_A^{Ex} - T\Delta\bar{S}_A^{Ex} + RTln(x_A) = 0 \qquad \text{Eq. 38}$$

Thus the temperature dependence of the solubility of A in liquid metal B can be expressed:

$$ln(x_A) = \frac{\Delta\bar{S}_A^{Ex}}{R} - \frac{\Delta\bar{H}_A^{Ex}}{RT} \qquad \text{Eq. 39}$$

### 7.1.2 Miedema Model Description

The macroscopic atom model, known commonly as the Miedema model [95], is a semi-empirical model developed to determine the enthalpy associated with metal alloys. This model allows for a prediction of the enthalpy associated with the interaction of two elements, with a focus on transition metals, in both solid solutions and liquid solutions. The values of the model's parameters are empirical but have been shown to be representative of the physics and chemistry related to the enthalpy effects [95].

During the development of the Miedema model, it was suggested the model could be applied to predicting transition metals', used in crucible materials, solubility in liquid sodium. The use of this model for solubility in liquid alkali metal coolants has been shown in previous research for liquid lithium [96]. To better understand this model's predictive capabilities for the solubility of lanthanides in liquid sodium and liquid cesium, this thesis compared previously published experimental data of metals in liquid alkali metals to the results of this model. The comparison provides information on the accuracy of the model's prediction and then the model can provide a basic understanding of the feasibility of solubility experiment results for previously untested systems.

Referring back to Eq.39, the solubility of a metal alloy can be represented by the excess partial molar enthalpy and entropy of the solute metal in the solution. The Miedema model allows for a prediction of the excess partial molar enthalpy based on this semi-empirical approach.

The excess partial molar enthalpy of a metal in a liquid solution of another metal calculated from the model is based on the enthalpy effects from the interaction at the interface between the two elements. This interaction is modeled using several

parameters which are based on physical properties but whose values have been optimized using experimental data. One of the physical properties is the effect of solute metal's surface area in the interaction and is included by the molar volume $V_A$. The work function $\varphi$, which is similar to the electronegativity, is to account for the potential felt by the outer electrons between the two elements. The effect of the electron density at the interface is included by the parameter $n_{ws}$, which is related to the Wigner-Seitz cell. Using these parameters, the excess partial molar enthalpy of two metals is calculated using:

$$\Delta\bar{H}_A^{Ex} = \frac{2\ x\ V_A^{2/3}\ x\ P}{\left(n_{ws\ A}^{-1/3}\right) + \left(n_{ws\ B}^{-1/3}\right)} x\left(-(\Delta\varphi)^2 + \frac{Q}{P}\left(\Delta n_{ws}^{\frac{1}{3}}\right)^2\right) \qquad \text{Eq. 40}$$

where Q/P is a constant of 9.4 while P is a proportionality constant which depends on the valences of the two metals in the system. The allows the calculation of the excess partial molar enthalpy of a dilute quantity of metal A in the liquid metal B. For interactions between transition and non-transition metals an additional parameter, $R^*$, is necessary. While the physical representation of this term is debated, its addition has been attributed to an atomic nearest neighbor effect and has been shown necessary by experiments [95]. Thus the following equation is the excess partial molar enthalpy for the solution of a transition metal and a non-transition metal.

$$\Delta\bar{H}_A^{Ex} = \frac{2\ x\ V_A^{2/3}\ x\ P}{\left(n_{ws\ A}^{-1/3}\right) + \left(n_{ws\ B}^{-1/3}\right)} x\left(-(\Delta\varphi)^2 + \frac{Q}{P}\left(\Delta n_{ws}^{\frac{1}{3}}\right)^2 + R^*\right) \qquad \text{Eq. 41}$$

The parameters for the majority of the elements of the periodic table have been previously tabulated [95]. By using the tabulated parameters, the Miedema model can be used to predict the excess partial molar enthalpy of entire groups of elements in their interactions with other metals, as this work does.

By using the Miedema model, a prediction of the solubility of the lanthanides in liquid sodium and liquid cesium was determined. The Miedema model was used to predict the excess partial molar enthalpy for the solubility. The excess partial molar entropy term was modeled using two various techniques.

The first technique was in neglecting the excess partial molar entropy term and using Equation 42 to calculate the solubility. Previous works have suggested this is acceptable for systems where the excess partial enthalpy is large and positive [95]. These works argue in these systems the entropy is mainly due to vibrational effects and thus would

be on the order of magnitude of the gas constant. In these systems the entropy contribution to the solubility is dwarfed by the by the large positive excess partial molar enthalpy term. By neglecting the entropy contribution, the solubility is defined as:

$$X_A(T) = \exp\left(\frac{-\Delta\bar{H}_A^{Ex}}{RT}\right) \quad \text{Eq. 42}$$

The second technique is by correlating the excess partial molar enthalpy to the excess partial molar entropy term by a constant correlation parameter, $\tau$. Derived from the quasi-regular solution, it has been previously suggested to be between 1500 and 3000 K for metallic solutions [97]. The relationship between the enthalpy and the entropy is:

$$\Delta\bar{H}_A^{Ex} = \tau\Delta\bar{S}_A^{Ex} \quad \text{Eq. 43}$$

The use of a correlation parameter of 3000 K has been shown applicable for most solutions and has previously shown success in the prediction of the solubility of transition metals in liquid lithium [96]. In using the correlation parameter, the solubility can be defined as:

$$X_A(T) = \exp\left(\frac{\Delta\bar{H}_A^{Ex}}{\tau R}\right)\exp\left(\frac{-\Delta\bar{H}_A^{Ex}}{RT}\right) \quad \text{Eq. 44}$$

This work compares the solubility predicted by the Miedema model and the various entropy calculations to previous experimental data. By analyzing the relationship of the predicted and experimental solubility across the liquid alkalis, trends can be stated to discuss the accuracy of the predictions and the appropriate excess entropy contribution to use. From these trends, the predicted solubility can be used more accurately used to predict the lanthanides in liquid sodium and liquid cesium.

### 7.1.3 Model Comparison to Previous Solubility Experiments

To investigate the model's effectiveness, experimental data from previous solubility experiments were compared to the model's prediction. As iron is one of the elements with the most experimental solubility data in liquid alkali metals, performing the comparison for iron provides the some of the most detailed information. The comparison with iron provides a good representation for the majority of the experimental data for metals in liquid alkalis. For additional comparisons to further validate the general trends between the model's solubility prediction and experimental data from the iron systems, one is referred to the work of Isler and Zhang [98].

Shown in Figure 34 through Figure 38 are the comparisons of iron to the liquid alkali metals. In each figure are three predictions from the model: the solubility if the entropy term is neglected, the solubility if the excess partial molar entropy is modeled with an correlation parameter, $\tau$, of 3000 K, and the solubility if the entropy is modeled with a correlation parameter of 1500 K. These three predictions provide ranges for the predicted solubility as a function of temperature. While the range between these estimates may seem very large, the amount of scatter in experimental solubility data justifies the inclusion of this large of a range.

The solubility of iron in liquid lithium is shown in Figure 34. The previous experimental data shows considerable scatter between experiments. This amount of scatter is common for the various metals in liquid alkali metal systems when comparing the multiple experiments. The biggest reason for this is due to the affect impurities such as oxygen, carbon, and nitrogen have on the solubility measurements. By comparing multiple experiments, multiple impurity concentrations are compared and thus explain part of the scatter. In analyzing the described model to experiments, which did not purposefully add these impurities, a representation of the scatter of future solubility test can be showcased.

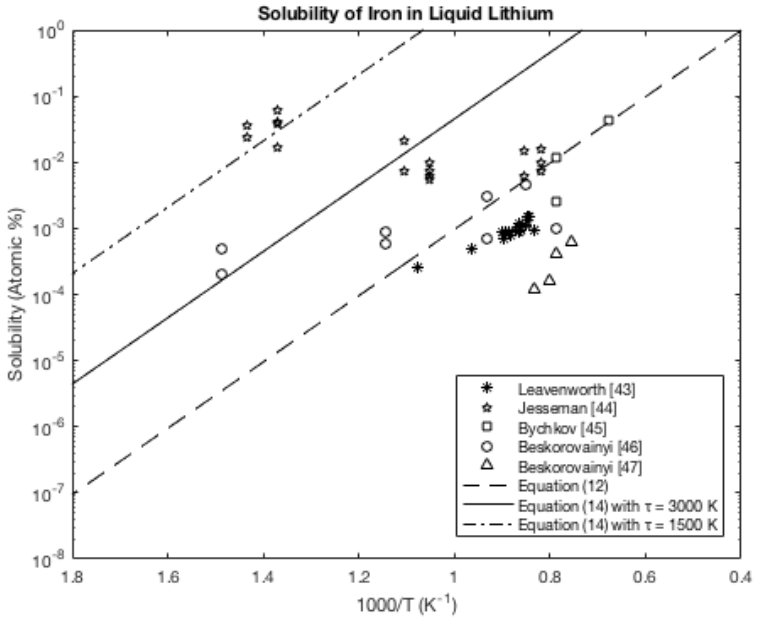


**Figure 34. Solubility of iron in liquid lithium comparison for the Miedema model and previous experimental data.**

In Figure 34, the largest amount of iron in liquid lithium data where the entropy term has less of an effect on the predicted solubility. When considering all of the experiments, the temperature dependency of the data is lost due to the scatter. In order to properly

compare the temperature dependence of the model to the data, the temperature dependence of individual experiments must be analyzed. The majority of the experimental data, especially near the prediction with neglected entropy, show temperature dependencies, which are only slightly less than predicted by the model.

The solubility of iron in liquid sodium, potassium and rubidium are shown in Figure 35, Figure 36, and Figure 37 respectively. While the amount of liquid rubidium data is scarce, it shows many of the same trends across the metal solubilities as both sodium and potassium. The majority of their experimental data is within the range predicted when a correlation parameter is incorporated, with a tendency towards being closer to the prediction with an interaction parameter of 3000 K. In addition, the temperature dependencies all of the experiments are considerably less than the models but the majority of individual experiments due show an increase of solubility with increasing temperature.

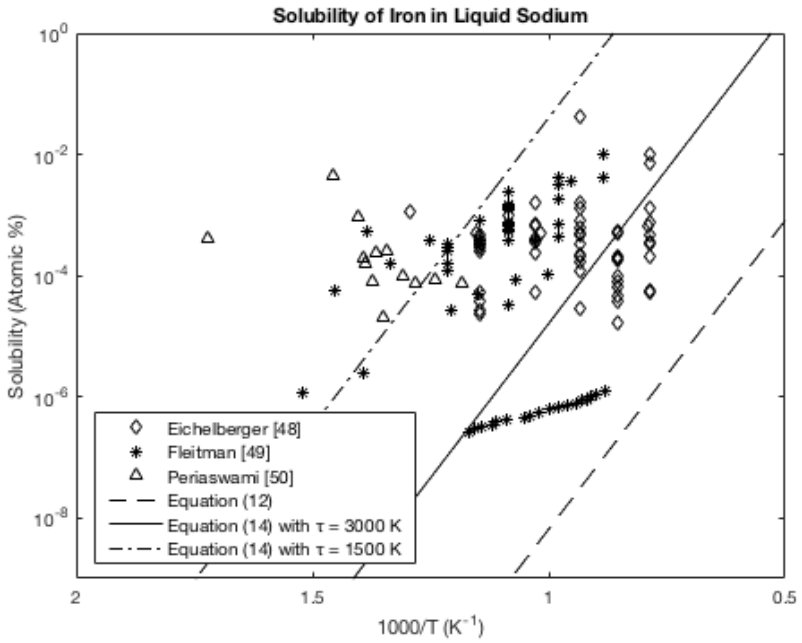


**Figure 35. Solubility of iron in liquid sodium comparison of the Miedema model and previous experimental data.**

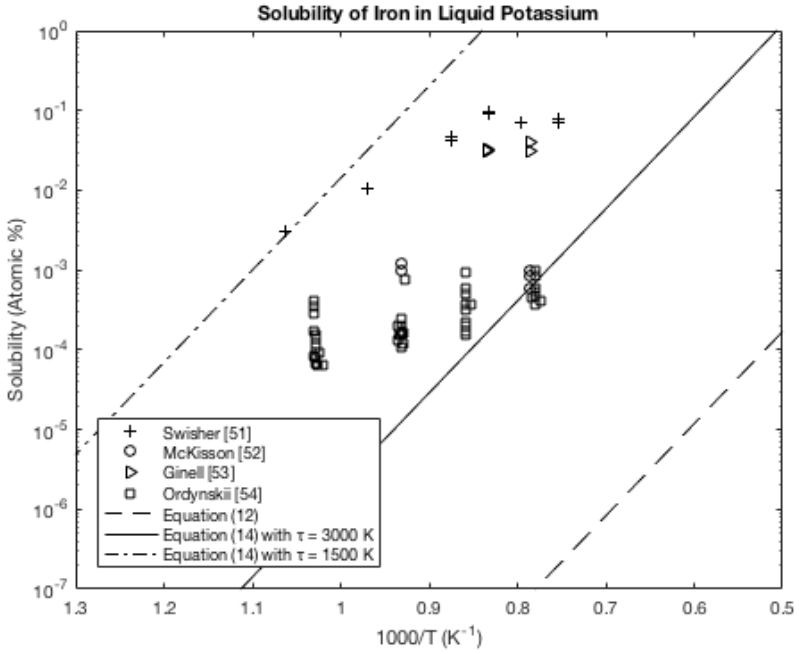


**Figure 36. Solubility of iron in liquid potassium comparison of the Miedema model and previous experimental data.**

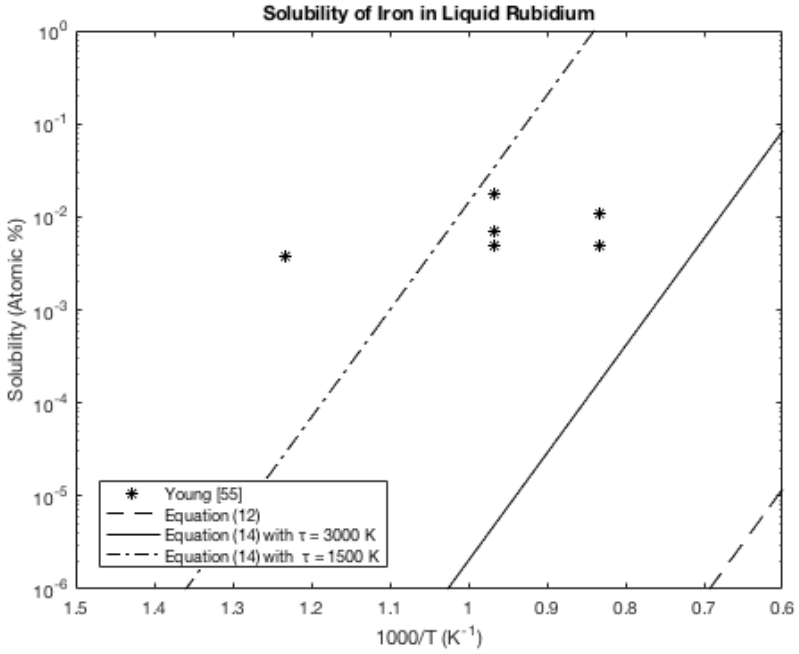


**Figure 37. Solubility of iron in liquid rubidium comparison of the Miedema model and previous experimental data.**

The iron solubility in liquid cesium is shown in Figure 38. As in the case for liquid rubidium, the experimental data for liquid cesium is extremely limited but several features appear for the majority of the data in liquid cesium. The experimental data in

liquid cesium show a temperature dependency considerably smaller than the prediction. All of the experimental solubilities are considerably larger than predicted by even with a correlation parameter of 1500 K. The predictions over the range of temperatures for the majority of experimental data for liquid cesium, is lower than any current experimental method for liquid alkali metals can detect.

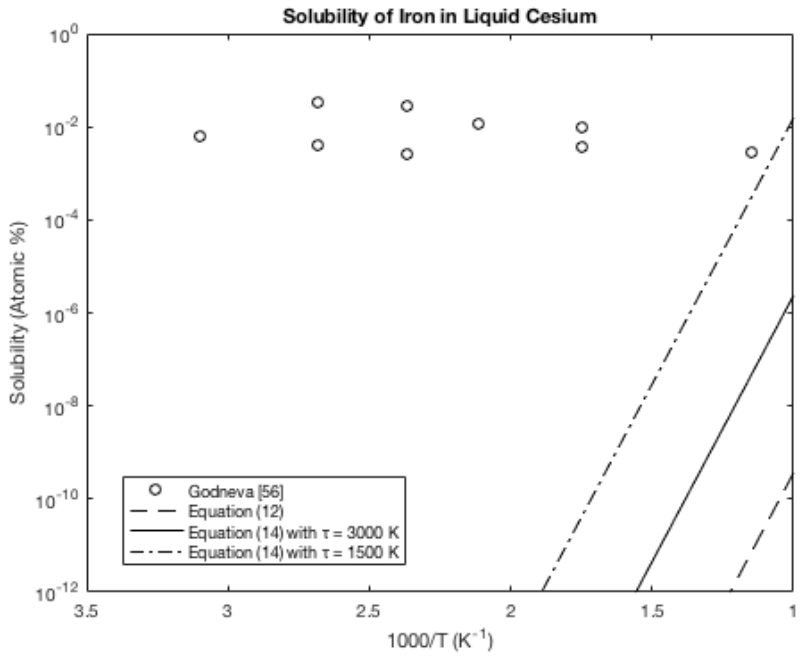


**Figure 38. Solubility of iron in liquid cesium comparison of the Miedema model and previous experimental data.**

When analyzing all the alkalis, several trends manifest themselves across the alkali metals. The first is the model calculates a larger temperature dependence than shown in experiments. The deviation of the temperature dependency of experimental data to the model continues to grow as the atomic number of the alkali metal increases. In addition, the relationship of the entropy correlation representing the largest amount of experimental data is also dependent on the alkali atomic number. The solubility experimental data in liquid lithium is closest aligned to the prediction where the entropy is neglected, while the data of liquid sodium, potassium, and rubidium show the entropy correlation is necessary. The model fails to provide any reasonable prediction for the liquid cesium results, as the experimental data is considerably higher than even the prediction with a correlation parameter of 1500 K. This information can then be utilized to provide a better understanding of the predicted results for the solubility of lanthanides in liquid sodium and liquid cesium.

### 7.1.4 Model Results for Ln Solubility

The enthalpies calculated by the Miedema model for the solubility systems studied in this thesis are shown in Table 6. Table 6 shows the enthalpy values from the Miedema model have a considerable greater dependence on the liquid alkali metal then the lanthanide.

**Table 6. Excess partial molar enthalpy of lanthanides in liquid alkalis calculated from the Miedema model.**

| Excess Partial Molar Enthalpy (Alkali-Lanthanide), $\Delta\bar{H}^{Ex}_{Lanthanide\ in\ liquid\ Alkali}$ (kJ/mol) | | |
|---|---|---|
| | Sodium-Lanthanide | Cesium-Lanthanide |
| Ce | 102 | 183 |
| Pr | 105 | 186 |
| Nd | 104 | 185 |

The modeled excess partial molar enthalpies across the three lanthanides for a specific liquid alkali metal all exhibit values within 2% of each other. The similarity of the excess partial enthalpy values for these three lanthanides exemplifies the physical and chemical behaviors commonly between these light lanthanides. Due to the comparable values in the enthalpies for the lanthanides in each liquid alkali, neodymium was chosen to show the temperature dependence of the solubility predicted by the model, as the other two lanthanides will have nearly identical predictions. Shown in Figure 39 are the results of the model for neodymium in liquid sodium and Figure 40 shows the results for liquid cesium. Based on the evaluation performed of this model a hypothesis of the expected solubility can be performed. For liquid sodium the experimental solubility of neodymium is expected to be around the prediction of Equation 44 with a correlation parameter of 3000 K. The predictions using an interaction parameter of 1500 K and entropy neglected providing a range for experimental scatter. For liquid cesium the neodymium solubility is expected to be considerably greater than the model's prediction, especially at the lower temperatures.

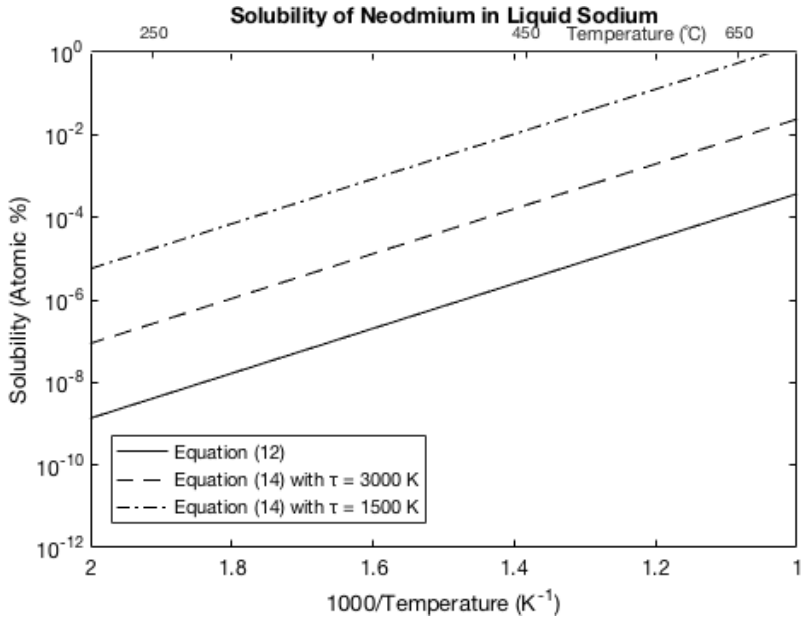


**Figure 39. Model prediction of the solubility of neodymium in liquid sodium.**

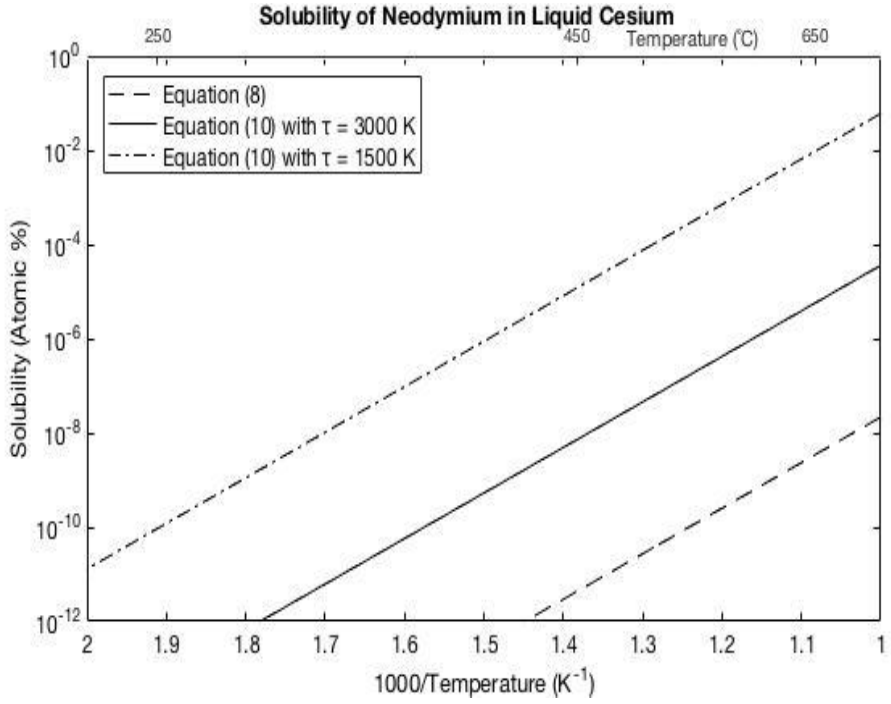


**Figure 40. Model prediction of the solubility of neodymium in liquid cesium.**

The trend of the failure of the Miedema model for the solubility in liquid cesium systems shown in Figure 41. The solubility measured, especially at the lower temperatures, is considerably higher than the predictions. In addition, while the temperature dependence in Figure 41 is larger than in previous experiments of metals in liquid cesium, it still is less than predicted by the model.

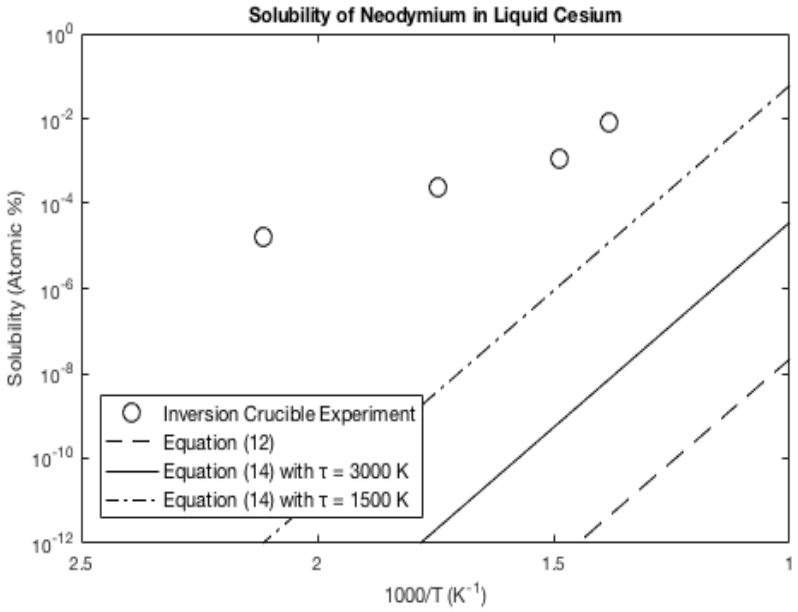


**Figure 41. Solubility of neodymium in liquid cesium compared between the Miedema model and experimental data in this thesis.**

## 7.1.5 Conclusion for the Model

For Summary, for liquid sodium, potassium, and rubidium the use of the enthalpy from the Mideama model with an interaction parameter for entropy correctly predicted a range for the solubility. However, the results of the model were much larger than experimental data for liquid lithium systems and much smaller than experimental data for liquid cesium systems. Thus the prediction was influenced greater by the Miedema model's effect of periodicity on the calculation of enthalpy for liquid alkali metal than experimental data suggests.

The model's predicted temperature dependence of the solubility was larger than the majority of experimental data. While several experimental results approached the temperature dependence predicted, the majority of data suggested a less dramatic impact of temperature on solubility. The predicted temperature dependence could be used as a maximum limit on the temperature dependence on solubility with the majority of practical applications experiencing a less pronounced dependence.

The increase of the model's solubility prediction can be accomplished in several ways. The parameters for cesium and lithium should be carefully examined in an attempt to reduce the periodicity the model causes for the liquid alkalis. Another consideration is in how the entropy term is represented. The use of an interaction parameter creates a large range of solubility but this range effectively captures experimental data scatter.

## 7.2 Ab-initio MD Calculation of Solubility

The present project has developed an An-initio MD model for calculating Ln solubility in liquid Na [99].

### 7.2.1 Computational Procedure

The solubility can be calculated from chemical potential calculation by using the Widom particle insertion method [100, 101].Ab-initio molecular dynamics (MD) method implemented in the Vienna ab initio simulation package (VASP) [102,103] is used for energy calculation.

The chemical potential is defined by:

$$\mu = \left(\frac{\partial F}{\partial N}\right)_{VT} \quad \text{Eq. 45}$$

where $F$ is the Helmholtz free energy in the canonical (NVT) ensemble. For $\mathrm{N} \gg 1$ we can approximate the partial derivative by a difference:

$$\mu = F(\mathrm{V}, \mathrm{T}, \mathrm{N}+1) - F(\mathrm{V}, \mathrm{T}, \mathrm{N}) \quad \text{Eq. 46}$$

The chemical potential can be approximated as a sum of the ideal gas term and the excess term:

$$\mu \approx \mu_{ideal} + \mu_{ex} \quad \text{Eq. 47}$$

The excess chemical potential can be written as an ensemble average [100]:

$$\mu_{ex} = -\mathrm{k_B T}\ \ln\left(\frac{1}{\mathrm{V}}\langle \int \exp\left(-\frac{\Delta \mathrm{U}}{\mathrm{k_B T}}\right) \mathrm{dr_{N+1}}\rangle_{\mathrm{N}}\right) \quad \text{Eq. 48}$$

where $\Delta \mathrm{U}$ is the potential energy change caused by particle insertion:

$$\Delta \mathrm{U}(\mathrm{r^N}, \mathrm{r_{N+1}}) = \mathrm{U}(\mathrm{r^{N+1}} = \{\mathrm{r^N}, \mathrm{r_{N+1}}\}) - \mathrm{U}(\mathrm{r^N}) \quad \text{Eq. 49}$$

In Widom particle insertion method, a test particle is randomly inserted into a configuration of N solvent A (here A is Na, Cs or Na-Cs mixture), and the energy difference $\Delta \mathrm{U} = \mathrm{U}(\mathrm{N}+1) - \mathrm{U}(\mathrm{N})$ will be recorded. The integral in Eq. 48 can be approximated by evaluating particle insertions in a grid with approximately 1 Å

spacing in the simulation box. Due to coulombic repulsion between adjacent atoms, the Boltzmann factor $\exp(-\frac{\Delta U}{k_B T})$ becomes negligible when the test particle is too close to the preexisting atoms. To improve the sampling efficiency, grid points are ranked based on their distance to the closest atom and Ab-initio MD energy calculations are only performed on the test particles inserted at grid positions that are furthest away from other atoms. It is found that only the top 10% grid points are needed to calculate the integral for satisfactory accuracy level [104].

Within the operating temperature range, the states of all three Ln elements are solid. The chemical potential change of Ln from pure Ln solid to the Ln-A solution $\Delta\mu_l$ can be represented by:

$$\begin{aligned}\Delta\mu_l\left(\mathrm{Ln_x}(A)_y; \mathrm{Ln}\right) &= \mu\left(\mathrm{Ln_x}(A)_y; \mathrm{Ln}\right) - \mu(\mathrm{Ln(s)}; \mathrm{Ln}) \\ &= \mu_{ex}\left(\mathrm{Ln_x}(A)_y; \mathrm{Ln}\right) - \mu_{ex}(\mathrm{Ln(s)}; \mathrm{Ln})\end{aligned} \qquad \text{Eq. 50}$$

with ideal gas contributions cancelled out. By continuously varying the concentration of the Ln in the Ln-A solution, the solubility can be obtained when $\Delta\mu_l\left(\mathrm{Ln_x}(A)_y; \mathrm{Ln}\right) = 0$.

Computational settings in VASP are stated as follows. A generalized gradient approximation (GGA) exchange correlation functional was used as parameterized by Pardew, Burke and Ernzerhov [105]. The cutoff energy was set to 500 eV with a Methfessel-Paxton smearing of width 0.2 eV [106] and a Hubbard U value of 5.4 eV [107]. The accuracy for the electronic energy convergence was set to $10^{-6}$ eV. The Brillouin zone was sampled through the gamma point which is acceptable for large and disordered systems just like this case [107]. The Ab-initio MD calculations were conducted in the canonical NVT ensemble with a time step of 1 fs. The Nose-Hoover thermostat was employed with a relaxation time of 20 fs and the temperature was set to 1000K. The systems were first run for 5 ps to reach equilibration before particle insertions are performed. Spin polarization effects were not considered in this calculation.

### 7.2.2 Results and Disscussion

The chemical potential change ($\Delta\mu_l$) of Ce in liquid Na was obtained by performing the insertions (1Ce in 256 Na, 1Ce in 128 Na, and 1Ce in (124 Na 4Ce)) and comparing the excess chemical potential with that from inserting (1Ce in 32 Ce) (see Figure 42). As can be seen, the zero point for the chemical potential change locates at around 0.4-

0.6 atomic percent, which gives the calculated solubility at a temperature of 1000K [99]. Considering the uncertainty in the simulation, however, we can only safely conclude that the solubility limit is lower than 0.78 atomic percent at 1000K [99].

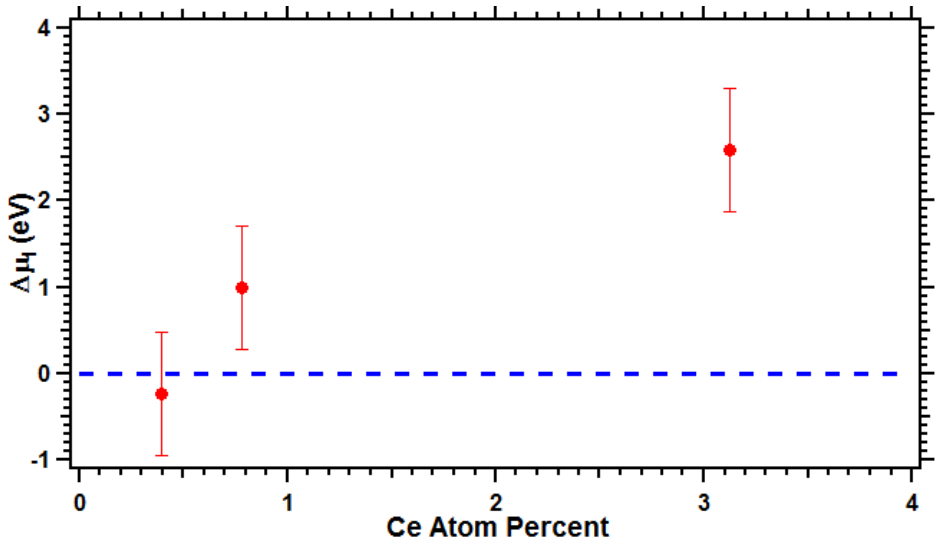


**Figure 42 Cerium chemical potential change upon solvation in a sodium melt depending on the molar concentration of cerium in the liquid sodium at 1000K.**

The calculated solubility is consistent with the known experimental results performed on similar materials at high temperatures. The solubility of Ln elements is low in liquid sodium on the basis of previous experimental and theoretical studies on rare earth elements, which are expected to have similar behaviors in alkali metals. Borestdt et al. [108] found that Ce and Sm have a solubility of about 0.3 at.% in liquid Lithium at 873 K. The authors also reported a solubility value around 0.3at.% for La in liquid Na at 873 K. and the solubility for Ho in liquid K at 873 K was reported to be about 0.3 at.% [108]. Lanthanides present poor miscibility with alkali metal melts in light of limited experimental data [108], which may be owing to the fact that Ln atoms are unlikely to form thermodynamically stable compounds with the alkali metal. In addition, a low solubility of Ln in Na can also be predicted from classical alloy theory. Interstitial solubility is expected to be fairly small since the solute atoms are larger than the interstitial sites in the lattice based on the Hume-Rothery interstitial solid solution rules. Substitutional solubility should also be very low due to the difference in the crystal structures and valences between the solute and solvent.

Except for the solubility calculation which is the purpose of the model developed, the model can also be applied to predict other fundamental information of Ln-Na system such as the heat capacity and radial distribution function [99], which are also important to understand Ln-Na interactions.

## 7.3 DFT-Phonon Calculation of Solubility

To further develop the temperature dependence of Ln solubility in various systems, DFT-Phonon calculations have been performed. This technique has been well developed and applied to calculate the solubility of rare-earth elements in solid solution such as aluminum [109] and magnesium [110]. Based on the experimental model "microscopic picture", we transferred such method to a liquid metallic solution case using the thermodynamic theory. This approach was verified by calculating Fe solubility in liquid Na and comparing it to the corresponding experimental data [111]. Our results showed a generally low value of Ln (Ce, Pr, Nd) solubility in liquid Na and Cs.

### 7.3.1 Methodology

*DFT-Phonon solubility calculation in solid solution*

Thermal properties of A-Ln mixture can be studied using the first-principles combined with phonon calculations. Here solvent A is Na, Cs or Na-Cs mixture. Based on the thermodynamic properties, we are able to calculate the solubility of Ln elements in A solvent. The vibrational contributions of the phonons are essential for calculating the temperature dependence of solubility [109]. Force constants of supercells are calculated by the density-functional perturbation theory (DFPT) implemented in VASP [109]. Phonon frequencies are calculated from the force constants through the PHONOPY code [112]. Within the quasi-harmonic approximation (QHA) framework in solid-solution, the phonon contribution to the vibrational free energy is expressed by [112]:

$$F_{ph}(T) = \frac{1}{2}\sum_{q,\nu} \hbar\omega_{\mathbf{q}\nu} + k_B T \sum_{q,\nu} \ln\left[1 - \exp\left(-\hbar\omega_{\mathbf{q}\nu}/k_B T\right)\right] \qquad \text{Eq. 51}$$

In this equation, we sum over all phonon branches with wave vectors $q$ in the first Brillouin zone and over all bands ($\nu$ is the band index), and $\omega_{q,\upsilon}$ is the frequency of the phonon with wave vector q and band index $\nu$. When the pressure is p=0, the enthalpy H reduces to lattice energy $E_o(V)$ and the Gibbs free energy can be written as [109]:

$$G = E_o(V) + F_{ph}(T;V) \qquad \text{Eq. 52}$$

Here $E_o(V)$ is the ground state energy at a certain volume.

The introduction of an impurity lanthanide atom into the solvent A will cause the total

free energy change which includes the effects from both enthalpy and entropy:

$$\Delta G = \Delta H - T\Delta S \quad \text{Eq. 53}$$

The free energy of the mixture will depend on the concentration of the Ln atoms, and the Ln saturation concentration will be that which gives the minimum free energy. If Ln saturation concentration is very small, the Ln-Ln interactions can be ignored and the increase in enthalpy of the system is directly proportional to the number of Ln atoms added [113], i.e.

$$\Delta H \cong \Delta H_{Ln} X_{Ln} \quad \text{Eq. 54}$$

where $X_{Ln}$ is the mole fraction of the Ln, $\Delta H_{Ln}$ is the enthalpy change per mole of Ln atoms added. There exist two contributions to the entropy change $\Delta S$ upon adding Ln atoms. One is the thermal entropy change $\Delta S_{Ln}$ per mole which results from the vibrational frequencies of the atoms around Ln. The other is from the change in the configurational entropy given by [113]:

$$\Delta S_{mix} = -R(X_{Ln}\ln X_{Ln} + (1 - X_{Ln})\ln(1 - X_{Ln})) \quad \text{Eq. 55}$$

where $R$ is the gas constant. The molar free energy of the mixture containing $\mathrm{X_{Ln}}$ mol of lanthanides atoms is therefore given by:

$$\begin{aligned} G &= G_A + \Delta G \\ &= G_A + \Delta H_{Ln} X_{\mathrm{Ln}} - T\Delta S_{Ln} X_{Ln} + RT(X_{Ln}\ln X_{Ln} + (1 - X_{Ln})\ln(1 - X_{Ln})) \end{aligned} \quad \text{Eq. 56}$$

The saturation concentration of lanthanides $X_{Ln}$ is therefore given by the condition:

$$\left.\frac{dG}{dX_{\mathrm{Ln}}}\right|_{X_{Ln}=X_{Ln}^{S}} = 0 \quad \text{Eq. 57}$$

Differentiating the Eq. 56 and making the approximation $X_{Ln}^{S} \ll 1$ yields

$$\Delta H_{\mathrm{Ln}} - T\Delta S_{Ln} + RT\ln X_{Ln}^{S} = 0 \quad \text{Eq. 58}$$

Therefore, the solubility $\mathrm{X_{Ln}^{S}}$ is obtained by [113]:

$$X_{Ln}^{S} = \exp(-\frac{\Delta H_{Ln} - T\Delta S_{Ln}}{RT}) = \exp(-\frac{\Delta G_{Ln}}{RT}) = \exp(-\frac{\Delta G_{\mathrm{Ln}-atom}}{k_B T}) \quad \text{Eq. 59}$$

where $\Delta G_{Ln}$ is the Gibbs free energy change from Ln per mole in the dilute solvent A. $\Delta G_{Ln-atom}$ is the Gibbs free energy change from Ln per atom in the dilute solvent A and can be obtained by performing DFT-Phonon energy calculations based on Eq. 52.

*Solubility conversion based on "Microscopic Picture"*

The previous DFT-Phonon solubility calculation method can be converted to a liquid metal solution case mainly on basis of an experimental model called "microscopic picture". A "microscopic picture" model based on an extensive series of experiments has been proposed to describe the metal behaviors in alloy formation. The following discussions about the enthalpies of formation are based on this model, for which more details can be obtained from the text book by F.R. deBoer et al. [114]. If intermetallic alloys of transition metals with non-transition metals $AB_n$ are sufficiently rich in *B* such that *A* atoms are completely surrounded by *B* neighbors, the enthalpy of formation for solution $AB_n$ equals the enthalpy changes at the dissimilar atomic interface [114]:

$$\Delta\overline{H}^{\circ solution}_{A\ in\ B} = \Delta\overline{H}^{\circ interface}_{A\ in\ B} \qquad \text{Eq. 60}$$

where [114]:

$$\Delta\overline{H}^{\circ interface}_{A\ in\ B} = V_A^{2/3}\frac{[-P(\Delta\phi^*)^2 + Q\left(\Delta n_{WS}^{\frac{1}{3}}\right)^2 - R^*]}{(n_{WS}^{-\frac{1}{3}})_{av}} \qquad \text{Eq. 61}$$

$\boldsymbol{V_A^{2/3}}$ is the molar surface area of metal A. $\boldsymbol{n_{WS}}$ is defined as the average electron density at the boundary of the Wigner-Seitz cell for the pure elements in the metallic state, $\boldsymbol{\Delta n_{WS}}$ is the difference in electron density of the two metals and $(\boldsymbol{n_{WS}^{-\frac{1}{3}}})_{av}$ is the mean value of $(\boldsymbol{n_{WS}^{-\frac{1}{3}}})_A$ and $(\boldsymbol{n_{WS}^{-\frac{1}{3}}})_B$ [114]. $\boldsymbol{\phi}^*$ is the work function of the pure metallic elements at the interfaces between dissimilar atoms and $\Delta\boldsymbol{\phi}^* = \boldsymbol{\phi}_A^* - \boldsymbol{\phi}_B^*$. *Q* is proportionality coefficient and P is a constant to be determined empirically, that contains the electronic unit of charge [114]. Three terms indicating multiple contributors to the enthalpy of formation on the right-hand side of Eq. 61 are explained as follows. The first term $-\boldsymbol{P}(\Delta\boldsymbol{\phi}^*)^2\boldsymbol{V_A^{\frac{2}{3}}}/(\boldsymbol{n_{WS}^{-\frac{1}{3}}})_{av}$ identifies the charge transfer effect visualized on an atomic scale. When two blocks of different metals are brought in contact, there will be net charge transfer governed by the difference in contact potential between the two metals [114]. Charge will flow to places of lower potential energy until

the resulting dipole layer compensates the potential difference [114]. The second term $\boldsymbol{Q}\left(\Delta \boldsymbol{n}_{\boldsymbol{WS}}^{\frac{1}{3}}\right)^{2} \boldsymbol{V}_{\boldsymbol{A}}^{\boldsymbol{2/3}}/(\boldsymbol{n}_{\boldsymbol{WS}}^{-\frac{1}{3}})_{\boldsymbol{av}}$ defines the mismatch of electron densities at the boundary between neighboring dissimilar atomic cells. The third term $\boldsymbol{V}_{\boldsymbol{A}}^{\boldsymbol{2/3}}\boldsymbol{R}^{*}/(\boldsymbol{n}_{\boldsymbol{WS}}^{-\frac{1}{3}})_{\boldsymbol{av}}$ is the additional enthalpy contribution originating from the combination of different types of metals: one metal with p-type electron wave functions and the other with mainly d-type wave functions [114]. $R^*$ is different for solid ($R_{solid}$) and liquid ($R_{liquid}$) and can be parameterized from the experimental results [114]. However, in the specific case where alkali metals are involved as the non-transition metals, $R^*$ equals to zero either for solid or liquid [114].

In our case with Ln as the inner transition metals (metal A) and Na or Cs as the non-transition metals (metal B), enthalpy of formation in both solid solution and liquid solution at the same temperature are equal based on Eq. 61 [114]:

$$(\Delta H_{A\ in\ nB})_{liquid} = (\Delta H_{A\ in\ nB})_{solid} \quad \text{Eq. 62}$$

Or equivalently:

$$H_{A-nB(liquid)} - (H_A + nH_{B(liquid)}) = H_{A-nB(solid)} - (H_A + nH_{B(solid)}) \quad \text{Eq. 63}$$

$$H_{A-nB(liquid)} - H_{A-nB(solid)} = n(H_{B(liquid)} - H_{B(solid)}) \quad \text{Eq. 64}$$

$$\Delta H_{fus,A-nB} = \Delta H_{fus,nB} \quad \text{Eq. 65}$$

Since the entropy of fusion can be described as [115]:

$$\Delta S_{fus} = \frac{\Delta H_{fus}}{T_f} \quad \text{Eq. 66}$$

where $\boldsymbol{\Delta H_{fus}}$ is the heat of fusion and $T_f$ is the melting temperature. With the approximation of metal A in metal B dilution, the influence of the A impurity on the melting temperature of metal B solution can be neglected, i.e. the melting temperature $T_f$ of $AB_n$ system and the melting temperature $\boldsymbol{T_f'}$ of pure metal $B_n$ system are equal, which yields:

$$\frac{\Delta H_{fus,A-nB}}{T_f} = \frac{\Delta H_{fus,nB}}{T_f'} \quad \text{Eq. 67}$$

$$\Delta S_{fus,A-nB} = \Delta S_{fus,nB} \quad \text{Eq. 68}$$

Equivalently:

$$S_{A-nB(liquid)} - S_{A-nB(solid)} = n(S_{B(liquid)} - S_{B(solid)}) \quad \text{Eq. 69}$$

$$S_{A-nB(liquid)} - (S_A + nS_{B(liquid)}) = S_{A-nB(solid)} - (S_A + nS_{B(solid)}) \quad \text{Eq. 70}$$

i.e.:

$$(\Delta S_{A\ in\ nB})_{liquid} = (\Delta S_{A\ in\ nB})_{solid} \quad \text{Eq. 71}$$

Based on Eq. 62, Eq. 71 and the Gibbs mixing energy described by Eq. 53, we have:

$$(\Delta G_{A\ in\ nB})_{liquid} = (\Delta G_{A\ in\ nB})_{solid} \quad \text{Eq. 72}$$

In light of the equations above, the solubility of $A$ in solid $B$ solution obtained from DFT-Phonon method is transferred to the temperature range where $B$ is in the liquid state.

### 7.3.2 Computational Details

Vienna Ab-initio Simulation Package (VASP) [103] is used in this work and the projector augmented wave (PAW) method is employed within the DFT framework [116]. Perdew-Burke-Ernzerhof (PBE) generalized gradient approximation (GGA) is used for the exchange-correlation functional. The first order Methfessel-Paxton's smearing method is used with a width of 0.1 eV to determine the partial occupancies for each wavefunction. The cutoff energy of 500 eV is applied and convergence of energy $10^{-6}$ eV is set. Spin polarization is considered for all calculations. Density functional perturbation theory (DFPT) implemented in VASP is utilized to calculate the force constant of supercell. A mesh of $6 \times 6 \times 6$ K-points sampling is applied. Based on force constants, phonon frequencies can be calculated through the PHONOPY code [112] to obtain vibrational thermodynamic properties which are important for solubility calculations. The DFPT method was utilized to calculate the force constants of systems, i.e. $AB_n$. The dilution of one impurity atom in Na was constructed by: the impurity

atom replacing the center site atom in a $3 \times 3 \times 3$ supercell with 54-atom cell of atom *B*. Such information was exploited to obtain the phonon frequencies and other thermodynamic properties.

### 7.3.3 Verification of Fe Solubility in Na

Fe solubility in pure Na was calculated in a temperature range of $650{\sim}900\mathrm{K}$ and compared with values from previous work. As shown in Figure 43, the data for Fe solubility from experiments are very scattered, which may be due to the fact that various measurements were conducted at different oxygen concentration levels. Oxygen level in liquid sodium appeared to possess very strong effects on the solubility of materials such as iron [117]. A correlation for solubility of Fe in Na at $658{\sim}997\mathrm{K}$ based on experimental measurements has been developed as a function of temperature by Stanaway and Thompson [118]. A low level of oxygen was achieved by uranium gettering. Borgstedt [119] reported the solubility with an oxygen concentration less than $1.0 \times 10^{-4}$ at. %. Thorley [120] estimated the solubility in an oxygen concentration of $1.4 \times 10^{-3}{\sim}1.4 \times 10^{-2}$ at. %. The trend with temperature as presented by our calculated values (no oxygen) was similar to those from experiments. Without any oxygen considered, our computational values are closer to the experimental results with low oxygen concentration such as reported by Stanaway [118].

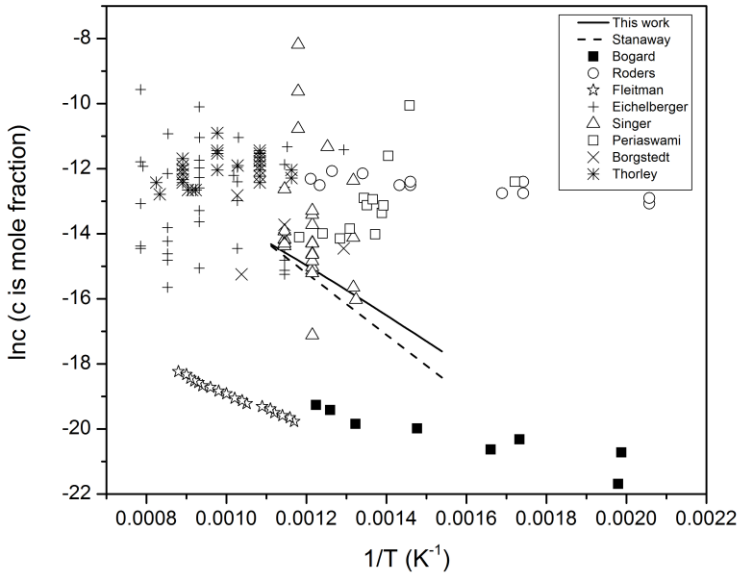


**Figure 43 [111] DFT-Phonon calculated solubility of Fe in Na compared with values from various references.**

### 7.3.4 Results and Discussion

As shown in Figure 44 and Figure 45, the Ln solubility in Na or Cs increases with increasing temperature. Ln has higher solubility in Cs than in Na. The experimental data for Nd solubility in Na are very scattered due to the uncertainties and are generally larger than the calculated values. Nd solubility in Cs, however, shows a similar trend with the simulation results though the values are still larger. A fitting of the simulation results to the Arrhenius equation is given as:

$$\ln C_s = \ln C_0 - \frac{Q}{k_B T} \qquad \text{Eq. 73}$$

where $C_0$ is the constant prefactor and Q is the heat in unit of eV. The fitting parameters values and the specific solubilities from both experiments and simulation at 723K are listed in Table 7. Our calculated solubility of $4.99 \times 10^{-7}$ at.% has shown consistence with a value of $2.8 \times 10^{-7}$ at.% from the previous experimental measurements of Ce solubility in sodium at 723 K [121]. Such low solubility conforms to the observation that cerium on the fuel periphery deposits from liquid metal mixture with a high concentration of sodium [122]. Generally, for the same composition the calculated solubility is lower than the value from experiments performed by Jeremy [123].

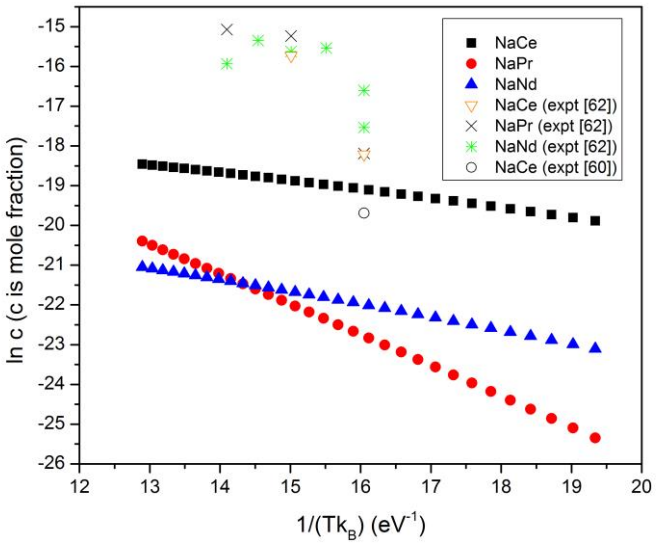


**Figure 44 DFT-Phonon calculation of temperature dependence of Ln solubility in liquid Na within a temperature range of 650K-900K. Multiple experimental results are included for comparison.**

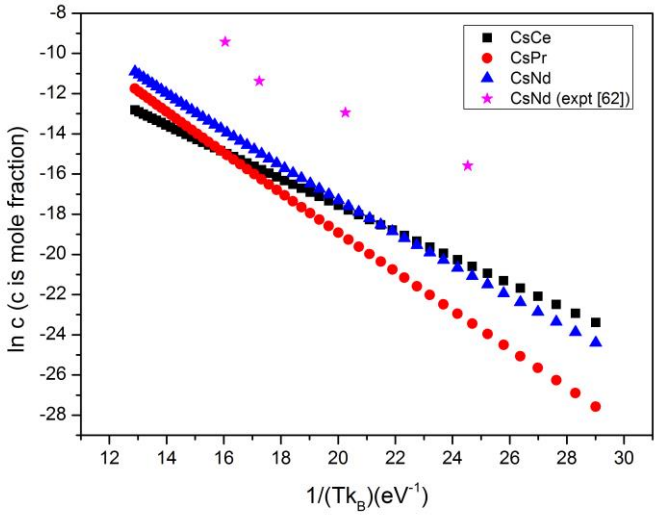


**Figure 45 DFT-Phonon calculation of temperature dependence of Ln solubility in liquid Cs within a temperature range of 400K-900K. Experimental results are included for comparison.**

**Table 7 Fitting Parameters of Ln solubility correspondence to the temperature in Na or Cs and the specific values at 723K.**

| System | Q (eV) | ln $C_0$ | Solubility (at. %) 723K | Expt (at.%) 723K |
|---|---|---|---|---|
| Ce in Na | 0.221 | -15.576 | 4.987E-7 | 2.80E-7 [121], 1.23E-6[123] |
| Ce in Cs | 0.667 | -4.224 | 3.261E-5 | - |
| Pr in Na | 0.767 | -10.476 | 1.261E-8 | 1.26E-6 [123] |
| Pr in Cs | 1.009 | 1.233 | 3.157E-5 | - |
| Nd in Na | 0.318 | -16.904 | 2.761E-8 | 2.43E-6~6.14E-6 [123] |
| Nd in Cs | 0.905 | 0.694 | 9.796E-5 | 8.12E-3 [123] |

As the solubility is calculated from the Gibbs mixing energy as given in Eq. 59, Ln solubility in Na-Cs mixture can be calculated from a weighted Gibbs mixing energy:

$$\Delta G_{mix} = X_{Na} \cdot \Delta G_{mix\_Na} + (1 - X_{Na}) \cdot \Delta G_{mix\_Cs} \qquad \text{Eq. 74}$$

where $\Delta G_{mix\_Na}$ is the Ln Gibbs mixing energy in pure Na and $\Delta G_{mix\_Cs}$ is the Ln Gibbs mixing energy in pure Cs. $X_{Na}$ is the mole fraction of Na in the Na-Cs liquid mixture. As an example, Ln solubility in Na(50.23 at%)-Cs is calculated (see Figure 46) and the corresponding fitting parameters are listed in
Table 8.

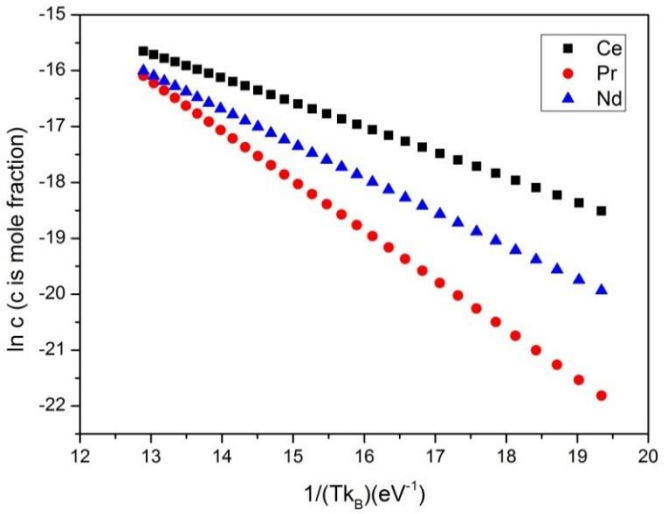


**Figure 46 DFT-Phonon calculation results of temperature dependence of Ln solubility in liquid Na (50.23 at%)-Cs within a temperature range of 600K-900K.**

**Table 8 Fitting Parameters of Ln solubility correspondence to the temperature in Na (50.23 at%)-Cs and the specific values at 723K.**

| System | Q (eV) | ln $C_0$ | Solubility (at. %) 723K | Expt (at.%) 723K |
|---|---|---|---|---|
| Ce in Na (50.23 at%)-Cs | 0.443 | -9.926 | 4.00E-6 | - |
| Pr in Na (50.23 at%)-Cs | 0.888 | -4.648 | 6.20E-7 | - |
| Nd in Na (50.23 at%)-Cs | 0.610 | -8.145 | 1.61E-6 | 4.23E-4 [123] |

To develop the correlation between solubility and temperature, DFT combined with phonon calculations were performed. With the method verified by the calculation of Fe solubility in liquid Na, we were able to develop solubility of Ln (Ce, Pr, Nd) in liquid Na, Cs and Na-Cs mixture as a function of temperature. Generally, Ln solubilities in these systems are extremely low and Ln has much higher solubility in Cs than in Na.

## 7.4 Calculation of Diffusivity

Diffusion coefficients of Ln in liquid metal systems such as Na, Cs and Na-Cs mixture are key data for investigation of Ln transport behaviors in metal fuels. The currently available data from experimental measurements is limited. By utilization of Ab-initio MD, the project calculated the Ln diffusivities in liquid Na and Cs and found that the diffusion coefficients are in the magnitude order of liquid diffusion ($10^{-5}$ $cm^2/s$) [124, 125 ]. Also the temperature dependence of the Ln diffusivity was developed.

Additionally, structural properties of Ln-Na and Ln-Cs systems were also investigated.

### 7.4.2 Methodology

The diffusion coefficient is defined as the proportionality constant between the molar flux of a component in a system and the concentration gradient that gives rise to this flux. Ab-initio MD method implemented in VASP is applied to determine the diffusion coefficient of lanthanides in liquid alkali metals at a specific temperature. The settings in VASP are similar to those used in the previous Ab-initio calculations of Ln solubility. The molecular dynamic model of liquid metal was constructed by the supercell with 128 atoms in total. Four Ln atoms were introduced replacing Na atoms to constitute binary alloy systems since only the case with low Ln concentration is of interest in the reactor application.

According to Stokes-Einstein equation [126], the diffusion coefficient $D$ can be calculated from the mean-square displacement $\sigma(\mathrm{t})$:

$$D = \lim_{\mathrm{t}\to\infty} \frac{\sigma(\mathrm{t})}{6\mathrm{t}} \qquad \text{Eq. 75}$$

The averaging mean-square displacements should be obtained from VASP after a long enough period of simulation. As pointed out by Yurev [127], a simulation time more than 10 ps is sufficient. The temperature dependence of diffusion coefficient is governed by the Arrhenius equation:

$$\ln D = \ln D_0 - \frac{Q}{k_B T} \qquad \text{Eq. 76}$$

where $T$ is temperature, $R$ is the gas constant. $D_0$ is the temperature-independent pre-exponential factor. $Q$ is the activation energy for diffusion.

### 7.4.3 Results and Discussions

Figure 47 shows the calculation of diffusion coefficient for Ce in liquid Na at 723K by recording mean square displacements of four Ce atoms in the liquid metallic system of 124 Na atoms for more than 50 ps. The Ln diffusivities at multiple temperatures were calculated from the slope of the fitting data as listed in Table 9. The diffusion coefficients of Ln in either liquid Na or liquid Cs were all found to be in the liquid diffusion magnitude order of $10^{-5}\mathrm{cm}^2/\mathrm{s}$. Moreover, the diffusivity for each metallic system showed an increasing trend with the increasing temperature as expected. A summary of diffusivity dependence on temperature is presented in Figure 48 and is

fitted to the Arrhenius equation with corresponding parameters listed in Table 10. Although the corresponding experimental values are still lacking, our calculated results are consistent with other experimental results for diffusion of specific element in similar systems at elevated temperatures. For example, the diffusion of Cerium oxy ions in $MgCl_2 - NaCl - KCl$ eutectic at a temperature of 853K was reported to have a diffusion coefficient in the magnitude order of $10^{-5}\mathrm{cm}^2/\mathrm{s}$ in previous experimental studies [128]. In addition, a classical molecular study of the Na-K alloy reported a calculated value of $4.77 \times 10^{-5}\mathrm{cm}^2/\mathrm{s}$ in for the diffusivity of K in the $\mathrm{Na_{90}Li_{10}}$ system at 373K [129].

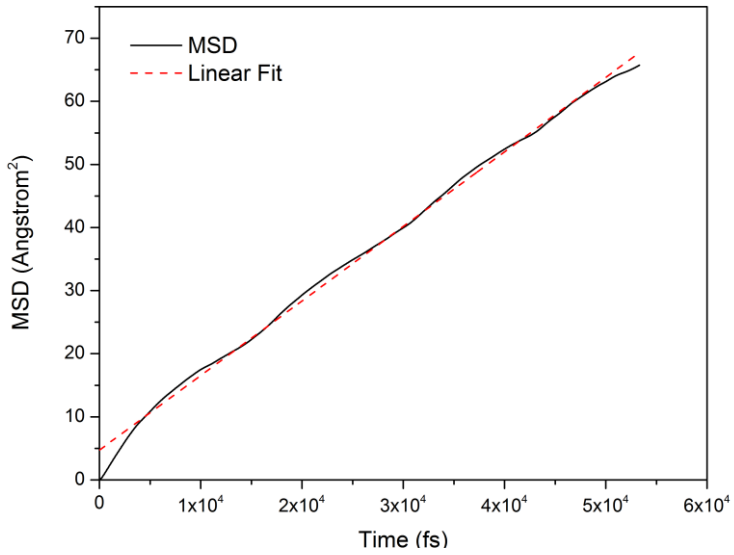


**Figure 47 The example mean squared displacements of 4 Ce atoms in 124 Na atoms at 723K are recorded against time in femtoseconds.**

**Table 9 Ln diffusivity in liquid Na or Cs metallic system at different temperatures.**

| System | Temperature (K) | Diffusivity($\mathrm{cm}^2/\mathrm{s}$) $\times 10^5$ |
|---|---|---|
| **Ce in Na** | 723 | $1.97 \pm 0.07$ |
| | 848 | $2.83 \pm 0.22$ |
| | 1000 | $5.33 \pm 0.04$ |
| **Ce in Cs** | 723 | $1.59 \pm 0.01$ |
| | 848 | $2.00 \pm 0.07$ |
| | 923 | $2.71 \pm 0.06$ |
| **Pr in Na** | 723 | $4.53 \pm 0.16$ |
| | 848 | $6.36 \pm 0.10$ |
| | 923 | $8.67 \pm 0.17$ |
| **Pr in Cs** | 723 | $1.33 \pm 0.10$ |
| | 848 | $2.02 \pm 0.17$ |
| | 923 | $3.03 \pm 0.07$ |
| **Nd in Na** | 723 | $4.00 \pm 0.16$ |

| | | |
|---|---|---|
| | 848 | $5.09 \pm 0.24$ |
| | 923 | $6.13 \pm 0.05$ |
| | 723 | $1.76 \pm 0.07$ |
| **Nd in Cs** | 848 | $2.66 \pm 0.03$ |
| | 923 | $3.20 \pm 0.13$ |

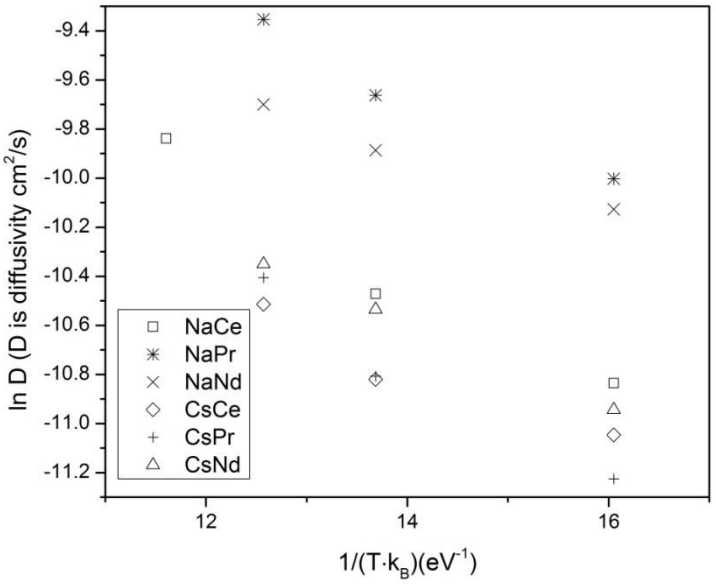


**Figure 48 Ln diffusivity corresponding to the temperature in Na or Cs each at three temperatures.**

**Table 10 Parameters of Ln diffusivity as a function of the temperature in Na or Cs.**

| System | Ln $D_0$ | Q (eV) |
|---|---|---|
| NaCe | -7.315 | 0.223 |
| CsCe | -8.765 | 0.144 |
| NaPr | -7.135 | 0.180 |
| CsPr | -7.620 | 0.226 |
| NaNd | -8.219 | 0.120 |
| CsNd | -8.197 | 0.171 |

The structural properties of the Ln-Na and Ln-Cs liquid alloy systems are characterized by the form of its pair correlation function (PCF) as shown in Figure 49 and Figure 52 separately. The total pair correlation functions g(r) of Na-based metallic systems calculated by [130]:

$$g(\mathrm{r}) \approx c_{NaNa}g_{NaNa}(r) + c_{NaLn}g_{NaLn}(r) + c_{LnNa}g_{LnNa}(r) + c_{LnLn}g_{LnLn}(r) \quad \text{Eq. 77}$$

where $g_{ij}(r)$ are four partial pair distribution functions of Na-Na, Na-Ln, Ln-Na, Ln-Ln pairs. The weighting factors can be expressed as $x_i x_j Z_i Z_j/(x_{Na}Z_{Na} + x_{Ln}Z_{Ln})^2$ with the atomic number of an atom $i$, $Z_i$ and the corresponding concentration $x_i$. The total PCF for Cs-based systems can be obtained in a similar way. The height of the peaks of $g(\mathrm{r})$ decreases and the peak position shifts to a shorter distance with increasing temperature. This observation agrees with the results from a previous study on the simulation of liquid alkali metals [131]. As observed from Figure 49, no well-defined first coordination shell is observed in the $g(r)$ for pure liquid Na, which indicates the deviation from a crystal structure. The liquid binary alloys, Na-Pr and Na-Nd, both show a similar shape of PCF as liquid Na and therefore present approximately homogeneous metallic properties. In the Na-Ce binary system, however, an extra peak at a distance of around $2.65\text{Å}$ at 723K indicates the appearance of segregation phenomena. This peak was found to be mainly attributed to the contribution from the partial pair correlation function, $g_{CeCe}(r)$ with a peak indicating aggregation of the Ce atoms and the Ce separation from the Na solvent atoms (see Figure 50). The Na-Ce atomic configuration after 60 ps simulation in Figure 51 indicates that all the four Ce atoms tend to gather together during diffusion. Such segregation phenomenon is caused by the rejection of the solutes from a solidified alloy into the liquid phase due to different impurity solubility in liquid and solid phases at the equilibrium temperature. Segregation can be used for predicting the solidification [132] and the degree of segregation is influenced by the chemical composition of the alloy [133]. Thereby, the Na-Ce alloys at current temperatures are expected to be in the amorphous solid state while Na-Pr and Na-Nd still maintain liquid features. In Cs-based systems (see Figure 52), a small peak at a distance of around $2.5\text{Å}$ has been observed which indicates the emerging segregation phenomena. However, the effects seem much smaller compared with the Na-based systems, which may be due to shielding effects from the large size of Cs solvent atoms. Thereby, the Ln-Cs systems appear to present typical characteristics of a liquid state.

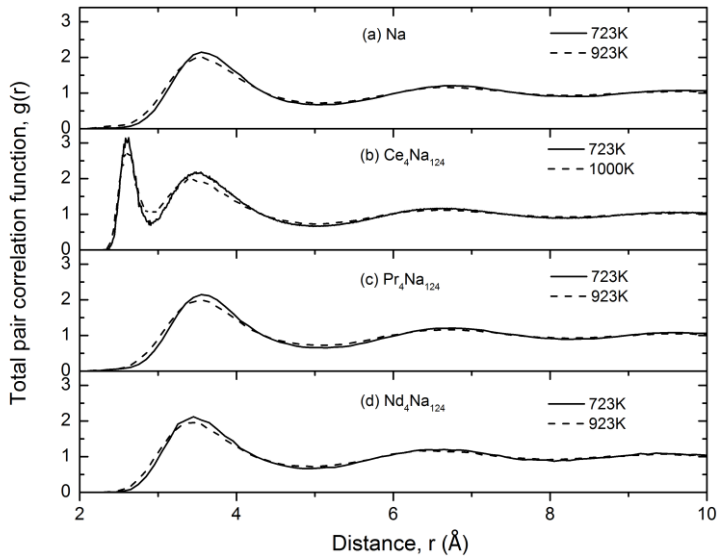


**Figure 49 The total pair correlation functions *g(r)* of four Na based liquid metallic systems. PCF are calculated at two temperatures for each metallic system.**

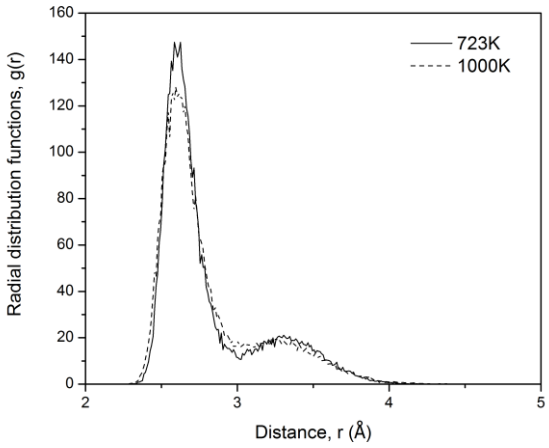


Figure 50 The Ce-Ce pair correlation functions *g(r)* at two temperatures.

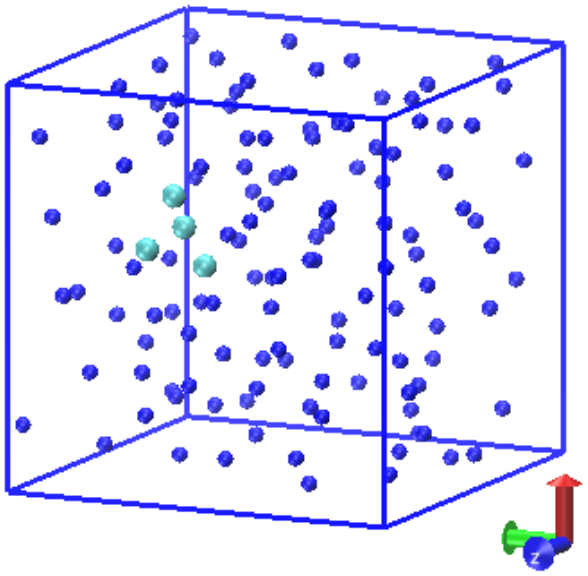

Figure 51 A snapshot of atomic structure of $Ce_4Na_{124}$ system after 60 ps at 723K with four Ce (cyan atoms) aggregated.

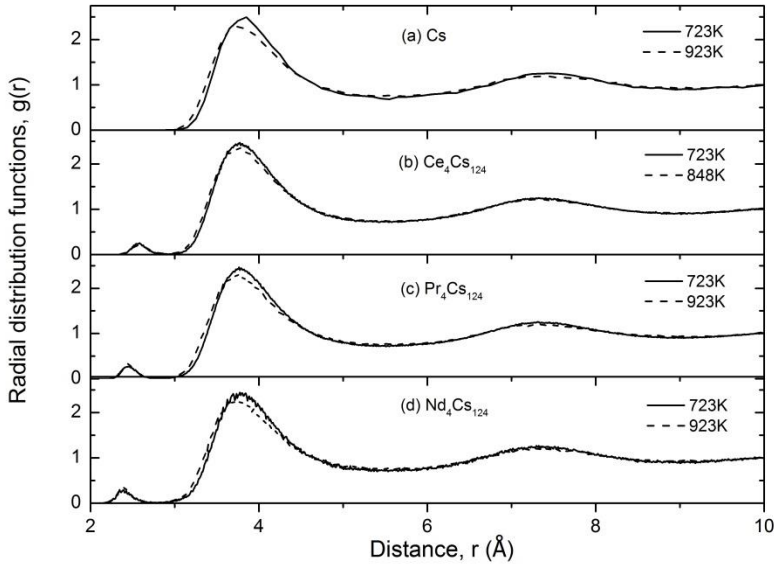


**Figure 52 The total pair correlation functions *g(r)* of four Cs based liquid metallic systems. PCF are calculated at two temperatures for each metallic system.**

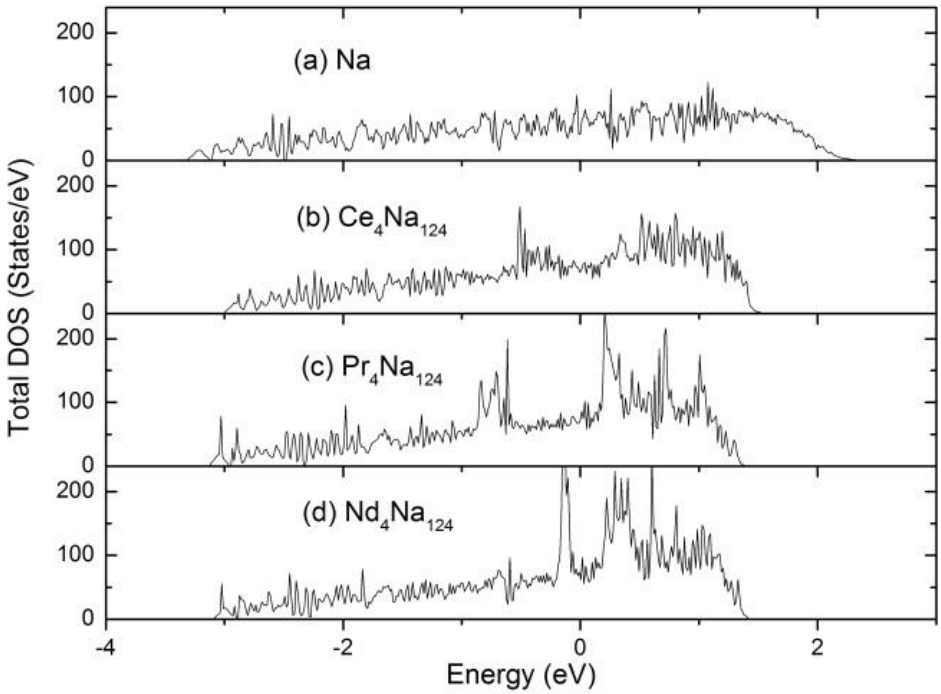


**Figure 53 The electronic density of states (DOS) of four liquid metallic systems at 723K. The origin of the energy is adjusted to be the Fermi level.**

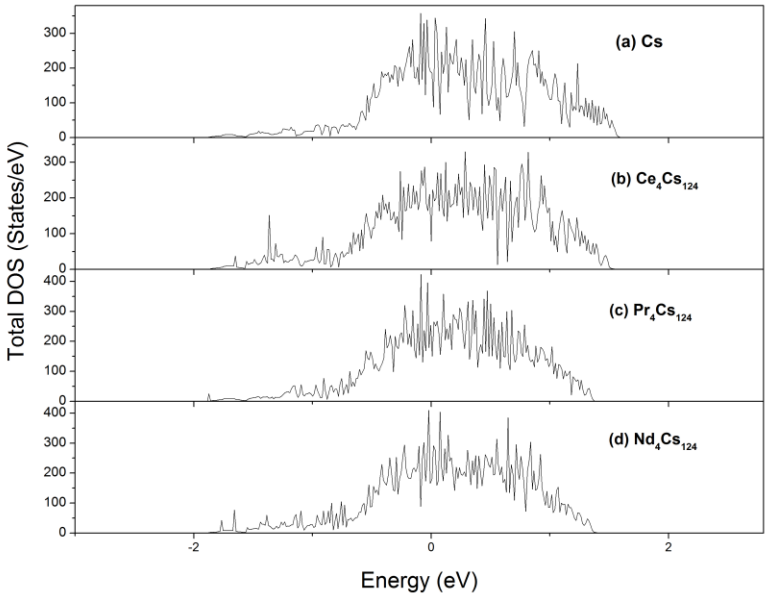


**Figure 54 The electronic density of states (DOS) of four liquid metallic systems at 723K. The origin of the energy shifts to be the Fermi level.**

The electronic density of states (DOS) can be calculated based on current model. DOS of four different liquid metallic configurations after 5ps equilibration is presented in Figure 53 for Ln-Na and Figure 54 for Ln-Cs with the energy origin adjusted to be

Fermi level ($E_F = 0$). The impact of the Ln impurity on the DOS of Cs is not as obvious as that in the Na based metal system. However, we can still discover that the inclusion of Ln atoms makes DOS more concentrated around the Fermi energy. Similar characteristics of DOS were also obtained from the previous DFT calculation of electronic structures of Ce impurities in different metal atoms such as Cu, Ag and Pd [134].

### 7.4.4 Calculation of Diffusivity in Na-Cs Mixture

In previous studies [135], several models have been proposed for relating diffusivity in the mixture with specific composition to diffusivity in an infinitely dilute solution ${D_i}^{x_j \to 1}$:

$$D_i = \sum_{j=1}^{n} x_j {D_i}^{x_j \to 1} \quad \text{Eq. 78}$$

$$D_i = \sum_{j=1}^{n} w_j {D_i}^{w_j \to 1} \quad \text{Eq. 79}$$

$$D_i = \sum_{j=1}^{n} v_j {D_i}^{v_j \to 1} \quad \text{Eq. 80}$$

$$\frac{1}{D_i} = \sum_{j=1}^{n} \frac{x_j}{{D_i}^{x_j \to 1}} \quad \text{Eq. 81}$$

where $x_j$ is the mole fraction, $w_j$ is the mass fraction, $v_j$ is the volume fraction. ${D_i}^{x_j \to 1}$ is the self-diffusivity of component *i* in an *i-j* mixture when mole fraction of component *j* is approaching one. ${D_i}^{w_j \to 1}$ and ${D_i}^{v_j \to 1}$ have similar meaning but are related to $w_j$ and $v_j$ correspondingly. Combined with the obtained diffusivity in pure Na and Cs, Ln diffusivity in Na-Cs with any composition can be easily calculated.

### 7.4.5 Conclusion

Ab-initio MD was employed to calculate the diffusion coefficients of Ln (Ce, Pr, Nd) in liquid Na and Cs. Ln diffusivity in Na-Cs mixture can be obtained from the previously established models. The structural properties of Ln-Na and Ln-Cs binary

metallic at different temperatures have also been reported. The total pair correlation functions for Na-Ce indicate an amorphous state while the other systems appear to be in the liquid state at typical reactor operation temperatures.

# 8. MOOSE/BISON Modeling of Ln Transport in Pore Scale

## 8.1 Introduction

In the U-Zr fuel, liquid metal filled pores can form, connect with each other and reach the fuel surface. These pores may accelerate the transportation of lanthanide (Ln) fission products to the fuel periphery, giving rise to FCCI. With utilization of MOOSE/BISON code, a model has been established to quantitatively study the Ln transport behaviors in pore-scale. By constructing multiple kernels in MOOSE to capture the physics like precipitation process and implementing the corresponding boundary conditions to describe the inter-reaction or inter-diffusion at different interfaces, Ln concentration distribution in different media can be reflected from simulation. MOOSE/BISON code is based on finite element method (FEM).

MOOSE (Multiphysics Object Oriented Simulation Environment) is an object-oriented C++ finite element-based framework developed in Idaho National Lab to solve systems of coupled non-linear partial differential equations [136]. By combining computer science with a strong underlying mathematical description through a unique approach, MOOSE serves as a software toolkit to development of engineering simulation codes [137]. The mathematical principle of Jacobian-free Newton–Krylov (JFNK) [138] forms the foundation of MOOSE in which the set of partial differential equations (PDE) to be solved are written in a weak form [139].

A schematic of MOOSE structure is shown in Figure 55. Based on JFNK implementation requiring only residual evaluations of the discrete system, MOOSE takes a modular architecture providing a convenient way to add and couple various physics together with material properties and boundary conditions handed consistently [136]. Residing underneath the physics layer, MOOSE provides a set of core functionality necessary for residual and Jacobian evaluation [136]. Moreover, MOOSE employs the interfaces in libMesh, which is a finite element framework developed by the CFD Lab at the University of Texas in Austin [140]. Diverse large scale parallel computing resources can be used through libMesh with a set of utilities for massively parallel finite element based computations such as mesh I/O, a FEM library, and interfaces to solver packages such as PETsc and SNES [136]. To develop new applications, only the kernel development is required from the developers. MOOSE is designed to do everything else for the application developer, such as finite element discretization of the PDEs, the nonlinear solver, and the parallel high performance computing [137].

A practical calculation in MOOSE is mainly achieved by setting up three important modules: kernels, boundary conditions and materials. Physics expressions are modularized into kernels and each kernel must supply a residual but may provide a Jacobian optionally [136]. These kernels are combined at run time into complete residuals describing the problem to be solved [137]. MOOSE supplies an extensive library of kernels describing solid mechanics, phase field models and more [137]. Boundary Conditions represent constraints of variables with residuals and Jacobians being evaluated on boundaries. Several typical Boundary Conditions are included in MOOSE itself such as Dirichlet and Neumann type boundary conditions [136]. The material system enables the creation of material objects which calculate the material properties before kernels compute residuals, with different materials properties applied to different subsets of the domain [136].

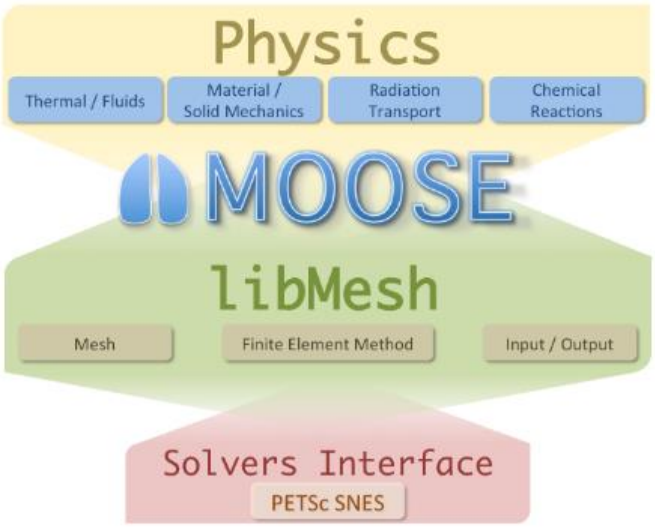


**Figure 55 [139] MOOSE structure**

BISON is a modern multidimensional Multiphysics finite-element based nuclear fuel performance code built on MOOSE [141]. With the applicability to analyze both steady and transient fuel behaviors and also geometries of various dimensions including 1D (spherically symmetric) or 2D (axisymmetric and plane strain) or 3D geometries, BISON has been widely employed to investigate a variety of fuel forms such as LWR oxide fuel [141] and metallic fuel in both rod and plate geometries [142]. BISON supplies a variety of governing equations including fully-coupled partial differential equations for energy, species, and momentum conservation [141]. To account for both nonlinear kinematics and nonlinear material behaviors, BISON implemented a variety of constitutive laws such as $UO_2$ temperature and burnup dependent thermal

properties, solid and gaseous fission product swelling, fuel thermal and irradiation creep, cladding thermal and irradiation creep and irradiation growth, fuel-clad gap mechanics [141]. The metallic fuel modeling capability in BISON is under development and multiple efforts have been reported such as constituent distribution model implemented into the BISON for solving Zirconium migration problems [143,144].

## 8.2 Ln Transport in a Single 1-D Tubular Pore Connected to Na

There are three serial steps in the Ln migration process: solid-state diffusion through solid fuel, reactions at the solid/liquid interface and liquid-state diffusion through the pore. Ln generated in the solid fuel will diffuse through the solid towards the solid-liquid interface driven by the concentration and temperature gradients. The Ln reaction kinetics at the interface is represented by the corresponding boundary conditions. The dissolved Ln solute in the liquid bulk will transport away from the interface following the Fick's law including Soret effects. The precipitation process as a result of limited Ln solubility will occur everywhere.

Assumptions:

1. Three kinetics are included at the interface: interface reactions occur between dissolved Ln in the fuel and in the pore and such interface reactions are reversible in the direction of absorption or desorption. Ln precipitation in the fuel can also dissolve into the liquid metal filled pore at the interface. Also there is inter-diffusion between dissolved Ln in the fuel and Ln precipitate in the liquid metal.
2. Solubility only depends on temperature.
3. The diffusion coefficient of a species in solution only depends on the temperature.
4. Precipitation kinetics in the fuel is assumed to be diffusion limited and is approximated by Ln solute reaction with widely spaced discrete spherical Ln sinks.
5. Ln precipitates have zero diffusivity.
6. Ln is generated in the fuel at a constant rate $\dot{q}$ uniformly.
7. Ln precipitates are suspended in the corresponding media.

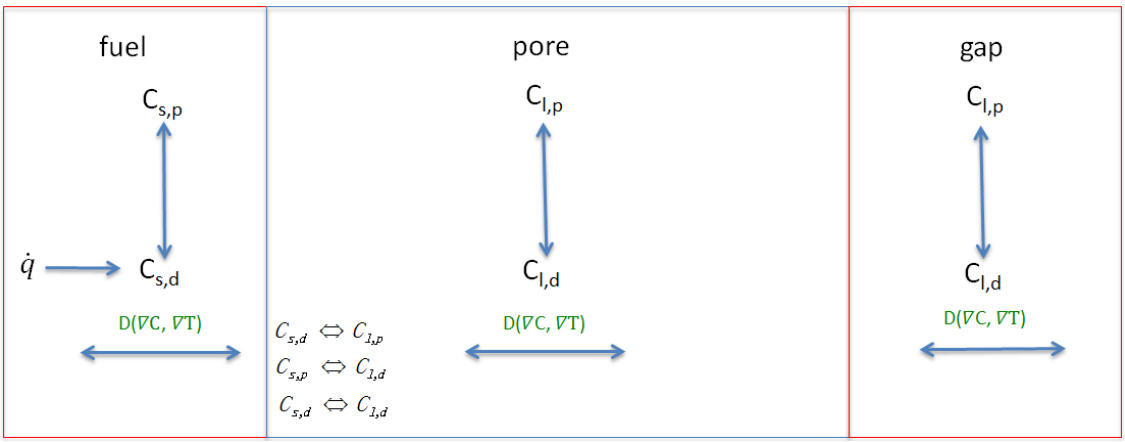


**Figure 56 Schematics of Ln diffusion and reactions in a pore scale with the temperature decreasing from left to the right.**

As shown in Figure 56, four different Ln concentrations are defined as variables and restricted in corresponding blocks: precipitated concentration Ln in the fuel $C_{s,p}$ and dissolved Ln concentration in the fuel $C_{s,d}$ exist in the fuel block; precipitated Ln concentration in the liquid metal $C_{l,p}$ and dissolved Ln concentration in the liquid metal $C_{l,d}$ are in the pore and the gap. At the beginning, Ln is generated as dissolved Ln in the fuel. The dissolved Ln will precipitate out as Ln precipitation once it goes above the solubility limit or the super-saturated conditions are changed. The liquid-state precipitation occurs in the liquid metal solution. The reaction between dissolved Ln in the fuel and the pore occurs at the fuel-pore interface and is approximated by first-order kinetics model [145]. Similarly, Ln precipitation on the fuel side of the fuel/pore interface can dissolve into the pore following the first-order kinetics. As related to Ln chemical potential, Ln solubility in different media is used to determine the Ln flux across the interface. Just as a diffusion couple, the inter-diffusion between dissolved Ln in the fuel and Ln precipitation in the pore will start after the precipitation forms on the fuel/pore interface.

Two diffusion coefficients will be used in different blocks correspondingly. The liquid-state diffusivity $D_l$ is used for $C_{l,d}$ in the pore, while the solid-state diffusivity $D_s$ applies to $C_{s,d}$ diffusion in the fuel. The Soret effects are included for the diffusion process with the respective heat of transport $Q^*$. Soret can drive the diffusion along the temperature gradient. The Soret effects in metallic systems have been investigated in the previous studies [146,147].

For the present calculation, the concentration has a unit atoms/$\mu m^3$**.**

### 8.2.1 Pore-Scale Model Implementation in MOOSE

Block restricted variables will be utilized and four variables for Ln concentration will

be used: dissolved Ln concentration in solid $C_{s,d}$ and in liquid $C_{l,d}$; precipitated Ln concentration in solid $C_{s,p}$ and in liquid $C_{l,p}$. The temperature is introduced as an auxiliary variable and a specific temperature profile is applied. Ln precipitation process is described by the "Precipitation" kernel while the various reactions at the interface are described by the corresponding interfacekernel. Kernels are selectively applied in corresponding blocks to make up the kinetic equations. The respective reaction rate constants or factors are implemented as the material properties in various blocks. The diffusivity and solubility are correlated to the temperature by the Arrhenius equation. The kernels implementation in MOOSE is shown in Figure 57:

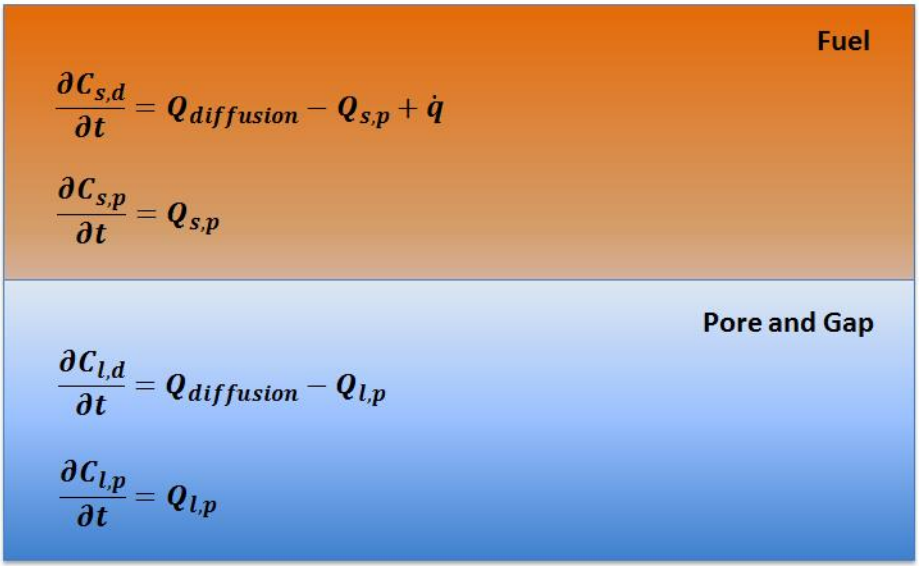


**Figure 57. Applied kernels in MOOSE for a pore-scale model of Ln transport.**

### 8.2.2 Ln Kinetics in Different Blocks

Precipitation kinetics in the fuel

The precipitation kinetics in the fuel can only occur when the total Ln concentration is less than the atomic number per volume of pure Ln, i.e. $C_{s,p} + C_{s,d} < C_{Ln\_pure}$. The first-order kinetics is used to describe the excess Ln solute in the solution [148,149]. The equation indicates that the precipitation can only occur when the solution is over-saturated. The precipitation process can be divided into two steps: nucleation and growth [149]. The nucleation originates from oversaturated Ln and more Ln can be absorbed by formed nucleation serving as sinks. With Ln sinks widely spaced in the U-Zr fuel, the mobile Ln solutes will transport and react with discrete sinks spaced in the crystal [150]. Considering the small values of solid-state diffusivity, we assume the reaction is relatively rapid and such precipitation kinetics is diffusion limited. The rate constant for diffusion controlled reaction between a Ln solute and a spherical sink with radius $R$ can be simplified as: $4\pi R C_{sink} D_{s,d}$, where $C_{sink}$ is the number of sinks formed in a unit volume [150]. The precipitation rate is linear to the oversaturated Ln

concentration [150]. The Ln precipitation rate in the fuel can be described by:

$$Q_{s,p} = \begin{cases} 4\pi R C_{sink} D_{s,d}\left(C_{s,d} - C_{s,d}^{0}\right) & \left(C_{s,d} > C_{s,d}^{0}\ \right) \\ 4\pi R C_{sink} D_{s,d}\left(C_{s,d} - C_{s,d}^{0}\right)\dfrac{C_{s,p}}{C_{Ln\_pure}} & \left(C_{s,d} \le C_{s,d}^{0}\right) \end{cases} \quad \text{Eq. 82}$$

As indicated by Eq. 82, Ln precipitation can start after the Ln concentration goes beyond the solubility limit. If no Ln deposits out and the Ln in the fuel is under-saturated, no precipitation will occur. However, if the dissolved Ln concentration in the fuel becomes lower than the solubility after some Ln precipitates already form, the reaction rate will become negative indicating the precipitated Ln will redissolve into the fuel.

Precipitation kinetics in the pore

The precipitation kinetics in the pore can only occur when the total Ln concentration is less than the atomic number per volume of pure Ln, i.e. $C_{l,p} + C_{l,d} < C_{Ln\_pure}$.

$$Q_{l,p} = \begin{cases} k_{l,p} \cdot \left(C_{l,d} - C_{l,d}^{0}\right) & \left(C_{l,d} > C_{l,d}^{0}\ \right) \\ k_{l,p} \cdot \left(C_{l,d} - C_{l,d}^{0}\right)\dfrac{C_{l,p}}{C_{Ln\_pure}} & \left(C_{l,d} \le C_{l,d}^{0}\right) \end{cases} \quad \text{Eq. 83}$$

A similar kinetics as precipitation in the fuel is used for Ln precipitation in the liquid metal solution as shown in Eq. 83. With no crystal structure in the liquid metal solution, $k_{l,p}$ is used as a rate constant for precipitation. The Ln precipitation behaviors are similar to those in the fuel.

Interface reaction at the solid-liquid-interface

Multiple interface reactions are introduced as the boundary conditions at the fuel/liquid-metal interfaces. Each flux of a certain Ln concentration variable at the interface is constituted by fluxes from different reactions:

$$J_{s,p} = -J_{s,p\to l,d} \quad \text{Eq. 84}$$

$$J_{s,d} = -J_{s,d\to l,d} - J_{s,d\to l,p} \quad \text{Eq. 85}$$

$$J_{l,p} = J_{s,d\to l,p} \quad \text{Eq. 86}$$

$$J_{l,d} = J_{s,d\to l,d} + J_{s,p\to l,d} \quad \text{Eq. 87}$$

*a) Absorption/desorption between Ln solutes in the fuel and in the liquid metal*

The reaction at the interface between dissolved Ln in the fuel and in liquid metal is described by the driving force factor $F_{s,d\to l,d}$ as:

$$F_{s,d\to l,d} = k_{dr}^{s,d\to l,d} C_{s,d} - k_{dr}^{l,d\to s,d} C_{l,d} \quad \text{Eq. 88}$$

where $k_{dr}^{s,d\to l,d}$ is the driving force coefficient for Ln desorption from Ln solute in the fuel to Ln solute in the liquid metal solution. $k_{dr}^{l,d\to s,d}$ is the driving force coefficient for Ln absorption from Ln solute in the liquid metal to Ln solute in the fuel. A balance can be established when Ln saturation concentration is reached at the interface:

$$F_{s,d\to l,d} = k_{dr}^{s,d\to l,d} C_{s,d}^{0} - k_{dr}^{l,d\to s,d} C_{l,d}^{0} = 0 \quad \text{Eq. 89}$$

which yields:

$$k_{dr}^{l,d\to s,d} = \frac{k_{dr}^{s,d\to l,d} C_{s,d}^{0}}{C_{l,d}^{0}} \quad \text{Eq. 90}$$

Substituting Eq. 90 into Eq. 88 yields:

$$F_{s,d\to l,d} = k_{dr}^{s,d\to l,d} C_{s,d}^{0} \left(\frac{C_{s,d}}{C_{s,d}^{0}} - \frac{C_{l,d}}{C_{l,d}^{0}}\right) \quad \text{Eq. 91}$$

Therefore, the Ln flux direction should be determined by using the degree of Ln saturation on each side of the interface. The flux from Ln solute in the fuel to the Ln solute in the liquid metal is expressed as:

$$J_{s,d\to l,d} = \widetilde{D} F_{s,d\to l,d} \left(1 - \frac{C_{l,p}}{C_{Ln\_pure}}\right)\left(1 - \frac{C_{s,p}}{C_{Ln\_pure}}\right) \quad \text{Eq. 92}$$

where $\widetilde{D}$ is the effective Ln diffusion coefficient across the interface. Since the slow solid- state diffusion should dominate in this process, $\widetilde{D}$ is taken as the Ln solid-state diffusion coefficient in the fuel, i.e. $\widetilde{D} = D_{solid}$. Since such reaction can only occur at locations where the fuel is in direct contact with the liquid metal solution, the reaction rate will decrease as more Ln precipitation from the liquid metal solution cover the

surface of the fuel. This rate reduction is described by introducing the term: $1 - \frac{C_{l,p}}{C_{Ln\_pure}}$. Similarly, the precipitation from the fuel at the interface may also have barrier effects, which are introduced as the term: $1 - \frac{C_{s,p}}{C_{Ln\_pure}}$.

*b) Interface reaction between Ln solute on the fuel surface and Ln precipitates from liquid metal solution*

As the Ln in the liquid metal precipitates out on the surface of the fuel, a Ln/U-Zr diffusion couple is formed. The inter-diffusion kinetics between dissolved Ln in the fuel and Ln precipitation in the pore applies at the fuel/pore interface, which is described by the driving force factor $F_{s,d\rightarrow l,p}$ as:

$$F_{s,d\rightarrow l,p} = k_{dr}^{s,d\rightarrow l,p}\left(C_{s,d} - C_{s,d}^{0}\right) \quad \text{Eq. 93}$$

where $k_{dr}^{s,d\rightarrow l,p}$ is the driving force coefficient for Ln solute in the fuel to diffuse out of the fuel into Ln precipitates formed in the liquid metal solution. If dissolved Ln on the fuel surface is oversaturated, Ln will diffuse out of the fuel into the Ln precipitates in the liquid metal. On the other way around, if Ln in the fuel is under-saturated, Ln precipitates in the liquid metal will enter the fuel. If Ln concentration in the fuel is exactly at the solubility limit, the reaction will stop. The flux from Ln solute in the fuel to the Ln precipitates in the liquid metal solution is expressed as:

$$J_{s,d\rightarrow l,p} = \widetilde{D} F_{s,d\rightarrow l,p} \frac{C_{l,p}}{C_{Ln\_pure}}\left(1 - \frac{C_{s,p}}{C_{Ln\_pure}}\right) \quad \text{Eq. 94}$$

where $\widetilde{D}$ is the effective Ln diffusivity across the interface and is taken as the Ln solid-state diffusivity in the fuel, i.e. $\widetilde{D} = D_{solid}$. This reaction can only occur where the fuel surface contacts with the Ln precipitated from the liquid metal solution. Therefore, this reaction will be accelerated by more Ln precipitation formed in liquid metal at the interface, which is described by introducing the term: $\frac{C_{l,p}}{C_{Ln\_pure}}$. The barrier effects from the Ln precipitate from the fuel at the interface is considered through the term: $1 - \frac{C_{s,p}}{C_{Ln\_pure}}$.

*c) Dissolution of Ln precipitates from the fuel into liquid metal solution*

The dissolution of Ln precipitation in the fuel into the liquid metal filled pore will occur at the interface, which can be described by the driving force factor $F_{s,p\to l,d}$ as:

$$F_{s,p\to l,d} = k_{dr}^{s,p\to l,d} \cdot (C_{l,d}^{0} - C_{l,d}) \quad \text{Eq. 95}$$

where $k_{dr}^{s,p\to l,d}$ is the driving force coefficient for dissolution of Ln precipitates in the fuel to Ln solute in the liquid metal solution. If the Ln solute in the liquid metal solution is saturated, the dissolution will not occur. If dissolved Ln in the liquid metal is under-saturated, Ln precipitation in the fuel will dissolve into the liquid metal. However, if the Ln in liquid metal is oversaturated, dissolved Ln in liquid metal will enter the fuel and contribute to the fuel precipitation. The flux from Ln precipitates in the fuel to the Ln solute in the liquid metal solution is expressed as:

$$J_{s,p\to l,d} = \widetilde{D} F_{s,p\to l,d} \cdot \left(1 - \frac{C_{l,p}}{C_{Ln\_pure}}\right) \cdot \frac{C_{s,p}}{C_{Ln\_pure}} \quad \text{Eq. 96}$$

where $\widetilde{D}$ is the effective Ln diffusivity across the interface and is taken as the Ln solid-state diffusivity in the fuel, i.e. $\widetilde{D} = D_{solid}$. This reaction can only occur where the Ln precipitation in the fuel directly contacts with the liquid metal solution. Therefore, this reaction will be accelerated by more Ln precipitation formed from the fuel on the surface which is described by introducing the term: $\frac{C_{s,p}}{C_{Ln\_pure}}$, while reduced by more Ln precipitation formed from the liquid metal covering the surface which is described by the term: $1 - \frac{C_{l,p}}{C_{Ln\_pure}}$.

Diffusion kinetics

The diffusion kernel is applied to dissolved Ln in both the liquid metal solution and the fuel. The diffusion process is described by the Fick's law with the Soret term included [151]:

$$Q_{diffusion} = -\nabla \cdot \vec{J} \quad \text{Eq. 97}$$

$$\vec{J} = -D\left(\frac{\partial C}{\partial x} + \frac{Q^{*}C}{RT^{2}}\frac{\partial T}{\partial x}\right) \quad \text{Eq. 98}$$

where $R$ is the gas constant. Dissolved Ln in the solid fuel can diffuse with respective diffusivity and transport of heat $Q^{*}$ in different blocks. The temperature driving force

effect is represented by the Soret term $\frac{Q^*}{RT^2}\frac{\partial T}{\partial x}$.

### 8.2.3 Materials Properties

The established MOOSE model is applied to simulate X447 experiment conducted in the EBR-II [152]. The X447 experiment was designed to investigate the stress rupture properties of the cladding and the fuel-cladding chemical interactions in metallic fuels. The burnup rate is estimated from an achievement of 5% burnup within 288 effective full power days (EFPD) [152]. Composition of the fuel is listed below:

**Table 11 U-10wt%Zr fuel with enriched uranium (67% w/o U-235) [153]**

| | U-235 | U-238 | Zr |
|---|---|---|---|
| mole mass (g/mol) | 235 | 238 | 91.224 |
| mass fraction | 0.67*0.9 | 0.33*0.9 | 0.1 |
| mole fraction | 0.5226 | 0.2542 | 0.2233 |

The atomic number per unit volume of different materials in the simulation is calculated and is shown in Table 12:

**Table 12 Atomic density of materials in the simulation.**

| Material | U-10wtZr | $\gamma$-Ce | Cs (liquid) | Na (liquid) |
|---|---|---|---|---|
| theoretical density (g/cm$^3$) | 15.8 [152] | 8.85 [154] | 1.8291 [155] | 0.805 [156] |
| mole mass (g/mol) | 203.66 | 142.40 | 137 | 23 |
| atomic density (mol/m$^3$) | 7.76E+04 | 6.21E+04 | 1.34E+04 | 3.50E+04 |
| atomic density (atoms/μm$^3$) | 4.67E+10 | 3.74E+10 | 8.04E+09 | 2.11E+10 |

where the effective mole mass of U-10wt Zr is calculated from the element fraction in Table 1. The effective mole mass of Ce is weighted by the fission yields of two major Ce fission products Ce-141(5.795%) and Ce-144 (5.094%) [152]. The density (g/cm$^3$) of the mixture Na(50.23 at%)-Cs as mentioned in the previous chapter can be calculated by [157]:

$$\rho = 1.667 - 4.8 \times 10^{-4}(T - 373.16) \qquad \text{Eq. 99}$$

where $T$ is the temperature in unit of Kelvin. An average approximation of fission rate is obtained from X447 experiment in the EBR-II 5 at% burnup after 288 EFPD [152] as in Table 13.

**Table 13 Calculation of Ce generation rate. Heavy Metal density for U-10Zr is the density of uranium.**

| | |
|---|---|
| Heavy Metal density ($atoms/\mu m^3$) | 3.6288E+10 |
| Burnup fraction (mole fraction) | 0.05 |
| Time (s) | 24883200 |
| fission rate density ($atoms/\mu m^3/s$) | 72.9165 |
| Ce fission yield(141 and 144) | 0.1089 |
| Ce generation rate ($atoms/\mu m^3/s$) | 7.9399 |

The liquid-state diffusivity and solubility are obtained from DFT calculations on Ce in liquid Na and Cs separately. The Ce solubility in U-Zr fuel is related to the temperature and Zr concentration [158]. The solubility is estimated by the atomic fraction multiplied by the density of the fuel atoms, which is a reasonable assumption since the solubility is very low. Also the Ln solubility in the fuel should depend on the specific U-Zr phase, however, in the present report, the effects of the phase change are not considered. Ce diffusivity in U-22at%Zr has been reported in the previous study [158] and a fitting of Ce diffusivities at 1023K and 1123K to Arrhenius equation can be achieved. The experimental data for Soret heat of transport are currently lacking. The effective diffusion coefficient $\widetilde{D}$ is set to be $D_{s,d}$ indicating the solid-state diffusion dominates at the interface. The other unknown parameters are tested individually. A summary of the current parameter settings is shown in Table 14:

**Table 14 Parameters for the current pore-scale simulation.**

| Kinetics | Parameters | |
|---|---|---|
| Precipitation | $R \cdot C_{sink}$ ($\mu m^{-2}$) | 10 |
| | $k_{l,p}$ ($s^{-1}$) | 10 |
| | Ce solubility in U-Zr (mole fraction) | 0.003 (873K, 20at% Zr) |
| | Ce solubility in Na (mole fraction) | $\exp(-15.5763 - 0.2206/(T \cdot k_B))$ |
| | Ce solubility in Cs (mole fraction) | $\exp(-4.2240 - 0.6674/(T \cdot k_B))$ |
| Interface Reaction | $k_{dr}^{s,d\to l,d}$ ($\mu m^{-1}$) | $2 \times 10^{-5}$ |
| | $k_{dr}^{s,d\to l,p}$ ($\mu m^{-1}$) | $10^3$ |
| | $k_{dr}^{s,p\to l,d}$ ($\mu m^{-1}$) | $10^3$ |

| | | |
|---|---|---|
| Diffusion | Ce Diffusivity in liquid Na ($cm^2/s$) | $6.658 \times 10^{-4}\exp(-0.2226/(T \cdot k_B))$ |
| | Ce Diffusivity in liquid Cs ($cm^2/s$) | $1.56 \times 10^{-4}\exp(-0.144/(T \cdot k_B))$ |
| | Ce Solid-state Diffusivity in the fuel ($cm^2/s$) | $3.61 \times 10^{-8}\exp(-1.171/(T \cdot k_B))$ |
| | Solid Soret $Q^*$ (eV) | 1.0 |
| | Liquid Soret $Q^*$ (eV) | 1.0 |

The solubility is calculated in the unit of mole fraction. To convert it in the custom unit of $atoms/\mu m^3$ in the simulation, the atomic densities of different media from previous studies are used as listed in Table 12. Since the solubility is very low, Ce solubility in unit of $atoms/\mu m^3$ is approximated by the corresponding medium density multiplied by Ce solubility in unit of atomic fraction.

### 8.2.4 Results and Discussions

As shown in Figure 58, assuming pores are connected with the Na-filled gap, Ce is concentrated on the cold side of the gap due to the Soret effects in liquid Na. Therefore, Ce precipitation first forms on the cold side of the gap when Ce concentration is above the solubility. No Ln precipitation is observed in the pore since the Ln solubility in Cs is much higher than that in Na. Because the precipitation rate in the fuel is set to be large enough that Ln will precipitate out once surpassing the solubility limit, the concentration curve of dissolved Ln in the fuel almost overlaps with the solubility limit curve. Therefore, Ce migration along the temperature gradient from the left to the right is mainly caused by the Soret effects based on Eq. 98. In addition, Soret effects in the liquid metal are more dramatic than in the solid fuel due to a larger value of liquid-state diffusivity.

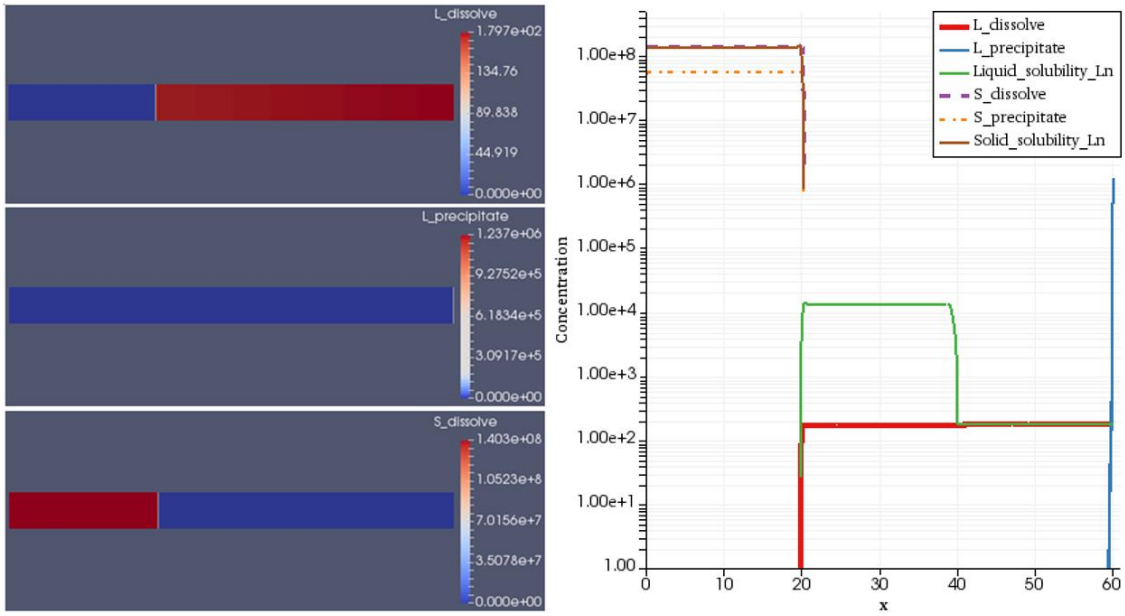


**Figure 58. Distribution of Ce concentration (atoms/μm$^3$) along 60μm at 5% burnup achieved by the simulation. Three blocks are included: fuel block on the left, liquid Cs filled pore in the middle and the liquid Na filled gap region on the right, each block with a length of 20μm. The Cs and Na in separate blocks are assumed to be not miscible currently. The temperature is decreasing with a gradient of 0.05K/μm from 855K on the left to 852K on the right. The source term is set to 7.9399 atoms/μm$^3$/s in the fuel block.**

## 8.2.5 Mesh Test


**Figure 59 Mesh settings in the calculation. Finer meshes are applied in three regions.**

The mesh settings are shown in Figure 59. Finer meshes are applied in the regions near the fuel/pore interface to reflect the interface reactions more accurately. Moreover, the Ce precipitation in the liquid metal is carefully accounted for by using finer mesh near the right side of the gap. Thereby, three regions with a length of 2μm in total are using fine mesh while the rest part which we denote as "Region 4" may use coarse mesh to save the simulation time. The lengths of the mesh regions are also tested and confirmed to be appropriate to accurately capture the Ce concentration. Testing of the different

mesh element sizes (μm) was shown in Table 15, where the average values of multiple Ln concentration in the corresponding blocks are compared. Item V is the mesh we are using. As can be seen, each element size in regions 1-4 are tested individually and the concentration changes are rather small. Moreover, Ce distribution for Mesh Items I-IV in Figure 60 are almost the same with Item V in Figure 58.

**Table 15 Mesh testing with different element size (μm) in distinct regions and the average values of Ce concentration in the corresponding blocks, e.g. $C_{l,p}^{ave\_liquid}$ is the average Ce precipitation concentration in the liquid solution including the pore and gap blocks.**

| Item | Reg 1 | Reg 2 | Reg 3 | Reg 4 | $C_{l,p}^{ave\_liquid}$ | $C_{l,d}^{ave\_liquid}$ | $C_{s,p}^{ave\_fuel}$ | $C_{s,d}^{ave\_fuel}$ |
|---|---|---|---|---|---|---|---|---|
| I | 0.5 | 0.5 | 0.1 | 1 | 1187 | 177 | 57269276 | 140298117 |
| II | 0.5 | 0.5 | 0.2 | 0.5 | 1189 | 177 | 57269271 | 140298117 |
| III | 0.25 | 0.5 | 0.2 | 1 | 1190 | 177 | 57269270 | 140298117 |
| IV | 0.5 | 0.25 | 0.2 | 1 | 1190 | 177 | 57269270 | 140298117 |
| V | 0.5 | 0.5 | 0.2 | 1 | 1189 | 177 | 57269271 | 140298117 |

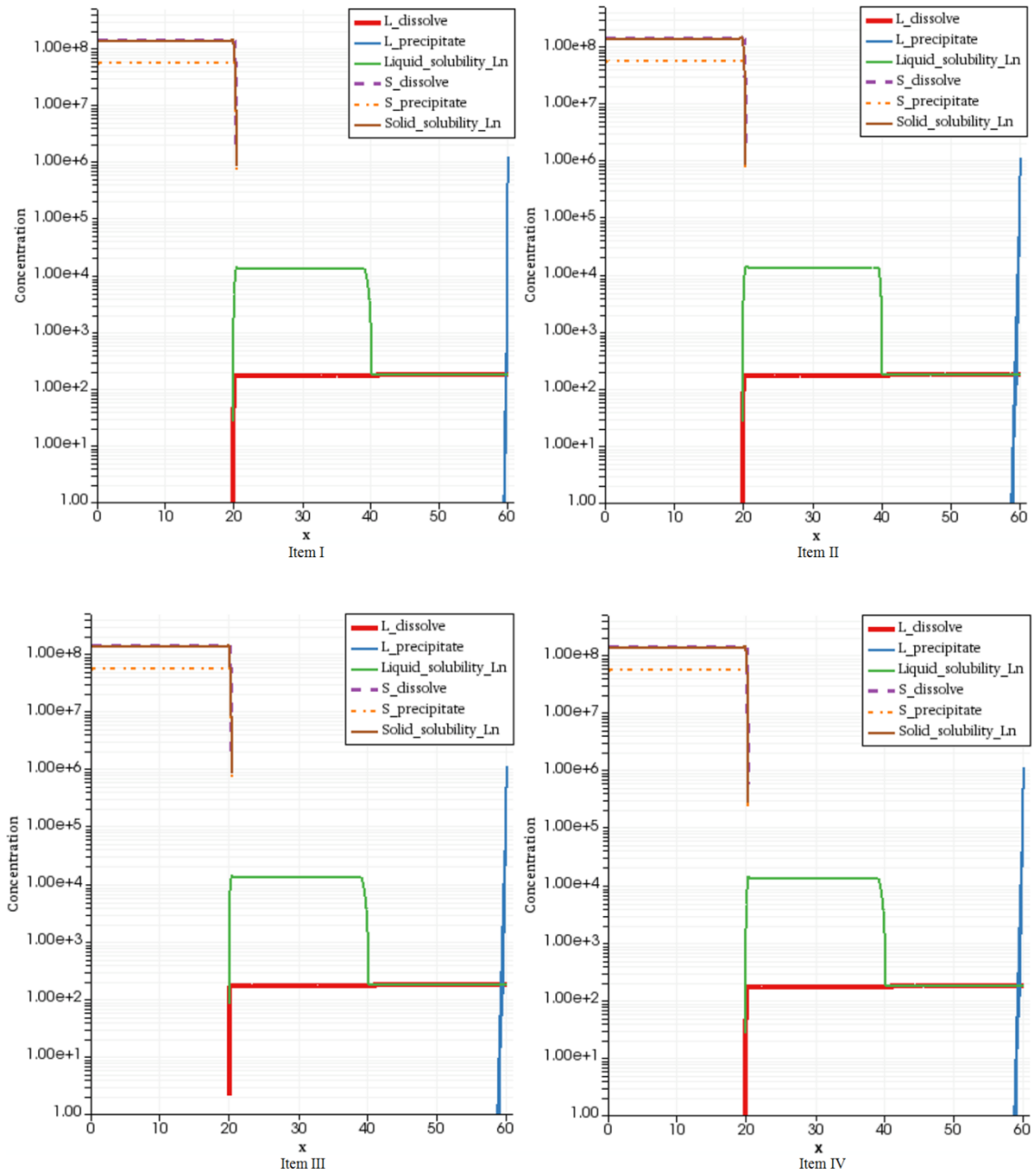


**Figure 60 Ce concentration distribution under different mesh settings (Mesh Item I-IV).**

## 8.2.6 Mass Conservation Verification

According to the mass conservation law, the Ce of different forms should sum up to the total amount of Ce produced in the fuel.

**Table 16 Integral amount of Ln concentration at 5% burnup from the simulation.**

| | |
|---|---|
| Time(s) | 24883200 |
| $C_{l,d}^{Integral}$ (atoms/μm) | 35367.65 |

| | |
|---|---|
| $C_{l,p}^{Integral}$ (atoms/μm) | 238370.50 |
| $C_{s,d}^{Integral}$ (atoms/μm) | 14029811679.12 |
| $C_{s,p}^{Integral}$ ((atoms/μm)) | 5726926550.73 |
| Total_Ln (atoms/μm) | 19757011968 |
| Ln Source (atoms/μm$^3$/s) | 7.9399 |
| Total Source Area (μm$^2$) | 100.00 |
| Total Ln generated (atoms/μm) | 19757011970 |

As shown in Table 16, the total generated Ce is calculated based on the given generation rate, the fuel block area and the simulation time. All the other results are directly from the output of the simulation. The difference between the generated Ce in the fuel equals and total amount of Ce distributed along all the blocks are negligible, which verifies the mass conservation.

### 8.2.7 Parameters Testing

The simulated Ce migration process depends on the parameters as shown in Table 14. The unknown parameters are tested to investigate their individual influence on the model. While one parameter is changed, all the others keep fixed as in Table 14. However, since the pore is connected to the gap in the current case and the Ce precipitates tend to form on the right side of the gap and cannot contact with the fuel block, the parameter $k_{dr}^{s,d\rightarrow l,p}$ should not make any difference and its corresponding testing is put in the isolated pore case as presented in section 1.4. The testing of all the other parameters is as follows:

a) $R \cdot C_{sink}$ for precipitation in the fuel

With an increasing $\boldsymbol{R \cdot C_{sink}}$ in the fuel, the Ce will precipitate in the fuel faster and less oversaturated dissolved Ce in the fuel will be observed. Comparing (a) with (b) in Figure 61 shows that a small value of $\boldsymbol{R \cdot C_{sink}}$ yields the oversaturated $\boldsymbol{C_{s,d}}$ since the precipitation is not fast enough. The model is not sensitive to this parameter as long as its value is large enough as observed from the very similar profile in (b) and (c).

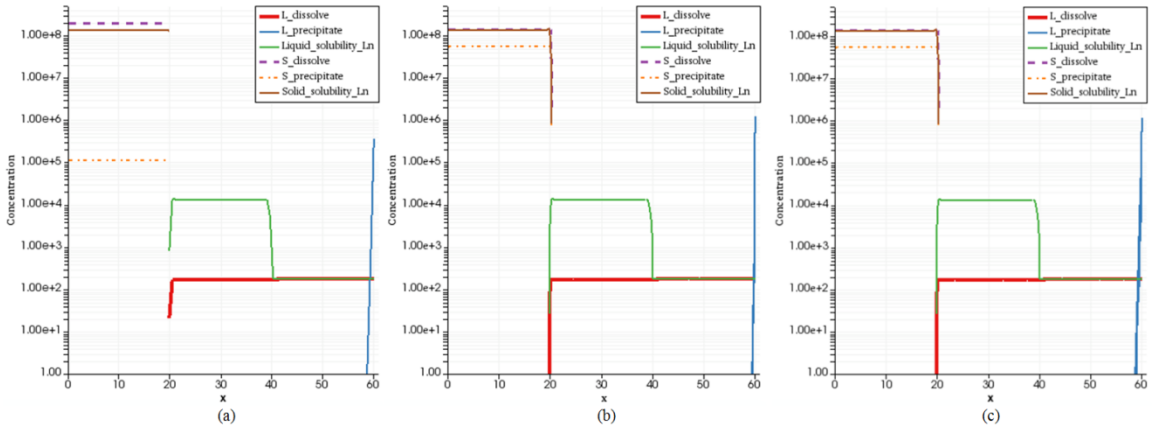


**Figure 61 Ce distribution at 5% burnup simulation with values of $R \cdot C_{sink}$(μm$^{-2}$) in the fuel from left to the right: $10^{-4}$, 10, $10^2$.**

b) $k_{l,p}$ for precipitation in the liquid metal

With an increasing value of $k_{l,p}$ the Ce will precipitate in the gap faster. A comparison between the (a) and (b) shows that more precipitation forms on the right side of the gap. However, no dramatic changes of Ce precipitation in the gap can be observed from the (b) and (c), which indicates that the model is not sensitive to $k_{l,p}$ as long as its value becomes large enough.

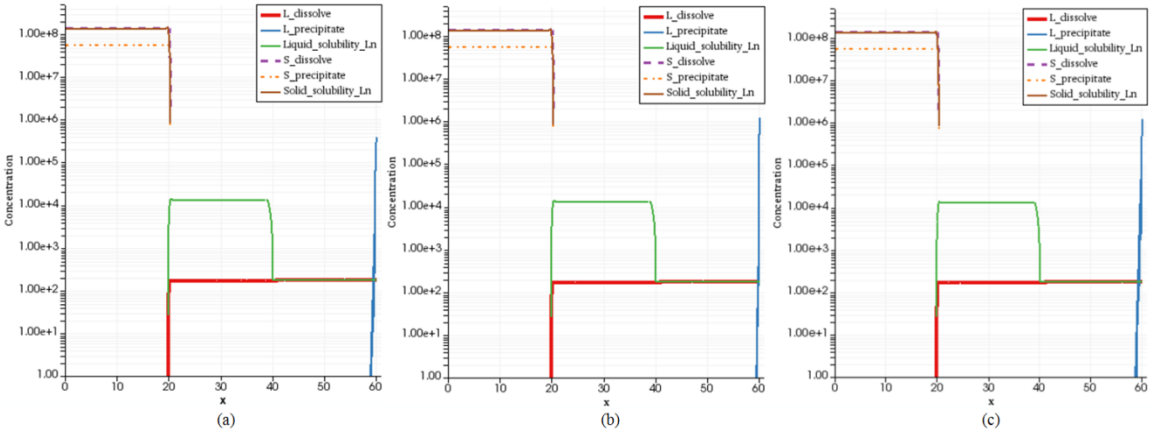


**Figure 62 Ce distribution at 5% burnup simulation with values of $k_{l,p}$(s$^{-1}$) from left to the right: 1.0, 10, $10^2$.**

c) Transport heat of solid Soret effects $Q^*_{solid}$

As $Q^*_{solid}$ is increasing, dissolved Ce in the fuel will migrate down the temperature gradient more dramatically. This is not obviously reflected from the simulation due to

the small value of the Soret term and also the small solid-state diffusivity. However, a value of 10eV as in (c) yields a larger value of $C_{s,p}$ on the right side of the fuel block. This is because more dissolved Ce in the fuel is pushed down the temperature gradient by a larger solid Soret effect and form more precipitation on the right side correspondingly.

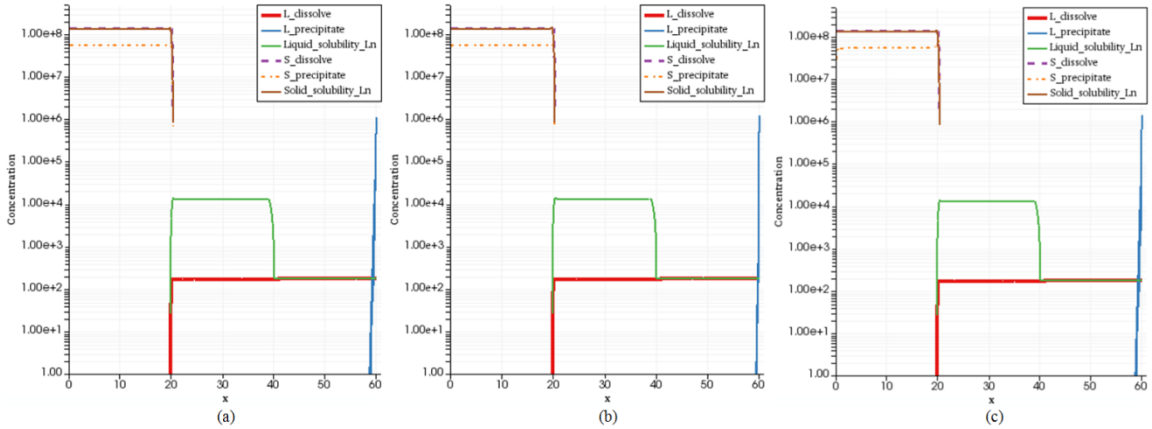


**Figure 63 Ce distribution at 5% burnup simulation with $Q^*_{solid}$ (eV) from left to the right: $10^{-1}$, 1.0, 10.**

d) Transport heat of liquid Soret effects $Q^*_{liquid}$

With an increasing $Q^*_{liquid}$, more dissolved Ce in both the pore and the gap will transport down the temperature gradient leading to more Ce precipitation formed in the gap as shown in comparison between (a) and (b). No dramatic changes of Ce precipitation in the gap have been observed from (b) to (c) since the value of this parameter is already too large to show sensitivity. However, a more dramatic increasing trend of $C_{l,d}$ down the temperature gradient is presented in (c) due to the larger value of liquid Soret effect.

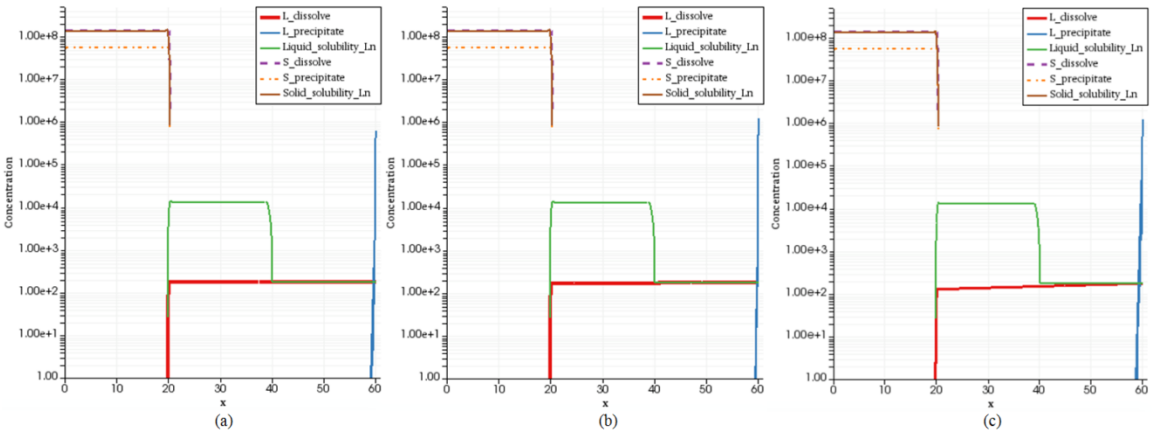


**Figure 64 Ce distribution at 5% burnup simulation with $Q^*_{liquid}$ (eV) from left to the right: 0.1, 1.0, 10.**

e) Driving force coefficient $k_{dr}^{s,d\rightarrow l,d}$ at the fuel/pore interface

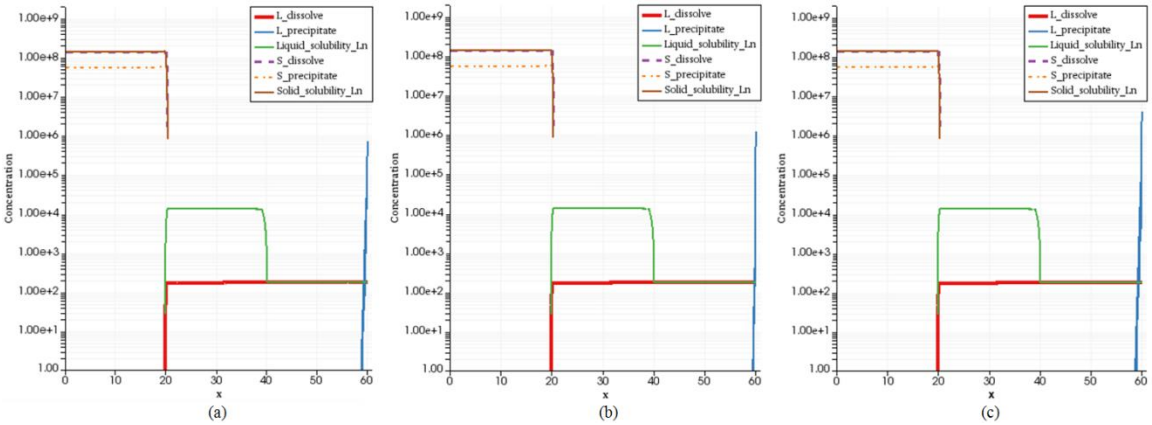


**Figure 65 Ce distribution at 5% burnup simulation with $k_{dr}^{s,d\rightarrow l,d}$(μm$^{-1}$) from left to the right: $2\times10^{-6}$, $2\times10^{-5}$, $2\times10^{-4}$.**

As $k_{dr}^{s,d\rightarrow l,d}$ increases, the reaction between dissolved Ce in the pore and the fuel becomes faster with more Ce solute in the fuel converted into Ce solute the liquid metal solution. As a result, more Ce precipitates form on the right side of the gap.

f) Driving force coefficient $k_{dr}^{s,p\rightarrow l,d}$ at the fuel/pore interface

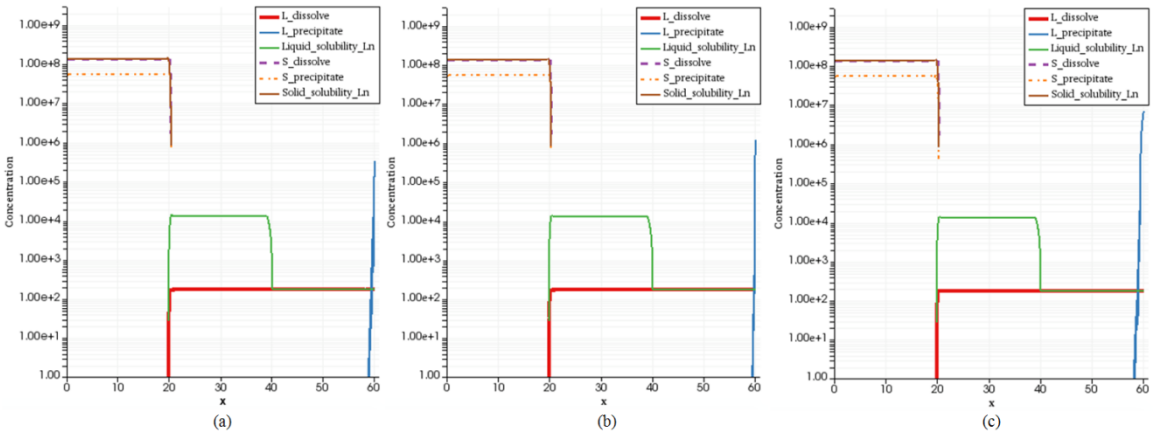


**Figure 66 Ce distribution at 5% burnup simulation with $k_{dr}^{s,p\rightarrow l,d}$ from left to the right: 10, $10^3$, $10^5$.**

With an increasing $k_{dr}^{s,p\rightarrow l,d}$, the Ce precipitates on the fuel side of the interface will dissolve into liquid-metal filled pore faster resulting in more Ce precipitation forms on the right side of the gap.

## 8.3 Ln Transport Model with a Transition Area Filled with Cs-Na Mixture

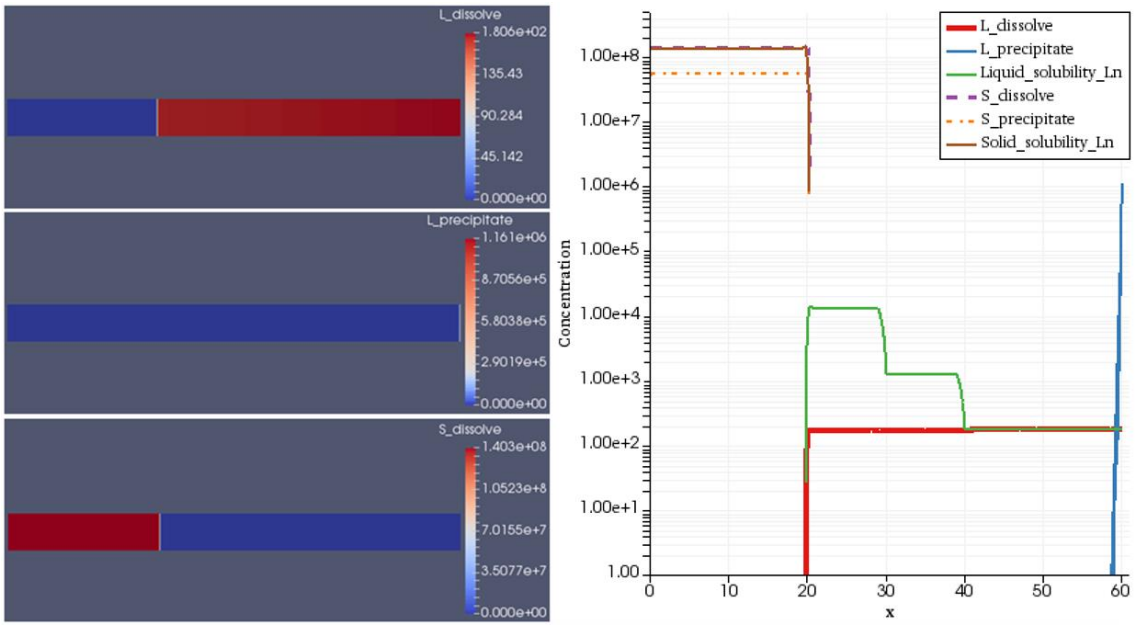


**Figure 67 Distribution of Ce concentration (atoms/μm$^3$) along 60 μm at 5% burnup achieved by the simulation. The liquid metal filled region is constituted by:**

**10 μm of Cs-filled pore, 10 μm of Na(50.23 at.%)-Cs filled pore and 20 μm of Na-filled gap. Three Ce solubility in liquid metal are used correspondingly.**

Liquid Na and Cs can mix with each other. To extend from the original assumption that Na and Cs exits in separate regions, we introduce a transition region filled with Na-Cs mixture to capture the possible influence from different compositions of liquid metal solution. The transition region is still a simplified model as a gradual changing of solubility from the pore to the gap can be expected in reality. However, a comparison between Figure 58 and Figure 67 shows that the different solubility introduced in the transition region appears to have no impacts on the Ln distribution profile since all the Ln precipitation in liquid metal concentrates on the cold side of the gap.

## 8.4 Ln Transport in an Isolated Cs Filled Tubular Pore

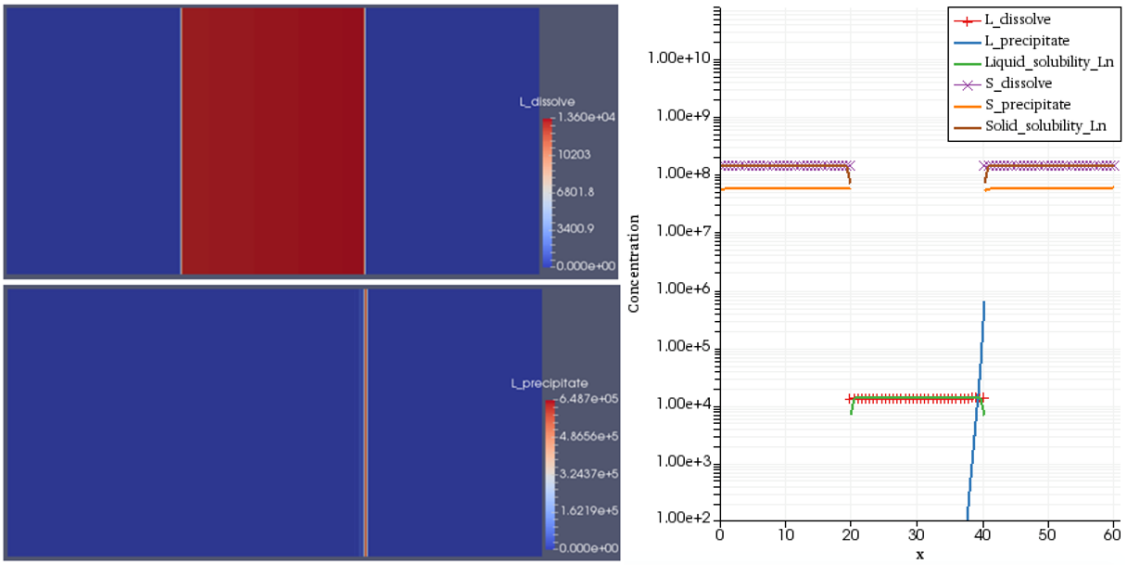


**Figure 68 Distribution of Ce concentration (atoms/μm$^3$) along 60 μm at 5% burnup achieved by the simulation. Three blocks are included: liquid Cs filled pore in the middle with two fuel blocks on both sides. The temperature is decreasing with a gradient of 0.05K/μm from 855K on the left to 852K on the right. The source term is set to 7.9399 atoms/μm$^3$/s in the fuel blocks.**

In this section, the parameters in the calculation are the same as listed in Table 14 except $k_{dr}^{s,p\rightarrow l,d}$ is set to be $10^5$ μm$^{-1}$ for a more dramatic Ln precipitation in liquid metal solution within a simulation time of 5% burnup. As shown in Figure 68, Ce in the Cs filled pore is more concentrated on the cold side of the pore due to the Soret effects in liquid Cs. Therefore, Ce precipitation first forms on the cold side of the pore when Ce concentration is above the solubility. The right fuel block has almost the same Ce

concentration as that in the left fuel block, which indicates that the isolated Cs-filled pore cannot contribute to the migration of Ce. This is due to the fact that Ce in the right fuel block is always oversaturated upon the formation of Ln precipitation in the liquid metal and a Ce flux from the right fuel block to the pore can be expected based on Eq. 93. Therefore, Cs-filled pore turns out to be a sink for Ce.

As the Ln precipitation can form on the surface of the right fuel block, the driving force coefficient $k_{dr}^{s,d\to l,p}$ may influence Ln concentration distribution, which is tested as follows:

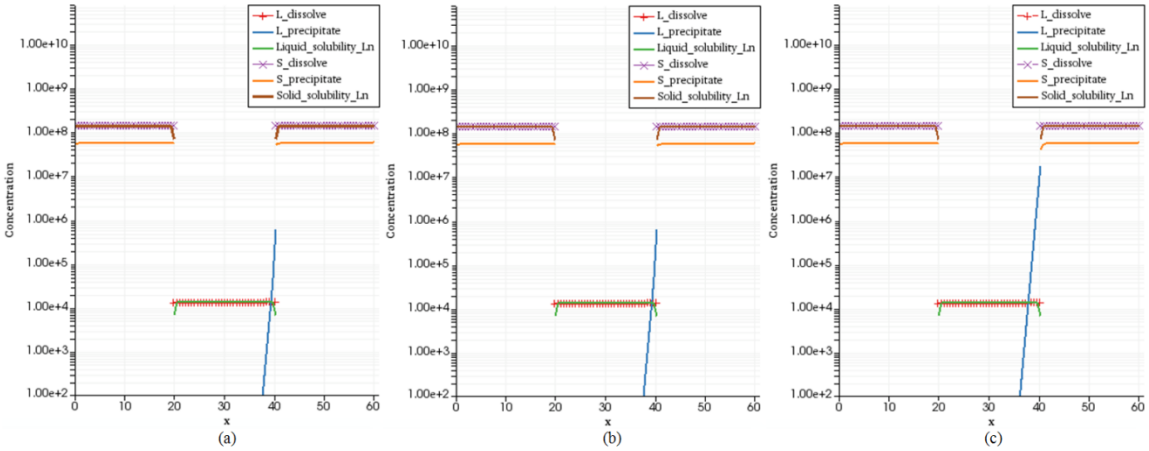


**Figure 69 Ce distribution at 5% burnup simulation with $k_{dr}^{s,d\to l,p}$(μm$^{-1}$) from left to the right: 10, $10^3$, $10^5$.**

Under the current circumstances, the Ce from the right fuel block will enter the Cs-filled pore to contribute to the Ln precipitation in liquid solution. An increasing value of $k_{dr}^{s,d\to l,p}$ results in a larger rate of inter-diffusion between Ce precipitates in the liquid metal solution and the Ce solute in fuel. Therefore, a dramatic increase of Ce precipitation concentration on the right side of Cs-filled pore has been observed from (b) to (c). However, a smaller value of such parameter shows less influence as shown from comparison between (a) and (b), indicating that the model is not sensitive to this parameter when it is too small.

## 8.5 Ln Transport in a Fuel Square with a Cs Filled Pore Connected to a Na Filled Gap

The estblished model is extend to cases with a 2-D single square pore. The same parameters are used as in Table 14. Calculations are performed for two different

temperature profiles:

a. 1-D temperature profile

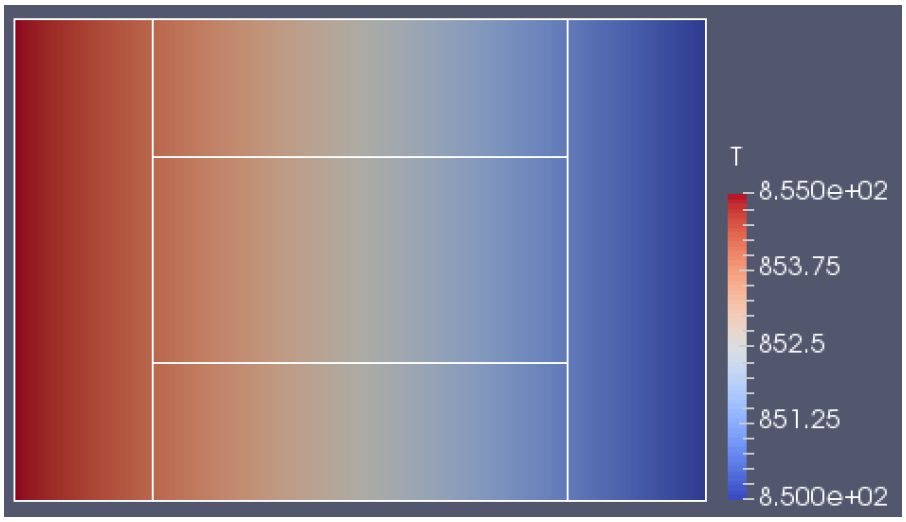


**Figure 70. Schematics of different regions in a $100\mu m \times 70\mu m$ square and the temperature profile with a gradient of 0.05K/μm along the x-axis. The highest temperature is set to 855 K. The gap block is on the right and the pore block in the middle, with the rest as fuel blocks.**

Ce diffuses in the fuel square with a single liquid Cs filled pore in the center and a Na-filled gap on the right with a 1D temperature profile as shown in Figure 70. The concentrated can be seen on the cold side of the gap as precipitates in Figure 71.

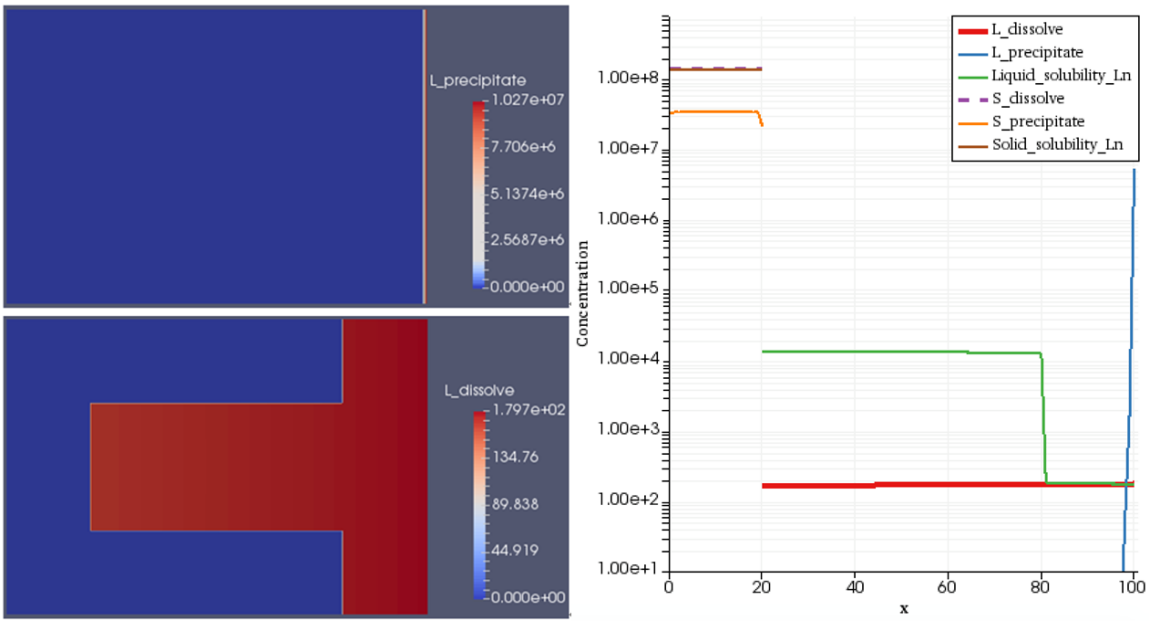


**Figure 71. Ce concentration distribution along x-direction centerline after reaching 5% burnup with a 1D temperature profile as indicated in Figure 70. The Ce generation rate is set to 7.9399 atoms/$\mu m^3$/s in the fuel blocks.**

b. 2-D temperature profile

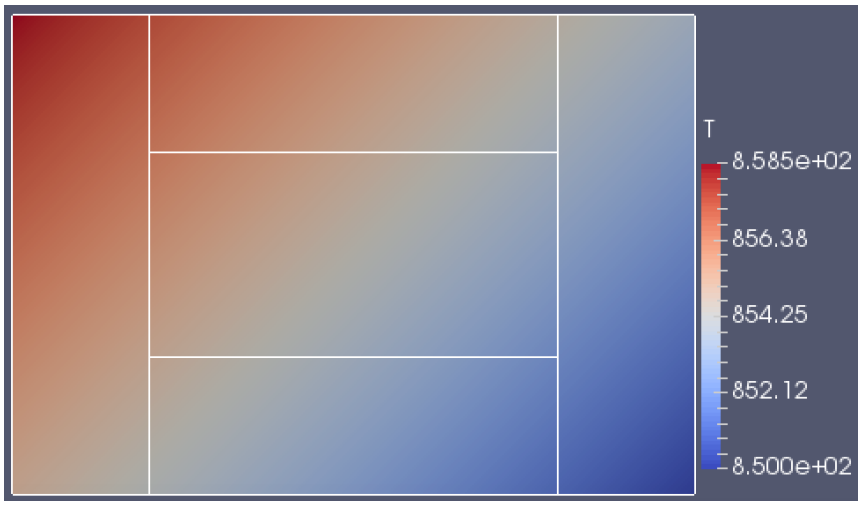


**Figure 72 Schematics of different regions in a $100\mu m \times 70\mu m$ square and a 2-D temperature profile with a gradient of 0.05K/μm along the both x-axis and y-axis. The lowest temperature is set to 850 K at the bottom right corner. The gap block is on the right and the pore block in the middle, with the rest as fuel blocks**.

Ce diffuses in the fuel square with a 2-D temperature profile in Figure 72. As expected, the concentrated Ce precipitates form at cold locations in the gap, which is on the bottom right corner (see Figure 73).


**Figure 73 Distribution of Ce precipitates concentration in liquid metal solution with a 2-D temperature profile as indicated in Figure 72. The Ce generation rate is set to 7.9399 atoms/$\mu m^3$/s in the fuel blocks.**

## 8.6 Ln Transport Model Through Multiple Pores

The estblished model is extend to cases with 2-D multiple circle pores. The same

parameters are used as in Table 14 except $k_{dr}^{s,p\to l,d}$ is set to be $10^5$ μm$^{-1}$ for more dramatic Ln precipitation in liquid metal solution in this whole section. Calculations are performed for two different distributions of pores as follows:

a. Multi-pore model $40\mu m \times 40\mu m$

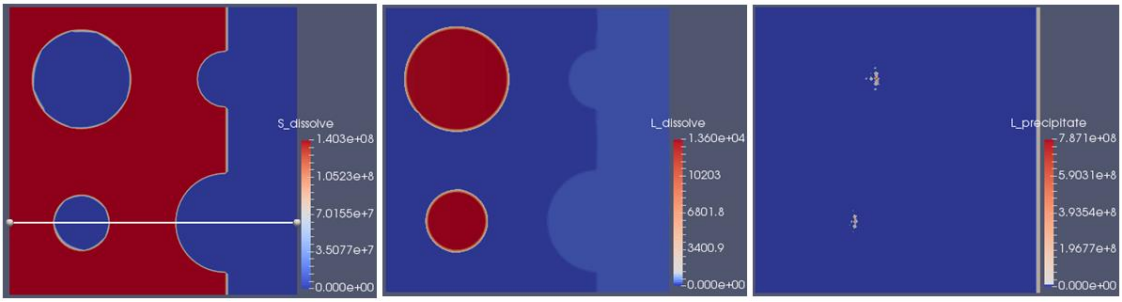


**Figure 74 Distribution of Ce concentration with a 1D temperature profile after reaching 10% burnup using a 1D temperature profile with a gradient of 0.05K/μm decreasing along the x-axis and the highest temperature 855K. The Ce generation rate is set to 7.9399 atoms/μm$^3$/s in the fuel. Two isolated Cs-filled circle bubbles of different sizes are included inside the fuel block and two semi-circle Cs-filled circle bubbles are connected to the Na-filled gap.**

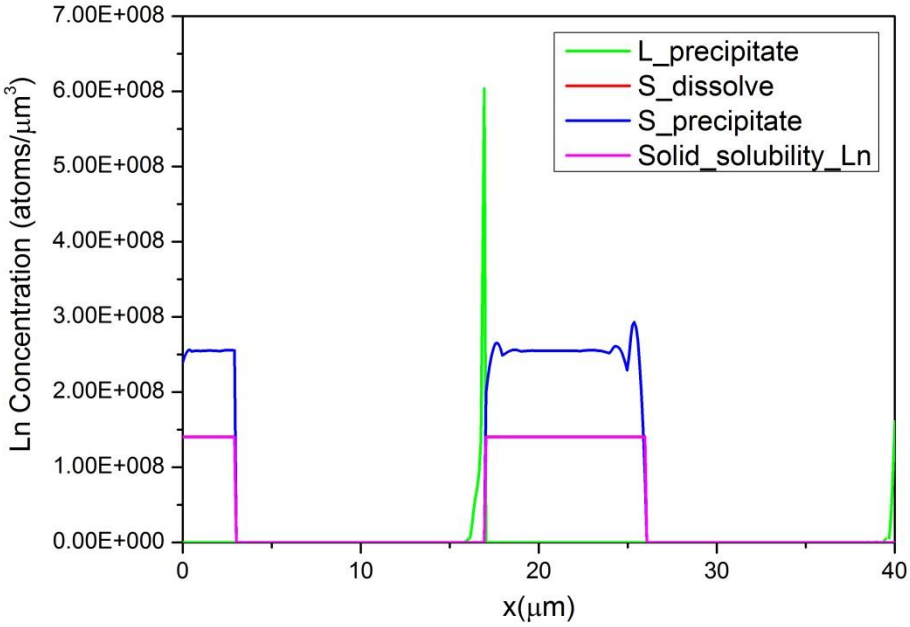


**Figure 75 Ce concentration distribution along a horizontal line as indicated in Figure 74. There is an overlap between curves indicating Ln solute concentration and the Ln solubility in the fuel due to the fast Ln precipitation process in the solid**

**fuel. The dissolved Ln in Na or Cs and the corresponding Ln solubility are not shown due to their much smaller values.**

As shown in Figure 74, the amount of dissolved Ln in the Cs-filled pores is much larger than that of Na-filled gap due to the larger Ln solubility in liquid Cs. Ln precipitates form both on the cold side of the isolated Cs-filled pores and also on the cold side of the Na-filled gap.

b. Multi-pore model $60\mu m \times 20\mu m$

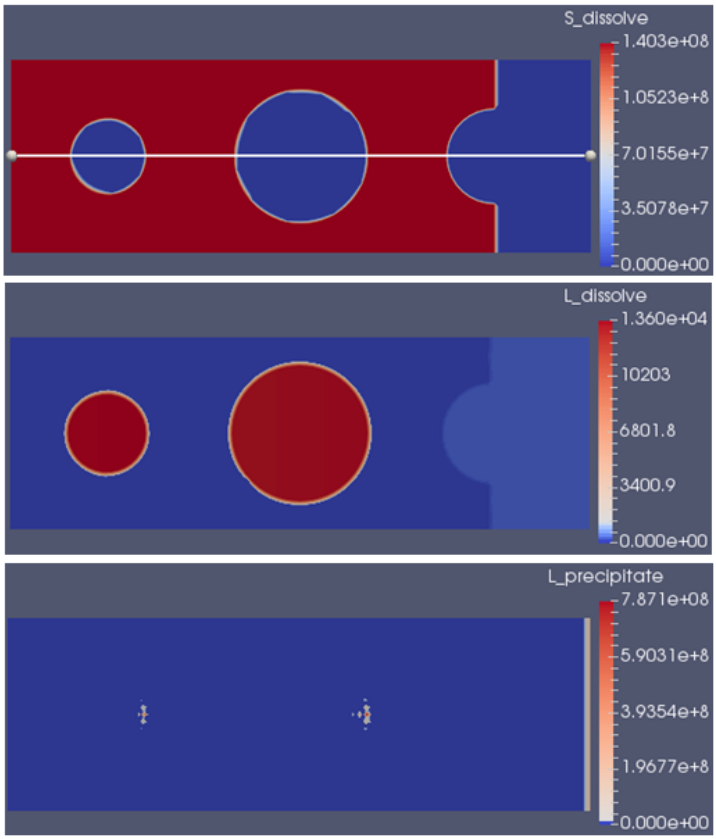


**Figure 76 Ce concentration distribution with a 1D temperature profile after reaching 10% burnup using a 1D temperature profile with a gradient of 0.05K/μm decreasing along the x-axis and the highest temperature 855K. The Ce generation rate is set to 7.9399 atoms/μm$^3$/s in the fuel blocks. Two isolated Cs-filled circle bubbles of different sizes are included inside the fuel block and one semi-circle Cs-filled circle bubbles are connected to the Na-filled gap.**

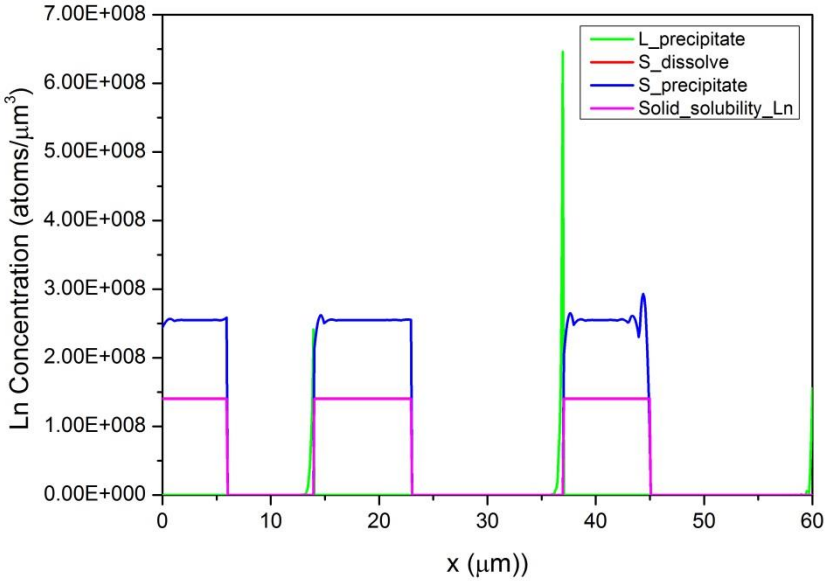


**Figure 77 Ce concentration distribution along a horizontal line as shown in Figure 76.**

As shown in Figure 76, Ce precipitates form in the Cs-filled pores and Na-filled gap. The larger Cs-filled pore has more Ce precipitation formed on the cold side than the smaller one. That may be because the larger pore locates where the temperature is lower and a larger size of pore can contain more Ln solute for the further precipitation process.

## 8.7 Conclusion

Modelling of Ln transport behaviors in pore scale has been achieved by using MOOSE/BISON. Ln migration phenomena have been simulated through a series of models: Ln transport in a 1D-tubular Cs-filled pore connected to Na-filled gap, Ln transport in a single 1-D isolated Cs-filled pore, Ln transport in a single Cs-filled pore connected to Na-filled gap and Ln transport in multiple circle pores. The simulation is performed focusing on Ce and using the corresponding materials properties. Materials properties such as Ln solubilities and diffusivities are from the DFT and Ab-initio MD calculations. Besides, there are seven unknown parameters in total which are tested individually to account for their sensitivity. It is found Ln migration is mainly driven by the Soret effects down the temperature gradient, especially in the liquid metal solution. Ln precipitation in liquid metal solution preferably initiates where the solubility is low either due to the composition or the temperature. Therefore, once the pore is connected to the Na gap where the solubility is much lower than that in the Cs-filled pore, the precipitates always form on the cold side of the gap. In the case of

isolated Cs-filled pores, however, Ln precipitates form on the surface of the fuel resulting in an Ln-fuel diffusion couple. With the current parameter settings, Cs-filled pores act as an Ln sink where Ln will enter from the fuel to contribute to the Ln precipitation in liquid metal solution. Such sink is unfavorable for the Ln transport from the fuel center to the fuel surface. Therefore, the Ln migration through the porous fuel can only be accelerated when pores are interconnected and finally connected to the Na-filled gap.

# 9. MOOSE/BISON Modeling of Ln Transport in Porous Medium

## 9.1 Mathematic Model

To achieve a macroscopic description of Ln transport behaviors in the metal fuel, the previously established pore-scale model of Ln transport behavior is required to be transferred to a continuum description.

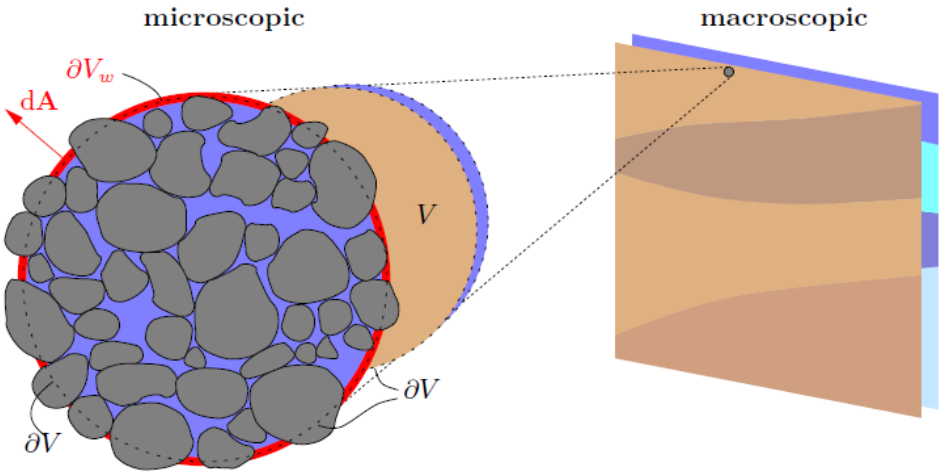


**Figure 78. [159] Schematics of a porous medium from a pore-scale (microscopic) to a continuum description (macroscopic).**

A schematic of conversion from pore-scale to a macroscopic porous model is shown in Figure 78. Each point of the pores belongs to one of the phases, either to a specific phase. By introducing the indicator function [159]:

$$\chi_i(x) = \begin{cases} 1, x \in phase\ \ i \\ 0, x \notin phase\ \ i \end{cases} \qquad \text{Eq. 100}$$

The average of some microscopic property $\alpha^{\mu}$ of phase $i$, i.e. the macroscopic value can be obtained by [159]:

$$\alpha^m(x) \coloneqq \langle \alpha^{\mu} \chi_i \rangle(x) \coloneqq \int_{\Omega} \alpha^{\mu}(x + x')\chi_i(x + x')\kappa(x')dx' \qquad \text{Eq. 101}$$

where $\kappa(x)$ is some convenient weight function within the support $\Omega$. $\kappa(x) \geq 0$ and $\int_{\Omega} \kappa(x)dx = 1$.

In order to migrate from a description of pore-scale to a continuum description of the porous medium as a whole, we first invoke an appropriate representative element volume (REV) in which some microscopic quantity becomes approximately constant when averaged with a weight function of characteristic extent $l$. Here we use a cube of side length $l$ as averaging volume with a weight function that is constant with the cube. The relevant state variables will be defined as state variables. The macroscopic solute flux will be obtained from the mass conservation equation [159]:

$$\frac{\partial(\theta C_L)}{\partial t} - \nabla \cdot \left[\theta \langle D^{\mu} \nabla C_L^{\mu} \rangle_L\right] = 0 \qquad \text{Eq. 102}$$

where $\theta$ is the liquid phase content, $C_L \coloneqq \langle C_L^{\mu} \rangle_L$ is the average concentration of solute in the liquid phase of volume $V$. $D^{\mu}$ is the molecular diffusion coefficient. $\langle D^{\mu} \nabla C_L^{\mu} \rangle_L$ includes the microscopic variation of the molecular diffusion coefficient and of the concentration gradient, which depends on the geometry of the liquid phase at the pore-scale. Under the assumption of liquid metal saturation in pores, we simplify this by taking their spatial average as a constant which will be absorbed into an effective value $D_{eff}$ of molecular diffusion coefficient for the porous medium. Eq. 102 can be rewritten as [160]:

$$\frac{\partial C}{\partial t} - \nabla \cdot \left[D_{eff} \nabla C\right] = 0 \qquad \text{Eq. 103}$$

where $C$ is the homogenized solute concentration throughout the material [160]. The transportation of a solute spreading in a porous medium is limited compared with that in a pure static bulk liquid. The effective diffusivity in porous media is macroscopic and can be estimated as [161]:

$$D_{eff} = \frac{D^{\mu} \Phi}{1.5 - \Phi/2} \qquad \text{Eq. 104}$$

where $\Phi$ is the liquid volume fraction available for the transport, which equals porosity under the assumption that the pores are filled with liquid metal. To handle effects of temperature on Ln migration in the porous medium, Soret term will be introduced as:

$$\frac{\partial C}{\partial t} - \nabla \cdot \left[D_{eff} (\nabla C + \frac{Q^* C}{RT^2} \nabla T)\right] = 0 \qquad \text{Eq. 105}$$

## 9.2 Ln Kinetics in Porous Media Adjacent to the Na-Filled Gap

Besides the assumptions listed in section 8.2, extra assumptions are introduced for porous media:

1. All the pores are interconnected and finally connected to the Na-filled gap.
2. All the interconnected pores are filled with liquid metal and are all available for Ln transportation.
3. The effects of porosity on the interface reaction at the boundary between porous media and the gap are negligible.
4. The correlation between the effective diffusivity and the molecular diffusivity is a function of the porosity only.

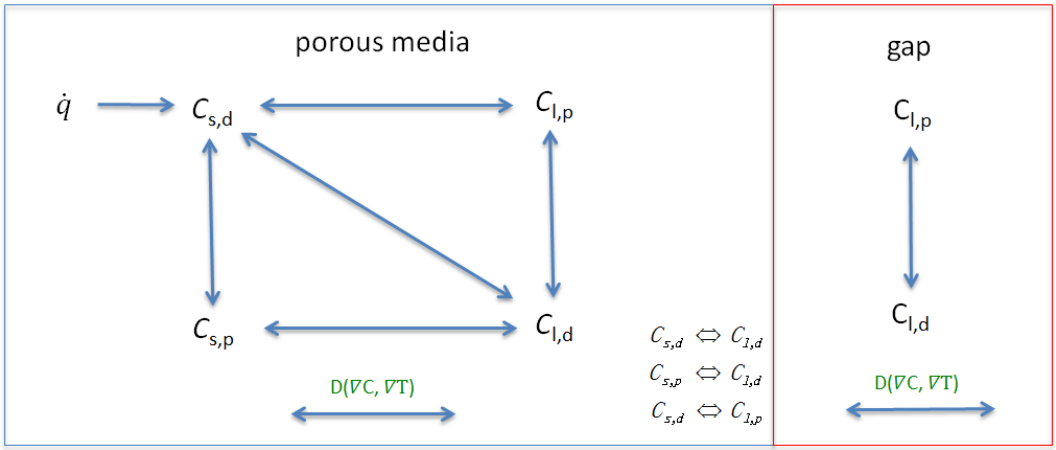


**Figure 79. Schematics of Ln diffusion and reactions in porous media adjacent to the Na-filled gap with the temperature decreasing from left to the right.**

As shown in Figure 79, porous media are consisted of U-Zr fuel and interconnected Cs-filled pores. Four homogenized Ln concentration variables similar to those introduced in the pore-scale case are defined in the porous media block [160]: $C_{s,p}$, $C_{s,d}$, $C_{l,d}$ and $C_{l,p}$, of which $C_{l,d}$ and $C_{l,p}$ are also defined in the gap block. The Ln transport behaviors in the gap are described by the same kinetics as in the pore-scale model. The reactions which occur at the interface between porous media and the Na-filled gap are the same with those in pore-scale model as presented in section 1.2.3.

In the porous media block, however, some properties of porous media, especially porosity, should be included in kinetics. The Ln diffusion kinetics in liquid metal solution is described in Eq. 105 with porosity included while the Ln diffusion process in solid fuel is based on Eq. 98. The average Ln solid-state precipitation rate and the average Ln precipitation in liquid metal part of the porous media should be correlated with the porosity. To describe the reactions at the fuel-pore interface inside the porous

media, average volume reaction rates between different Ln concentration variables should be introduced.

## 9.3 Porous Media Model Implementation in MOOSE/BISON

Four variables for Ln concentration will be defined in porous media block: dissolved Ln concentration in solid $C_{s,d}$ and in liquid $C_{l,d}$; precipitated Ln concentration in solid $C_{s,p}$ and in liquid $C_{l,p}$. Compared with the pore-scale model, three additional kernels are included as represented by the corresponding reaction rate terms: $Q_{porous}^{s,d\to l,d}$, $Q_{porous}^{s,p\to l,d}$ and $Q_{porous}^{s,d\to l,p}$ in Figure 80. Also the original kernels for diffusion and precipitation processes in pore-scale model are modified to capture the porous media properties.

Porous Media

$$\frac{\partial C_{s,d}}{\partial t} = Q_{diffusion} - Q_{porous}^{s,p} + \dot{q} - Q_{porous}^{s,d\to l,p} - Q_{porous}^{s,d\to l,d}$$

$$\frac{\partial C_{s,p}}{\partial t} = Q_{porous}^{s,p} - Q_{porous}^{s,p\to l,d}$$

$$\frac{\partial C_{l,d}}{\partial t} = Q_{diffusion} - Q_{porous}^{l,p} + Q_{porous}^{s,d\to l,d} + Q_{porous}^{s,p\to l,d}$$

$$\frac{\partial C_{l,p}}{\partial t} = Q_{porous}^{l,p} + Q_{porous}^{s,d\to l,p}$$

**Figure 80. Applied kernels in MOOSE for Ln transport in porous media.**

On basis of the pore-scale model, the average Ln solid-state precipitation rate in the porous media is correlated with the porosity as:

$$Q_{porous}^{s,p} = \begin{cases} 4\pi R C_{sink} D_{s,d}\left(C_{s,d} - C_{s,d}^{0}\right)\cdot(1-\Phi) & \left(C_{s,p} > C_{s,d}^{0}\right) \\ 4\pi R C_{sink} D_{s,d}\left(C_{s,d} - C_{s,d}^{0}\right)\dfrac{C_{s,p}}{C_{Ln\_pure}}\cdot(1-\Phi) & \left(C_{s,d} \le C_{s,d}^{0}\right) \end{cases} \quad \text{Eq. 106}$$

Since this solid-state precipitation only occurs in the solid fuel, a larger porosity will yield smaller precipitation rates. Similarly, the Ln precipitation rate in the liquid metal solution can be described by:

$$Q_{porous}^{l,p} = \begin{cases} k_{l,p} \cdot (C_{l,d} - C_{l,d}^0) \cdot \Phi & (C_{l,d} > C_{l,d}^0\ ) \\ k_{l,p} \cdot (C_{l,d} - C_{l,d}^0) \dfrac{C_{l,p}}{C_{Ln\_pure}} \cdot \Phi & (C_{l,d} \le C_{l,d}^0\ ) \end{cases} \quad \text{Eq. 107}$$

Additional volume average reactions with the physical meaning similar to Eq. 92, Eq. 94 and Eq. 96 have been included as reaction kernels inside the porous media block to approximate the corresponding reactions which can occur at the fuel/pore interface inside the porous media:

$$Q_{porous}^{s,d\to l,d} = \Phi \cdot k_{porous}^{s,d\to l,d} C_{s,d}^0 \left(\frac{C_{s,d}}{C_{s,d}^0} - \frac{C_{l,d}}{C_{l,d}^0}\right)\left(1 - \frac{C_{l,p}}{C_{Ln\_pure}}\right)\left(1 - \frac{C_{s,p}}{C_{Ln\_pure}}\right) \quad \text{Eq. 108}$$

$$Q_{porous}^{s,d\to l,p} = \Phi \cdot k_{porous}^{s,d\to l,p} (C_{s,d} - C_{s,d}^0) \frac{C_{l,p}}{C_{Ln\_pure}}\left(1 - \frac{C_{s,p}}{C_{Ln\_pure}}\right) \quad \text{Eq. 109}$$

$$Q_{porous}^{s,p\to l,d} = \Phi \cdot k_{porous}^{s,p\to l,d} \cdot (C_{l,d}^0 - C_{l,d}) \frac{C_{s,p}}{C_{Ln\_pure}} \left(1 - \frac{C_{l,p}}{C_{Ln\_pure}}\right) \quad \text{Eq. 110}$$

where the reaction rate constants $k_{porous}^{s,d\to l,d}$, $k_{porous}^{s,d\to l,p}$ and $k_{porous}^{s,p\to l,d}$ describe volume average reaction rates inside the porous media. Since the kinetics in the equations above occur at the fuel-pore interfaces inside the porous media, all reaction rates are assumed to be linear to the porosity $\Phi$.

## 9.4 Materials Properties Settings

We will focus on the study of Ce and the same materials properties as in pore-scale model will be used here. However, with the porosity $\boldsymbol{\Phi}$ and a constant Ln generation rate $\dot{\boldsymbol{q}}$ in the fuel, the actual uniform Ce generation rate in the porous media can be estimated as: $\dot{\boldsymbol{q}} \cdot (\mathbf{1} - \boldsymbol{\Phi})$. Moreover, three reaction rate constants as mentioned earlier will be included. Therefore, in addition to the parameters listed in **Table 14**, four more parameters are listed as in **Table 17**.

**Table 17 Additional parameters for the porous media simulation.**

| Kinetics | Parameters | |
|---|---|---|
| Reaction at the | $k_{dr}^{s,d\to l,d}$ $(\mathrm{s}^{-1})$ | $10^{-7}$ |

| | | |
|---|---|---|
| interface between porous media and the pore | $k_{dr}^{s,d\to l,p}$ $(s^{-1})$ | $10^{-1}$ |
| | $k_{dr}^{s,p\to l,d}$ $(s^{-1})$ | $10^{-2}$ |
| Porosity | Φ | 0.01 |

## 9.5 Simulation Results

An example of the simulation using porous model is given in Figure 81. As shown in the figure, the Ln precipitation only occurs at the gap, which is similar to the results predicted by the pore model.

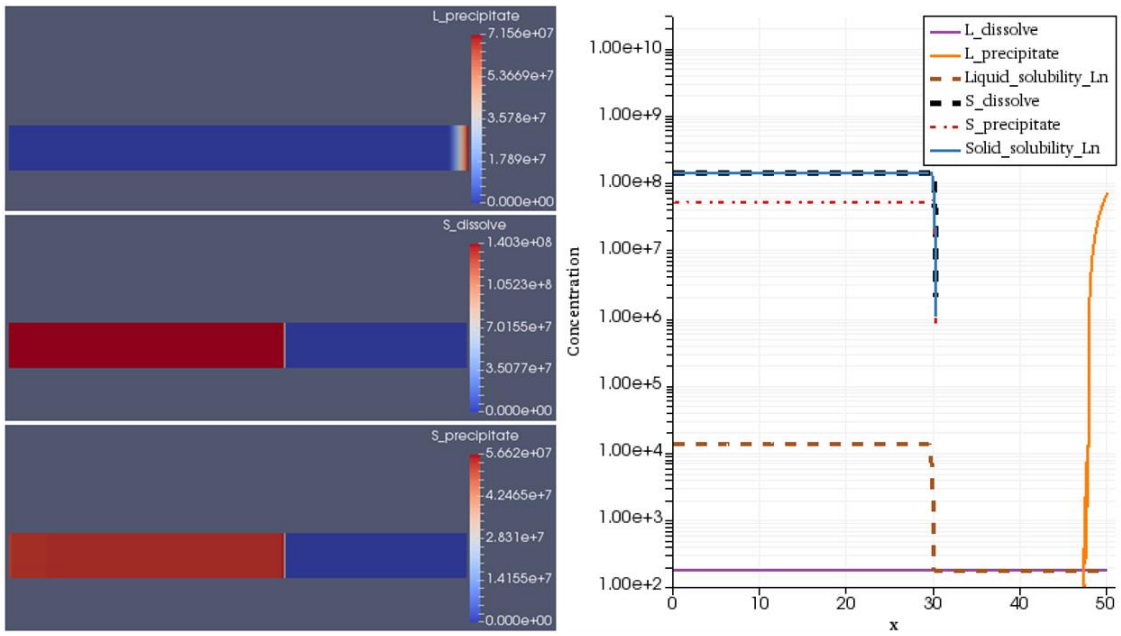


**Figure 81 Distribution of Ce concentration along 50μm after reaching 5% burnup using a 1D temperature profile with a temperature gradient of 0.05K/μm and highest temperature 855K.**

## 9.6 Parameters Testing

The additional unknown parameters introduced by the porous media are tested individually. All the other parameters remain the same as listed in Table 17.

a) Porosity Φ

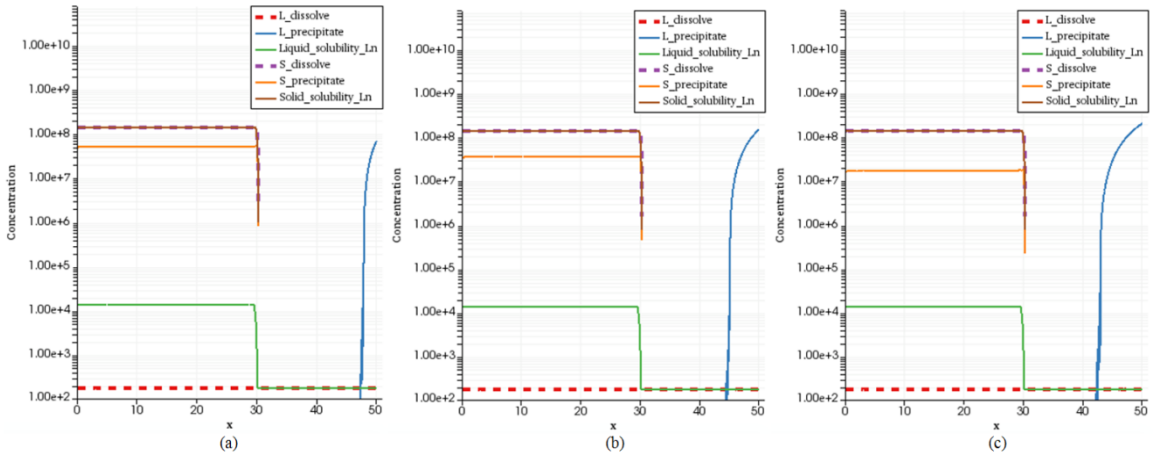


**Figure 82 Ce distribution at 5% burnup simulation with Φ from left to the right: 0.01, 0.05 and 0.1.**

Since the liquid Cs-filled pores provide paths for Ce to migrate at high speed, an increasing Φ will enhance the liquid-like transport and therefore more Ce can move from the porous media into the gap and precipitate out on the cold side of the gap. An increasing amount of Ln precipitates has been observed as the porosity goes up from left to the right in Figure 82.

b) Reaction rate constant $k_{porous}^{s,d\rightarrow l,d}$

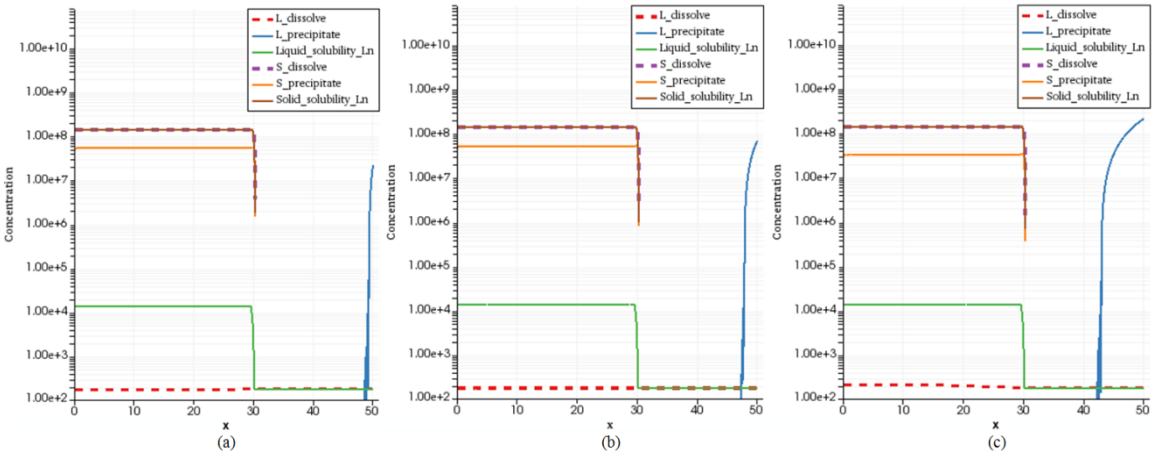


**Figure 83 Ce distribution at 5% burnup simulation with $k_{porous}^{s,d\rightarrow l,d}$ (1/s) from left to the right: $10^{-8}$, $10^{-7}$, $10^{-6}$.**

The reaction rate constant $k_{porous}^{s,d\rightarrow l,d}$ $(1/s)$ determines the rate of reaction between the dissolved Ln in solid fuel and in liquid metal solution. With a larger value of $k_{porous}^{s,d\rightarrow l,d}$, more Ce solute from the fuel will be desorbed into liquid metal solution and transport

into the gap. As a result, more Ce precipitates form on the right side of the gap with the increasing $k_{porous}^{s,d\to l,d}$.

c) Reaction rate constant $k_{porous}^{s,p\to l,d}$

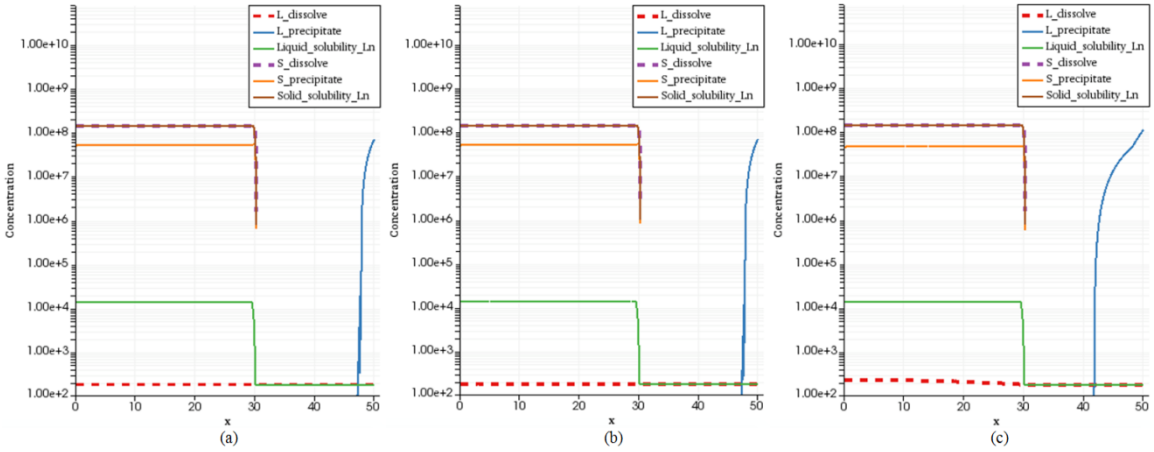


**Figure 84 Ce distribution at 5% burnup simulation with $k_{porous}^{s,p\to l,d}$ (1/s) from left to the right: $10^{-3}$, $10^{-2}$ and 10.**

The parameter $k_{porous}^{s,p\to l,d}$ $(1/s)$ describes the rate of Ce precipitates dissolution into the liquid metal solution. Therefore, an increasing value of $k_{porous}^{s,p\to l,d}$ yields a faster dissolution process which can be seen from comparison between (b) and (c). However, this is not reflected dramatically by comparing (a) and (b) which indicates that $k_{porous}^{s,p\to l,d}$ in a range of small values does not affect the model much.

d) Reaction rate constant $k_{porous}^{s,d\to l,p}$

In the case of porous media adjacent to the Na-filled gap, all the Ce precipitates form in the liquid metal solution concentrates on the cold side of the gap and there is no direct contact between the fuel and the Ce precipitates in the liquid metal. However, $k_{porous}^{s,d\to l,p}$ only takes effects when a diffusion couple forms between the Ce precipitates in liquid solution and the fuel so that inter-diffusion can occur at the fuel/liquid-metal interface. To test this parameter, we consider a specific condition where the fuel swells to contact with the clad and the liquid Na in the gap enters the pores in the porous media. In this case, only the porous media block is considered with pores filled with liquid Na instead

of liquid Cs.

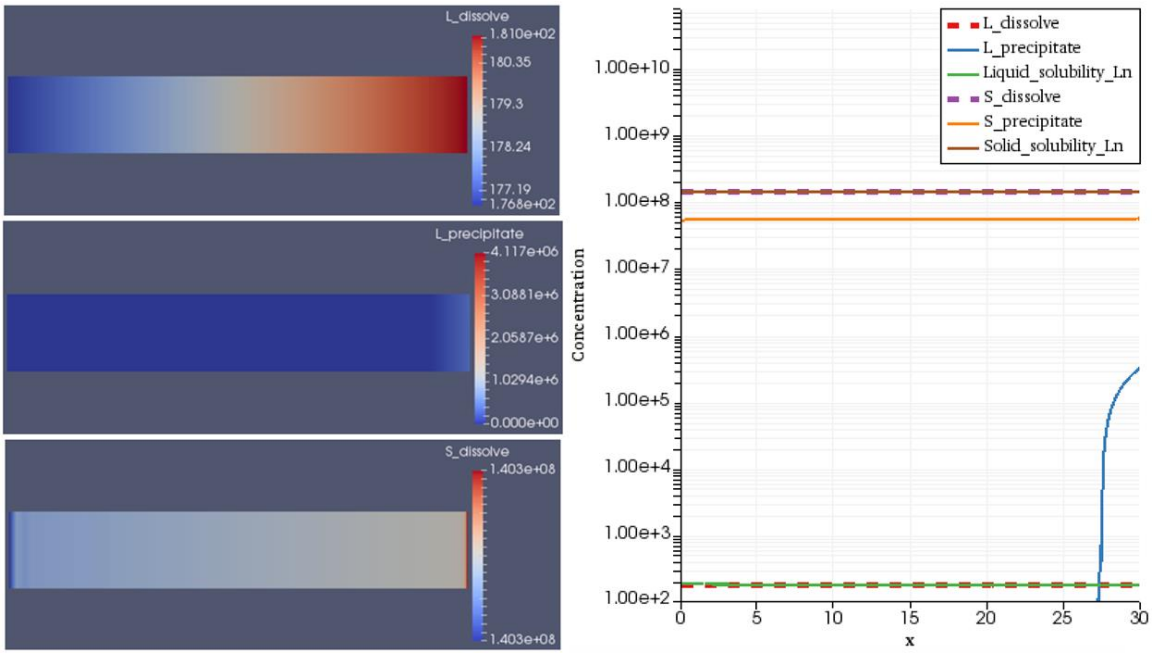


**Figure 85 Distribution of Ce concentration along 30μm in porous media after reaching 5% burnup using a 1D temperature profile with a temperature gradient of 0.05K/μm and highest temperature 855K.**

Figure 85 shows the Ce concentration distribution in porous media with a length of 30μm and the interconnected pores are filled with liquid Na. Ln precipitation tends to form on the cold side of the porous media block while the other Ce concentration such as Ce solute and precipitates in the fuel present a flat distribution.

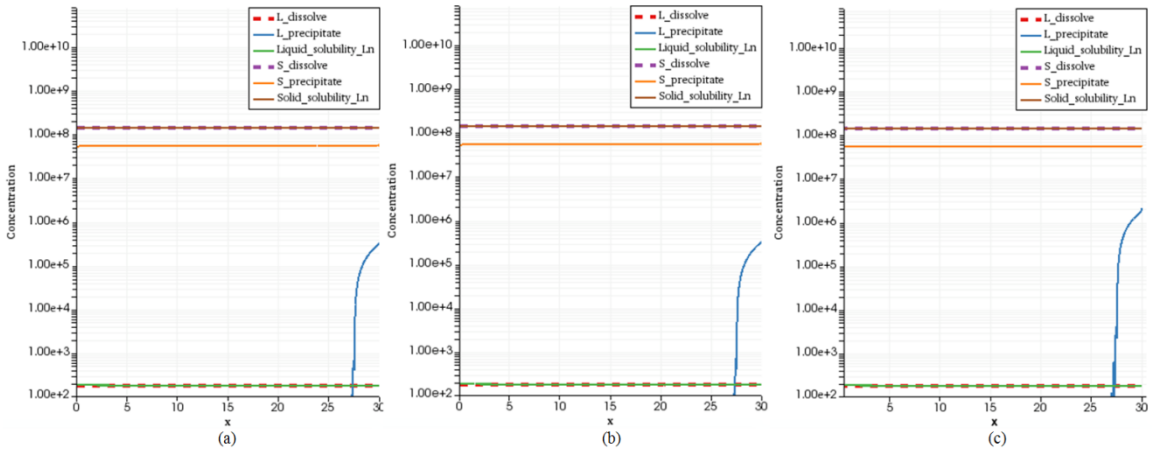


**Figure 86 Ce distribution at 5% burnup simulation with $k_{porous}^{s,d\rightarrow l,p}$ ($s^{-1}$) from left to the right: $10^{-3}$, 0.1 and 10.**

As shown in Figure 86, different values of $k_{porous}^{s,d\rightarrow l,p}$ $(1/\mathrm{s})$ have been tested. In consistence with the pore-scale model, liquid metal pores act as a sink for Ce, i.e. dissolved Ce in the fuel tend to enter the pore to contribute to the formation of the precipitation and a larger $k_{porous}^{s,d\rightarrow l,p}$ results in more Ce precipitates in liquid metal formed at cold locations. This is clearly displayed comparing (b) with (c). The model has much less sensitivity to a small value of $k_{porous}^{s,d\rightarrow l,p}$ since a similar amount of Ce precipitates in liquid metal has been observed in (a) as that in (b).

## 9.7 Conclusion

The 1-D model of Ln transport in porous media adjacent to Na-filled gap has been developed. The fast Ln liquid-like transport in porous media will be limited compared with that in liquid metal bulk. The properties of porous media have been considered in reactions and diffusion process by including porosity in physical kinetics. In addition, three more reaction rate constants are introduced as parameters to describe various reactions between relevant Ln concentration variables. All the additional unknown parameters introduced in porous media have been tested. Especially, the porosity appears to enhance the Ln liquid-like transport and the porous media with larger porosity present more Ln precipitation formation in the gap.

# 10 Solid Diffusion Modelling

The project focuses on 'liquid-like' transport, we also investigated the possibility of develop solid diffusion model to study the lanthanide transport. There simulations are at the preliminary status, and more studies are needed in the future to the solid diffusion transport.

## 10.1 Lanthanide Solid Diffusion in Fuel by BISON

Los Alamos National Laboratory, as collaborating national laboratory, conducted the Ln solid diffusion using MOOSE/BISON.

Two phases of cerium exist in U-Zr or U-Pu-Zr fuels: bcc $\delta-\text{Cerium}$ above 993K and fcc $\gamma-\text{Cerium}$ below 993K. Solid diffusion coefficients for $\delta-\text{Cerium}$ in U-10Zr (at %) have been reported with $\pm 50\%$ uncertainty. Activation energy ($Q$) for $\delta-\text{Cerium}$ can be derived from these data. Assumptions about $\gamma-\text{Cerium}$ were derived from data on cerium self-diffusion from both phases; A wide range of reasonable $Q$ values were tested. These data are incorporated into BISON to perform the solid diffusion calculation. As time evolves, cerium grows into our model in proportion to the rate of fission and migrates in accordance with solid diffusion properties based on local temperature.

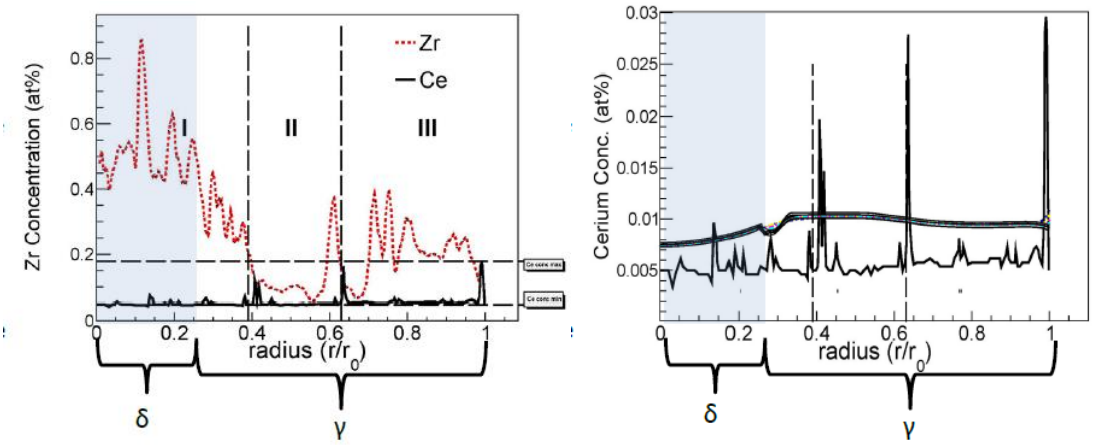


**Figure 87 Zr profile (red dot) and a scaled Ce profile (black solid) from EBR-II rod DP11.**

As shown in Figure 87, data from EBR-II rod DP11 show a Zr profile (red dot) and a scaled Ce profile (black solid). Horizontal dashed lines indicate relative minimum and maximum for Ce concentrations. Vertical dashed lines designate three zones created by Zr redistribution. The Ce profile has spikes generally correlated with the boundaries of the zones and at the rod periphery. Rod-averaged Zr concentration is ~22 at%. At 10 % burnup, Ce has a rod-averaged concentration that is just under 1%.

## 10.2 Multiscale Approach to Analyzing the Transport of Ln in U-Zr

In this study, a multi-scale approach consisting of density functional theory calculations, kinetic Monte Carlo simulations and continuum level modeling were used to study lanthnide transport through the UZr fuel pin. It was found that the lanthanide transport phenomenon through the solid was too slow to explain the observed FCCI and that controlling liquid-based transport through the pores in the metallic fuel is key to optimizing fuel performance.

### 10.2.1 Density Functional Theory Calculations

To study the diffusion of lanthanum in the uranium zirconium fuel, a bcc unit cell of UZr [162] containing 50 atomic percent uranium and 50 atomic percent zirconium (72.6 wt% U) was constructed. Next, the optimal lattice parameter of the unit cell was determined from performing DFT calculations on the unit cell. It was determined that the optimal lattice parameter was 3.6 Å. This number is consistent with earlier experimental and theoretical results [ 163 ] and will be used in all subsequent calculations.

Spin polarized density functional theory calculations were carried out using the Vienna ab initio simulation package (VASP) with the implementation of the Projector-Augmented-Wave (PAW) pseudopotentials [ 164 , 165 ]. A generalized gradient approximation (GGA) exchange correlation functional was used as parameterized by Pardew, Burke and Ernzerhov[166]. The cutoff energy of 500 eV and a Methfessel-Paxton smearing of the first order of width 0.1 eV were used in the simulations [167]. A 3×3×3 supercell of the UZr alloy was constructed containing 54 atoms in total. An additional lanthanum atom was placed at an octahedral (O) or tetrahedral (T) site. All symmetrically and translationally inequivalent sites were checked. The Brillouin zone was sampled through a 3×3×3 Monkhorst-Pack K-point mesh [168]. An accuracy of ($10^{-7}$ eV) was used for the electronic energy convergence. Convergence with respect to the cutoff energy and the k-point mesh was checked. Furthermore, the structure was allowed to relax until the forces acting on the atoms were less than 0.05 eV/Å. To study the stability of interstitial La, we computed the classical binding energies defined as :

$$E_{binding} = E_{La\ in\ UZr} - E_{UZr} - E_{La} \qquad \text{Eq. 111}$$

The first term on the right hand side of equation 111 refers to the total energy of the supercell containing the interstitial La atom. The second term in the expression is the energy of the supercell without the interstitial La. The last term (*ELa*) refers to the energy of a single La atom taken from the bulk hcp La structure. There are three symmetrically distinct sites to explore. The results are summarized in Table 18:

**Table 18. The classical binding energies for La atoms placed at symmetrically distinct sites in the bcc UZr alloy**

| | Face-centererd O-site | Edge-centered O-site | T-site |
|---|---|---|---|
| $E_{binding}$ $(eV)$ | -0.43 | +0.68 | +0.52 |

From Table 18, we notice that octahedral sites within the plane of U atoms in the UZr bcc structure are the most stable and most energetically favorable with respect to binding La atoms. Hence, we will next study the hopping of La atoms between these sites.

Lanthanum atoms are expected to occupy the face centered octahedral interstitial sites since they are the most stable and diffuse by hopping from one site to the neighboring ones. In this study, we studied transitions to the first nearest neighbors (8 available to each site) and second nearest neighbors (4 available to each site since we don't consider these transitions when the diffusion path is blocked by a body-centered atom). Possible paths for hopping are illustrated in Figure 88.

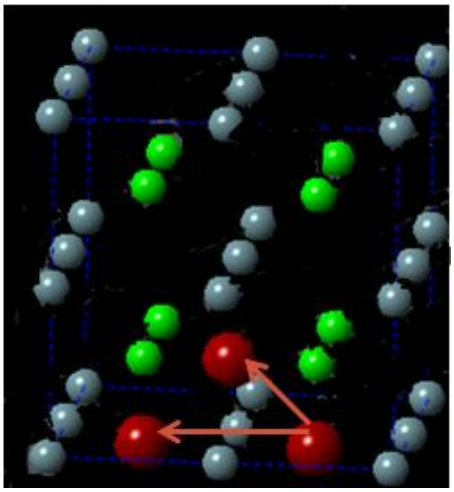

**Figure 88. Possible hopping paths for lanthanum atoms occupying octahedral interstitial sites in the UZr alloy. Zr: Green atoms, U: Gray atoms, La: Red atoms**

Transition states were determined via the climbing image nudged elastic band method [169]. An initial chain of images was constructed between the initial and final structures using linear interpolation between the two endpoints of the potential energy surface. A spring force between the adjacent images was applied to maintain constant the spacing between the images. Each image was optimized with the quick-min nudged elastic band algorithm [170]. All the atoms were allowed to relax simultaneously and the transition state was approximated by the image with the highest energy.

The hopping rates can be described via accounting for discrete energy levels available to the interstitial La atom by the quantum-mechanical version of the classical harmonic transition state theory [171]
:

$$k_{IF} = \Gamma_{IF} \ exp(-E_a/k_B T) \qquad \text{Eq. 112}$$

where $k_{IF}$ is the hopping rate from an initial O site to a final O site (a nearest neighbor or a next nearest neighbor), $\Gamma_{IF}$ is the hopping rate at infinite temperature, *kB* is the Boltzmann constant, T is the temperature of the simulation and *Ea* is the activation energy barrier for hopping from the given initial site to the final site under consideration. The infinite temperature hopping rate may be estimated as [171]:

$$\Gamma_{IF} = \frac{\prod_{i=1}^{3} f\left(h\nu_{I,i}/2k_B T\right)}{\prod_{j=1}^{2} f\left(h\nu_{TS,j}/2k_B T\right)} \qquad \text{Eq. 113}$$

where the function *f* is given by$f(x) = \sinh(x)/x$, and $\nu_I$, and $\nu_{TS}$ are the normal mode frequencies at the initial and transition state site respectively. Finally, the activation energy barrier may be approximated as:

$$E_{a,IF} = E_{cl,IF} + \varepsilon_{zp}^{TS} - \varepsilon_{zp}^{I} \qquad \text{Eq. 114}$$

where $E_{cl,IF}$ is the classical energy barrier for the hop from the initial to the final state, and $\varepsilon_{zp}^{TS}$ and $\varepsilon_{zp}^{I}$ are the zero point energies of the La atom at the initial site and the transition state site. It was determined that the energy barrier for path 1 (to the nearest neighbor) is 0.53 eV and that the energy barrier for path 2 (to the next nearest neighbor) is 1.2 eV.

### 10.2.2 Kinetic Monte Carlo Simulations

Next, and to estimate the diffusion coefficient, a single lanthanum atom was placed on a randomly selected O-site. Since for the current study, we are interested in dilute lanthanum concentrations in the fuel, the interactions between the lanthanum atoms are ignored and the motion of a single lanthanum atom is tracked in an infinite lattice. At each step of the kMC simulation, the lanthanum atom may hop from a face-centered octahedral site to one of its eight nearest neighboring face-centered O-sites (distance $a/\sqrt{2}$) or its four next neighboring face-centered O-sites (distance *a*) . Each kMC move included obtaining the rates (*ki*) for all the possible transitions from the current configuration. A choice for the hop was selected by generating a random number to perform the hop according to the condition:

$$\sum_{i=1}^{j-1} k_i \leq rK \leq \sum_{i=1}^{j-1} k_i \qquad \text{Eq. 115}$$

In the equation, r is the generated random number and K is the sum of the rates of all possible hopping processes. The clock is then advanced by $-\ln(\sigma)/K$ where σ is another random number. To obtain good results, the simulation must be run for a relatively long time, repeated several times and averaged. Then, the diffusion coefficient may be calculated using the relation:

$$D = \lim_{t\to\infty}\left[\frac{1}{6t}\langle|\boldsymbol{R}(t) - \boldsymbol{R}(0)|^2\rangle\right] \qquad \text{Eq. 116}$$

In the equation ***R(t)*** is the position of the lanthanum atom at time t. A typical mean squared displacement plot is shown in Figure 89

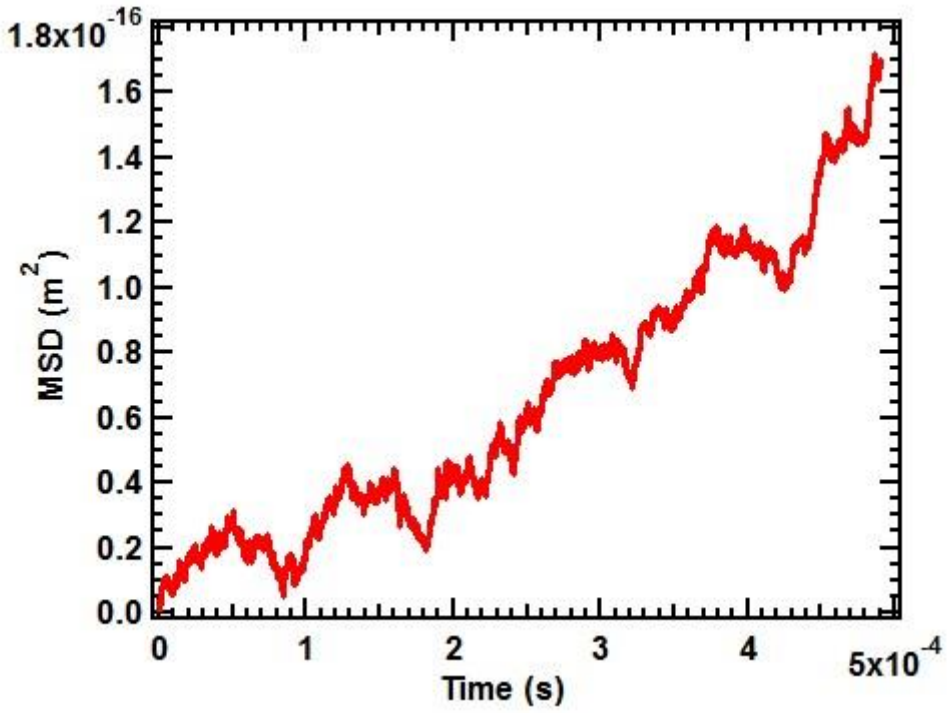


**Figure 89. A typical Mean Squared Displacement plot recorded at 700 K.**

The diffusivity results may be fitted to the Arrhenius equation: $D = D_o exp(-E_a/k_B T)$ In this equation *Do* is the diffusivity at infinite temperature, $E_a$ is the diffusion activation energy, $k_B$ is the Boltzmann constant and $T$ is the temperature. The fit is shown in Figure 90. From the fitting, we find that $D_o = 2.18 \times 10^{-10} m^2/s, E_a = 0.54$ eV.

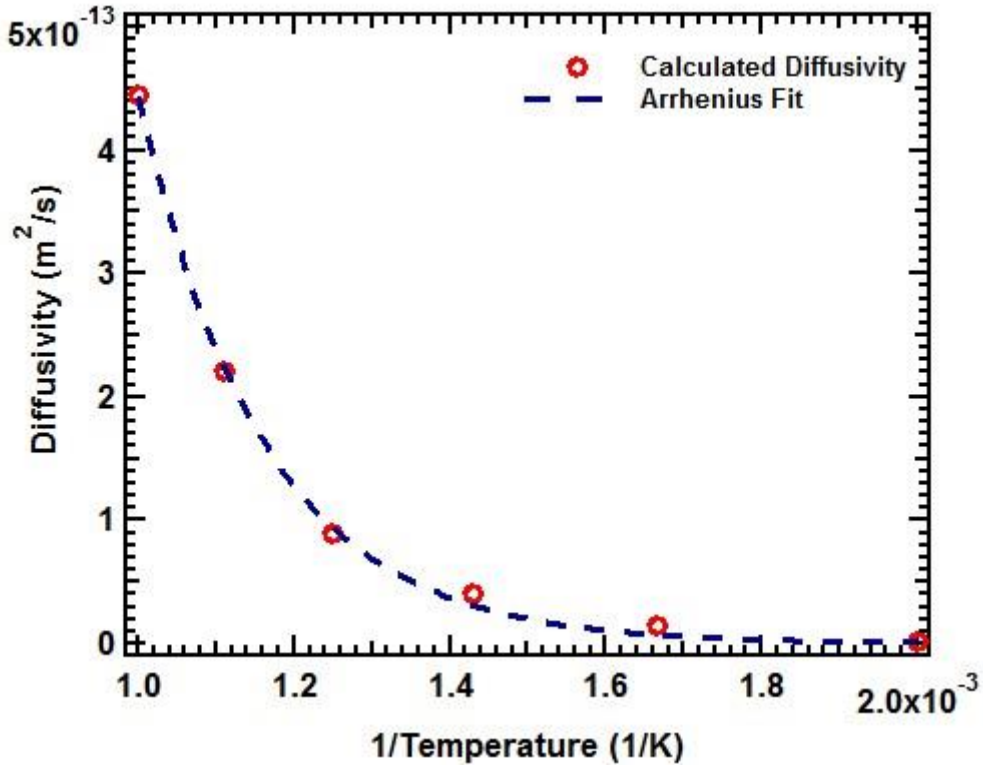


**Figure 90.The Arrhenius Fit for the calculated diffusivity at different temperatures**

The calculated diffusivity results are consistent with available experimental data which found that the diffusivity of La in UZr to be in the range [$1\times10^{-13}$- $8\times10^{-12}$] $m^2/s$ at 1111 K [172]. In addition, the same study experimentally measured the diffusivity of Ce (another lanthanide) in the UZr alloy and reported a value of $6\times10^{-14}$ $m^2/s$. These values are consistent with the diffusivity results derived computationally. It should be pointed out, however, that we used a bcc structure for UZr, but this structure changes as a function of temperature where different phases of the material are present. In addition, the fuel in a realistic situation is exposed to radiation damage creating vacancies in the fuel. We expect these vacancies to expedite the transport process and these effects have not been accounted for in this study. Nevertheless, the reported results are consistent with the literature values and will be used in a continuum level model to obtain better estimates for the timescale needed for the concentration of the fission product in the fuel to reach a steady state.

### 10.2.3 Continuum Level Modeling

Next, and from an engineering point of view, it is important to obtain an estimate for the amount of time needed for the lanthanum concentration across the fuel pin to reach a steady state distribution. The mass transport of lanthanum in the UZr metallic fuel may be described by employing Fick's law as:

$$\frac{\partial C}{\partial t} = \quad -\boldsymbol{\nabla}.(-D\boldsymbol{\nabla}C) \qquad \text{Eq. 117}$$

In the equation the diffusivity is a function of temperature which itself is a function of the radius of the fuel pin $D\big(T(r)\big)$. In this work we will ignore the generation of the fission product through the source term because we are only concerned with examining the effect of the temperature dependence of diffusivity on the mass transport. Furthermore, we will assume that the temperature instantaneously reaches its parabolic steady state temperature characteristic of a fuel pin.

$$T(r) = ar^2 + b \qquad \text{Eq. 118}$$

where the quantity, *a*, is negative and the diffusivity exhibits its dependence on the temperature through the Arrhenius equation. This steady state temperature profile is shown in Figure 91.

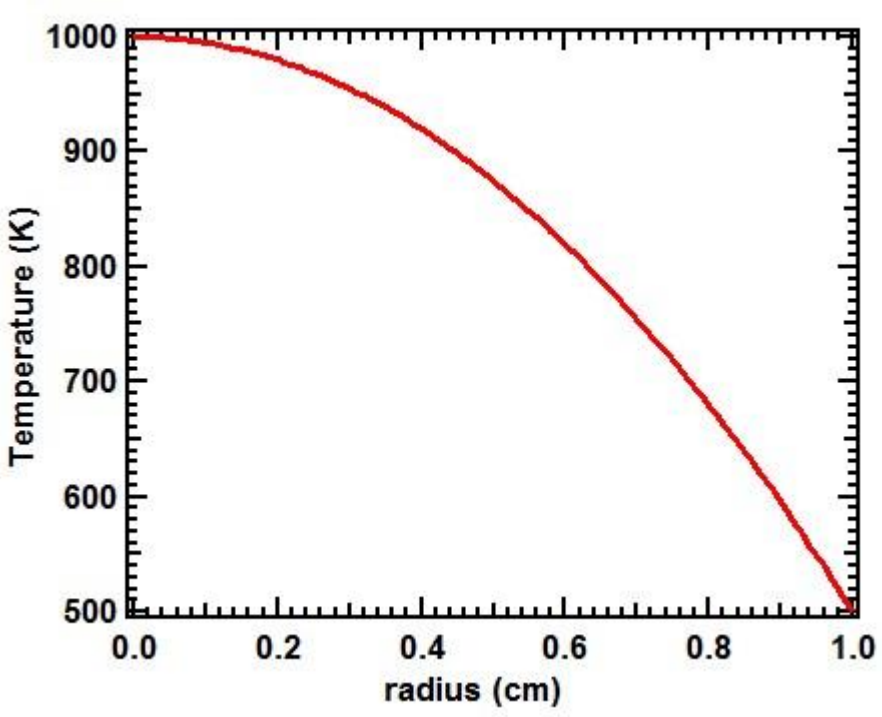


**Figure 91.The temperature distribution across the radius of the fuel pin. The temperature profile is parabolic and its vertex is at the center of the fuel where the temperature is highest. The parameters used are $\boldsymbol{a = -500\,K/cm^2}$, $\boldsymbol{b = 1000\ K}$**

Finally, only radial La migration will be considered as axial temperature gradients are relatively small and axial migration has not been observed for other elements [173].

Hence, the governing equation may be written in cylindrical coordinates as:

$$\frac{\partial C(r,t)}{\partial t} = D(r)\frac{\partial^2 C(r,t)}{\partial r^2} + \frac{1}{r}D(r)\frac{\partial C(r,t)}{\partial r} + 2arD_o\frac{E_a}{k_B\big(T(r)\big)^2}exp\big(-E_a/k_BT(r)\big) \quad \text{Eq. 119}$$

The final term is the Soret term and is obtained through the application of the chain rule: $\frac{dD}{dr} = \frac{dD}{dT}\frac{dT}{dr}$.

Neumann boundary conditions will be used at the center of the cylinder:

$$\left.\frac{\partial C}{\partial r}\right|_{r=0} = 0 \quad \text{Eq. 120}$$

At the surface of the cylindrical fuel pin, the lanthanum fission product escapes the fuel pin and deposits on its surface or dissolves in the liquid sodium which separates the pin from the cladding. This flux at the surface of the fuel pin (at radius R) may be described by an appropriate boundary condition. However, since we are only interested in studying the effect of the diffusivity on the transport within the fuel pin, we will utilize a zero-flux boundary condition:

$$\left.\frac{\partial C}{\partial r}\right|_{r=R} = 0 \quad \text{Eq. 121}$$

Finally, we will assume a linear initial lanthanum distribution given by: $C(r, t = 0) = C_0(1 - r)$

The problem was solved numerically using finite differences. Central differencing in space and forward differencing for time were implemented. Furthermore, ghost points were used at the boundaries to enable a better approximation of the derivatives there. All simulations were converged with respect to the time step and the mesh size and the numerical procedures were implemented in MATLAB. In the simulations, the radius of the fuel pin was chosen to be R = 1 cm, the temperature gradient was given by a = -250 K/cm$^2$ (b = 700 K), Co = 0.1 mol/cm$^3$ and the diffusivity was described via the parameters of the Arrhenius equation as determined from the previous section. The results are shown in Figure 92.

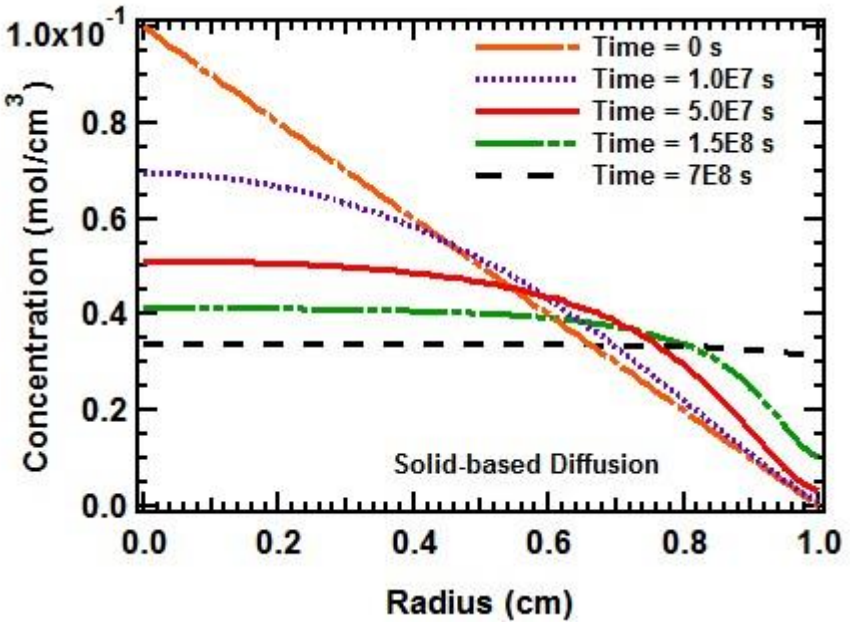


**Figure 92. The evolution of the lanthanum concentration profile across the radial direction of the fuel pin as a function of time via considering diffusion through the solid crystal structure only**

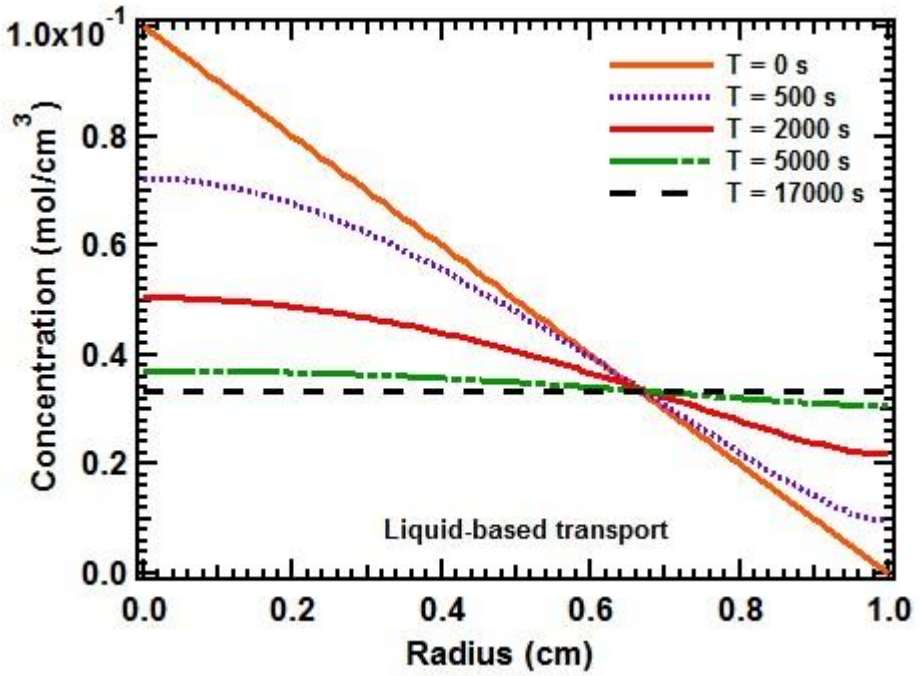


**Figure 93. The evolution of the lanthanum concentration profile across the radial** direction of the fuel pin as a function of time via considering diffusion through the liquid-sodium filled pores only

We use the results reported section 7 of this report to compare the solid state diffusion with liquid-based diffusion. From fitting the Arrhenius equation to the set of data for

the diffusivity of Ce in liquid sodium, we find that $D_0 = 3 \times 10^{-4}$ m2/s and $E_a = 0.15\ eV$. Using these parameters in the Arrhenius relation for diffusivity, we run the simulation again. The results are included in Figure 93

By comparing Figure 92 and Figure 93, it is clear that diffusion through the liquid-metal filled pores in the crystal UZr lattice dominate the diffusion process and can lead to a considerable change in the concentration profile in a very short period of time relative to the solid-based diffusion where decades are needed to reach the steady state concentration profile. These findings agree with the liquid-like mechanism for transport in studying FCCI of the present project.

Moreover, and in a nuclear reactor, the fuel pin is undergoing fission and radiation damage through collision cascades triggered by primary knock-on atoms. These processes lead to more defects and vacancies being formed and increase the porosity of the solid fuel. This in turn increases the liquid-filled porous network and enhances its effect in transporting lanthanides to the fuel surface and initiating FCCI. Therefore, it is very important to inhibit the liquid-based mass transport of lanthanides to the periphery in order to delay or prevent FCCI. Future efforts to optimize the performance of UZr metallic fuels should consider liquid-based transport since this appears to be an important mechanism in initiating the FCCI phenomenon.

### 10.2.4 Conclusion

Lanthanide transport to the fuel periphery is an important process for understanding the mechanisms and time-scales involved in the FCCI phenomenon. In this study, lanthanide transport through the uranium-zirconium alloy was studied at high temperatures relevant for the operation of these fuels in SFRs. It was found that the diffusivity through the crystalline structure was on the order of $10^{-13}$ $m^2/s$ at 1000 K. In addition, it was shown that solid-based diffusion was too slow to explain FCCI. Liquid-based transport through the liquid-filled pores in the fuel is thought to play an important role in controlling the FCCI process. Future efforts to optimize the performance of these fuels must account for the liquid-based diffusion of lanthanides through the pores in the fuel.

## 11. Conclusion

One of the key concerns of using metallic fuels is the cladding degradation due to fuel-cladding chemical interactions (FCCI). The major contribution to FCCI arises as Ln migrates to the periphery of the fuel and then contacts the cladding due to swelling or transport through the sodium gap eventually. The FCCI is recognized as a long-term, high-burnup cause of the clad failures. Therefore, it is important to understand the redistribution of lanthanide fission products and migration to the fuel surface. Based on available post-irradiation examination (PIE) data, pores filled with liquid metal (e.g. Cs) can be the fast paths for Ln migration to the fuel surface, then a 'liquid like' Ln transport theory for the metallic fuel during burning was developed. For studying, verifying and validating the theory, the present project conducted both experiment and modeling development.

For experiment, the study measured the solubility of the major lanthanides (Pr, Ce, Nd) that play important roles in FCCI in liquid sodium, liquid cesium and liquid sodium-cesium mixtures. It was found that all the lanthanides considered have a much smaller solubility in liquid sodium than in liquid cesium, and the solubility decreases with the faction of sodium in the liquid sodium-cesium mixtures. Considering that the sodium is the bonding materials of the cladding-fuel gap, while cesium is one of the fission products and may fill the pore in the fuel formed during burning, the experimental findings support the 'liquid-like' transport theory.

For the modeling development, fundamental data (the diffusion coefficients and solubilities of lanthanides in the liquids) were first calculated. Three models for solubility calculation were investigated. It was found that the method based on DFT-Phono calculation leads to simulation results agreeing well with experimental measurements. For diffusion coefficient calculations, first-principles molecular dynamic simulation was applied to simulate Ln-Na and Ln-Cs binary system. It was found that the diffusion coefficients are in the order of $10^{-5}$ $cm^2/s$. The diffusion coefficient of a give lanthanide is always higher in liquid Na than Cs, the higher diffusion coefficient in liquid Na makes it possible for lanthanides to pass through the Na-filled gap. The diffusion coefficient decreases with decreasing temperature, so the lanthanide will finally deposit on the cladding surface.

For studying Ln transport in liquid pore, an analytical solution was first developed. Based on the analytical solution, the importance of Soret effects on material transport with a temperature gradient was identified. Then the measured and simulated fundamental data were used as input for the transport model using MOOSE/BISION for Ln transport in pore and porous medium. In the simulations models, the effects of both the Ln concentration gradient and Soret effects on Ln transport were considered.

The modeling results indicated that the pores filled with liquid cesium can be a fast path for Ln transport from the bulk fuel to the fuel surface. It was also found that most of Ln precipitates at the cladding inner surfaces, which also supports the 'liquid-like' transport theory.

The project also developed solid-diffusion models based on BISON and a multi-scale approach. The modeling results indicate that solid-based diffusion was too slow to explain FCCI. Therefore, liquid-based transport through the liquid-filled pores in the fuel is thought to play an important role in controlling the FCCI process.

The present study advances the understanding of Ln migration and redistribution mechanism in the metallic fuel during operation and provides fundamental data for mitigating FCCIs.

# 12. Publications

## 12.1 Journal Publications

1. Li, Xiang, et al. "Ab-initio molecular dynamics study of lanthanides in liquid sodium." Journal of Nuclear Materials 484 (2017): 98-102.
2. Isler, Jeremy, et al. "Experimental solubility measurements of lanthanides in liquid alkalis." Journal of Nuclear Materials 495 (2017): 438-441.
3. Isler, J., and Zhang, J., "Examination of Solubility Models for the Determination of Transition Metals within Liquid Alkali Metals." Metals 6.7 (2016): 144..
4. Samin, Adib, et al. "Ab initio molecular dynamics study of the properties of cerium in liquid sodium at 1000 K temperature." Journal of Applied Physics 118.23 (2015): 234902.
5. Li, X., Zhang, J., Unal C., Mariani R. D., "Behaviors of Ce, Pr and Nd in liquid Cesium by Ab-initio molecular dynamic simulation." Journal of Nuclear Materials (2017), under review.
6. Xie Y., Zhang J., Li X., Isler J., Bensonc M. T., Mariani R. D., "Lanthanide Migration and Immobilization in Metallic Fuels." Progress in Nuclear Energy (2018), Under Review.
7. Samin A., Zhang J., "An analytical solution for Soret diffusion of a dilute species in a linear temperature profile." (2018), Will submit.

## 12. 2 Conference Publicaitons

1. Unal C., Li X., Isler J., Adib S., Zhang J., Matthews C., Arnold C., Galloway, J., Carlson N., Mariani R., "Modeling of Lanthanide transport in metallic fuels: Recent Progress." International Conference on fast reactors and related fuel cycles: next generation nulcear systems for sustainable development, IAEA-CN245-350
2. Li X., Samin A., Zhang J., "Ab-Initio Molecular Dynamics Study of the Solubility and Diffusion Coefficient of Cerium in Liquid Sodium", ANS Winter Conference, ANS Transaction 113 (1), 176-177, 2015
3. Unal C., Matthews C., Li X., Isler J., Zhang J., "A potential mechanism for lanthanide transport in metallic fuels." ANS summer Conference, ANS Transaction 116 (1), 501-503, 2017

## 12. 3 Presentation

1. Li X., Samin A., Zhang J., "Ab-Initio Molecular Dynamics Study of the Solubility and Diffusion Coefficient of Cerium in Liquid Sodium." ANS Winter Conference, Washington DC, Nov.12, 2015
2. Unal C., Matthews C., Li X., Isler J., Zhang J., "A potential mechanism for lanthanide transport in metallic fuels." ANS summer Conference, San Francisco, CA, Jun.15, 2017.
3. Isler J., Zhang J., Mariani R., "Experimental Solubility of Lanthanides in Liquid

Sodium.” Materials Science and Technology (MST), Salt Lake, Utah, Oct. 25, 2016.

## 12. 3 Thesis

1. Isler, Jeremy Payton. Interactions of Lanthanides and Liquid Alkali Metals for" Liquid-Like" Lanthanide Transport in U-Zr Fuel. Diss. The Ohio State University, 2017.
2. Li, Xiang. Studies of Liquid-like Lanthanide Transport Behaviors in Metallic Nuclear Fuels. Diss. The Ohio State University, 2017.

## 13. References


1 Delage, F., et al. "Status of advanced fuel candidates for sodium fast reactor within the Generation IV International Forum." Journal of Nuclear Materials 441.1-3 (2013): 515-519.

2 Carmack, W. J., et al. "Metallic fuels for advanced reactors." Journal of Nuclear Materials 392.2 (2009): 139-150.

3 Carmack, W. Jon, et al. "Metallography and fuel cladding chemical interaction in fast flux test facility irradiated metallic U-10Zr MFF-3 and MFF-5 fuel pins." Journal of Nuclear Materials 473 (2016): 167-177.

4 Pahl, R. G., et al. "Irradiation behavior of metallic fast reactor fuels." Journal of Nuclear Materials 188 (1992): 3-9.

5 Hofman, G. L., L. C. Walters, and T. H. Bauer. "Metallic fast reactor fuels." Progress in Nuclear Energy 31.1-2 (1997): 83-110.

6 Keiser, D.D., “Technical Report ANL-NT-240”, Argonne National Laboratory - West, Idaho Falls, ID, 2006.

7 Hofman, G. L., S. L. Hayes, and M. C. Petri. "Temperature gradient driven constituent redistribution in U-Zr alloys." Journal of nuclear materials 227.3 (1996): 277-286.

8 Isler, Jeremy Payton. Interactions of Lanthanides and Liquid Alkali Metals for" Liquid-Like" Lanthanide Transport in U-Zr Fuel. Diss. The Ohio State University, 2017.

9 Hofman, Gerard L., et al. "Swelling behavior of U-Pu-Zr fuel." Metallurgical Transactions A 21.2 (1990): 517-528.

10 Kim, Yeon Soo, G. L. Hofman, and A. M. Yacout. "Migration of minor actinides and lanthanides in fast reactor metallic fuel." Journal of Nuclear Materials 392.2 (2009): 164-170.

11 Mariani, Robert D., et al. "Metallic fuels: The EBR-II legacy and recent advances." Procedia Chemistry 7 (2012): 513-520.

12 Pahl, R. G., C. E. Lahm, and S. L. Hayes. "Performance of HT9 clad metallic fuel at high temperature." Journal of Nuclear Materials 204 (1993): 141-147.

13 Keiser Jr, Dennis D., and Mark C. Petri. "Interdiffusion behavior in U-Pu-Zr fuel versus stainless steel couples." Journal of nuclear materials 240.1 (1996): 51-61.

14 Matthews, Christopher, et al. "Fuel-Cladding Chemical Interaction in U-Pu-Zr Metallic Fuels: A Critical Review." Nuclear Technology 198.3 (2017): 231-259.

15 Tsai, Hanchung. Fuel/cladding compatibility in irradiated metallic fuel pins at elevated temperatures. No. CONF-900804-9. Argonne National Lab., IL (USA), 1990.

16 Cohen, A. B., H. Tsai, and L. A. Neimark. "Fuel/cladding compatibility in U-19Pu-10Zr/HT9-clad fuel at elevated temperatures." Journal of Nuclear Materials 204 (1993): 244-251.

17 K. Nakamura, et al. “Reactions of U-Zr alloy with Fe and Fe-Cr alloy” Journal of Nuclear Materials, vol. 275 (1999) pp. 246-254.

18 Nakamura, Kinya, et al. "Equilibrium phase relations in the U–Zr–Fe ternary system." Journal of Nuclear materials 275.2 (1999): 151-157.

19 Park, Y., et al. "Diffusional Interaction Between U-10 wt pct Zr and Fe at 903 K, 923 K, and 953 K (630° C, 650° C, and 680° C)." Metallurgical and Materials Transactions A 46.1 (2015): 72-82.

20 Huang, K., et al. "Interdiffusion and reaction between uranium and iron." Journal of Nuclear materials 424.1-3 (2012): 82-88.

21 V. Raghavan, “Fe-U-Zr (Iron-Uranium-Zirconium),” Journal of Phase Equilibria, vol. 24 (2003) pp. 364.

22 Kurata M, et al. “Thermodynamic assessment of the Fe-U, U-Zr and Fe-U-Zr systems.” J. Alloys Compd., 1998, 271-273, 636-640.

23 Ogata, Takanari, et al. “Reactions between U–Zr alloys and Fe at 1003 K.” Journal of Nuclear Materials 441 (2013) 579–582.

24 Ogata, Takanari, et al. "Reactions between U-Pu-Zr alloys and Fe at 923 K." Journal of nuclear science and technology 37.3 (2000): 244-252.

25 Nakamura, Kinya, et al. "Reactions of uranium-plutonium alloys with iron." Journal of nuclear science and technology 38.2 (2001): 112-119.

26 Aitkaliyeva, Assel, et al. "Fuel-Cladding Interaction Between U-Pu-Zr Fuel and Fe." Metallurgical and Materials Transactions E 2.4 (2015): 220-228.

27 Nakamura, Kinya, et al. "Phase relations in the quaternary Fe–Pu–U–Zr system." Journal of Nuclear Materials 304.1 (2002): 63-72.

28 Keiser, D. D., and M. A. Dayananda. "Interdiffusion between U-Zr fuelvs selected cladding steels." Metallurgical and Materials Transactions A 25.8 (1994): 1649-1653.

29 Keiser Jr, D. D., and M. A. Dayananda. "Interdiffusion between U-Zr fuel and

selected Fe-Ni-Cr alloys." Journal of Nuclear materials 200.2 (1993): 229-243.

30 C.W. Arnold, J. Galloway, C. Unal, “Modeling lanthanide transport in metallic fuels with BISON.” International Fuel Cycle Conference proceedings (2015). Paper 5084, Paris, France, September 21-24.

31 Mariani, Robert D., et al. "Lanthanides in metallic nuclear fuels: Their behavior and methods for their control." Journal of Nuclear Materials 419.1-3 (2011): 263-271.

32 A. Itoh, et al. Proc. 1997 Fall Meeting of the Atomic Energy Society of Japan, 1997, I66, 708.

33 Pahl, R. G., et al. "Experimental studies of U-Pu-Zr fast reactor fuel pins in the experimental breeder reactor-ll." Metallurgical Transactions A 21.7 (1990): 1863-1870.

34 Kim, Jun Hwan, et al. "Interaction between multi-component lanthanide alloy and ferritic-martensitic steel." *Metals and Materials International* 20.5 (2014): 819-824.

35 Ogata, Takanari, et al. "Reactions between U–Zr alloys and Fe at 923 K." Journal of nuclear materials 250.2-3 (1997): 171-175.

36 Bozzolo, G., et al. "Lanthanides migration in U–Zr based nuclear fuels." Journal of Nuclear Materials 407.3 (2010): 228-231.

37 Tsai, H., et al. "Irradiation performance of U-Pu-Zr metal fuels for liquid-metal-cooled reactors." Proc. of ICONE3 (1995): 23-27.

38 Kim, Jun Hwan, et al. "Formation of intermetallic compound at interface between rare earth elements and ferritic-martensitic steel by fuel cladding chemical interaction." Journal of Rare Earths 30.6 (2012): 599-603.

39 Kim, Jun Hwan, et al. "Reaction between a rare earth element and 9Cr-2W steel." Metals and Materials International 17.4 (2011): 535.

40 Moreau, J. M., et al. "A new phase in the Nd-Fe system: Crystal structure of Nd5Fe17." Journal of the Less Common Metals 163.2 (1990): 245-251.

41 Pawlik, Katarzyna, et al. "Phase composition investigations of the Nd-Fe alloys processed by various methods." Nukleonika 49 (2004): 27-31.

42 Van Ende, Marie-Aline, and In-Ho Jung. "Critical thermodynamic evaluation and optimization of the Fe–B, Fe–Nd, B–Nd and Nd–Fe–B systems." Journal of Alloys and Compounds 548 (2013): 133-154.

43 Chuang, Y. C., C. H. Wu, and Z. B. Shao. "Investigation of the Ce · Fe binary system." Journal of the Less Common Metals 136.1 (1987): 147-153.

44 Su, Xuping, and Jean-Claude Tedenac. "Thermodynamic modeling of the ternary

Ce–Fe–Sb system: Assessment of the Ce–Sb and Ce–Fe systems." Calphad 30.4 (2006): 455-460.

45 Johnson, Qu, et al. "Refinement of Th2Zn17 structure: Pr2Fe17." Acta Crystallographica Section B: Structural Crystallography and Crystal Chemistry 24.2 (1968): 274-276.

46 Zhang, W., C. Li, and X. Su. "The Fe-Pr (iron-praseodymium) system." Journal of phase equilibria 20.2 (1999): 158.

47 Cannon, J. F., D. L. Robertson, and H. T. Hall. "Synthesis of lanthanide-iron Laves phases at high pressures and temperatures." Materials Research Bulletin 7.1 (1972): 5-11.

48 Povoden-Karadeniz, E., et al. "Thermodynamic assessment of the La-Fe-O system." Journal of phase equilibria and diffusion 30.4 (2009): 351-366.

49 Ray, S., and J. P. Neumann. "Calculation of the binary chromiun-lanthanide phase diagrams." Journal of phase equilibria 17.3 (1996): 179-185.

50 Tortorici, P. C., and M. A. Dayananda. "Interdiffusion of cerium in Fe-base alloys with Ni or Cr." Journal of nuclear materials 204 (1993): 165-172.

51 Lo, Wei-Yang, et al. "Effects of Cr on the interdiffusion between Ce and Fe–Cr alloys." Journal of Nuclear Materials 458 (2015): 264-271.

52 Du, Yong, and Narcís Clavaguera. "Thermodynamic calculation of the Nd · Ni system." Calphad 20.3 (1996): 289-296.

53 Huang, Mianliang, R. William McCallum, and Thomas A. Lograsso. "Experimental investigation and thermodynamic modeling of the Nd–Ni system." Journal of alloys and compounds 398.1-2 (2005): 127-132.

54 Luo, Qun, et al. "Experimental investigation and thermodynamic assessment of Nd–H and Nd–Ni–H systems." Calphad 51 (2015): 282-291.

55 Du, Zhenmin, Lisha Yang, and Gang Ling. "Thermodynamic assessment of the Ce–Ni system." Journal of alloys and compounds 375.1-2 (2004): 186-190.

56 Palumbo, M., et al. "Thermodynamic analysis and assessment of the Ce–Ni system." Intermetallics 12.12 (2004): 1367-1372.

57 Xiong, Wei, et al. "Reassessment of the Ce–Ni binary system supported by key experiments and ab initio calculations." Intermetallics 15.11 (2007): 1401-1408.

58 Rahou, Z., et al. "Thermodynamic reassessment of Ni-Pr binary system." Journal of Alloys and Compounds 620 (2015): 204-209.

59 Du, Z., D. Wang, and W. Zhang. "Thermodynamic assessment of the La-Ni system." Journal of alloys and compounds 264.1-2 (1998): 209-213.

60 Dischinger, J., and H-J. Schaller. "On the constitution and thermodynamics of Ni–La alloys." Journal of alloys and compounds 312.1-2 (2000): 201-210.

61 Okamoto, H. "La-Ni (Lanthanum-Nickel)." Journal of phase equilibria 12.5 (1991): 615-616.

62 Ogata, Takanari, Mitsuo Akabori, and Akinori Itoh. "Diffusion of cerium in uranium-zirconium solid solutions." Materials Transactions 44.1 (2003): 47-52.

63 Hofman, Gerard L. "Metallic fast reactor fuels, Materials Science and Technology, A Comprehensive Treatment." Nuclear Materials 10 (1994): Part1.

64 Foust, O. J. SODIUM-NaK ENGINEERING HANDBOOK. VOLUME I. SODIUM CHEMISTRY AND PHYSICAL PROPERTIES. No. TID--26008. 1972, 1972.

65 G.J. Lamprecht and P. Crowther, "Solubility of Metals in Liquid Na: The Systems Na-Ag, Na-Zn and Na-Ce," Trans. AIME, 242 (1968), 2169-2171 (Equi Diagrams; Experimental)

66 Li, Xiang. Studies of Liquid-like Lanthanide Transport Behaviors in Metallic Nuclear Fuels. Diss. The Ohio State University, 2017.

67 Keiser Jr, Dennis D., and Robert D. Mariani. "Zr-rich layers electrodeposited onto stainless steel cladding during the electrorefining of EBR-II fuel." Journal of nuclear materials 270.3 (1999): 279-289.

68 Li, Xiang, et al. "Ab-initio molecular dynamics study of lanthanides in liquid sodium." Journal of Nuclear Materials 484 (2017): 98-102.

69 Walker, B. A., and J. N. Pratt. "The solubility of copper in liquid sodium." Journal of Nuclear Materials 32.2 (1969): 340-345.

70 Walker, R. A., and J. N. Pratt. "The solubilities of bismuth and tellurium in liquid sodium." Journal of Nuclear Materials 34.2 (1970): 165-173.

71 Lamprecht, G.J.; Crowther, P.; Kemp, D.M. “A study of the solubility of metals in liquid sodium: The system sodium-tin.” J. Phys. Chem. 71 (1967), 4209-4212.

72 Tongzai, Y. A. N. G., et al. "Determination of solubility of uranium in liquid sodium." Nuclear Science and Techniques 19.2 (2008): 93-98.

73 Stecura, Stephan. “Solubilities of vanadium, titanium, and zirconium in liquid potassium.” Technical Report TN D-5093; NASA: 1969.

74 Eichelberger, R. L., and R. L. McKisson. SOLUBILITY STUDIES OF Cr, Co, Mn, Mo, Ni, Nb, Ti, V, AND Zr IN LIQUID SODIUM. No. AI-AEC--12955. Atomics International, Canoga Park, Calif., 1970.

75 Stecura, Stephan. “Solubilities of Molybdenum and Tungsten in Liquid Potassium.” Technical Report NASA-TN-D-5504; NASA Lewis Research Center: Cleveland, OH, USA, 1969

76 Lamprecht, G. J., and P. Crowther. "SOLUBILITY OF METALS IN LIQUID SODIUM.. THE SYSTEMS SODIUM-SILVER, SODIUM-ZINC, AND SODIUM-CERIUM." Trans Met Soc AIME 242.10 (1968).

77 Johnson H.E. et al. Sodium-NaK Engineering Handbook, Vol. 1, Ed. O.J. Foust (Ed.). New York, N.Y.: Gordon and Breach Science Publishers Inc. (1972).

78 Anon. Quarterly Status Report on Advanced Reactor Technology (ART) for Period ending April 30, (1966); Technical Report LA-3524; USAEC: Los Alamos, NM, USA.

79 Griffin, R. B., and K. A. Gschneidner. "Effect of the sixth period elements on the melting and transformation temperatures of praseodymium: Part I. Experimental." Metallurgical Transactions 2.9 (1971): 2517-2524.

80 Moffatt, W.G.: "Binary Phase Diagrams Handbook", General Electric Comp., Schenectady, N.Y. (1976).

81 Borgstedt, H.U.; Guminski, C. “Solubility Data Series: Metals in Liquid Alklali Metals Part 1: Be to Os.” Oxford University Press: Oxford, UK, (1996).

82 Ferro, R.: Saccone, A. “Intermetallic Chemistry.” Elsevier: Amsterdam, The Netherlands, (2008).

83 Eichelberger, R.L.; McKisson, R.L.; Johnson, B.G. “Solubility of Refractory Metals and Alloys in Potassium and in Lithium.” National Aeronautics and Space Administration: Washington, DC, USA, (1969).

84 Eichelberger, R.L.; McKisson, R.L. “Solubility of Copper in Sodium; Technical Report Al-AEC-12671.” Atomics International: Canoga Park, CA, USA, (1968).

85 Eichelberger, R.L.; McKisson, R.L. “Studies of the solubility of Iron in Sodium; Technical Report Al-AEC-12834.” Atomics International: Canoga Park, CA, USA, (1969).

86 Fleitman, A. H., H. S. Isaacs, and J. R. Weeks. "The solubility and corrosion of pure iron in liquid sodium containing dissolved oxygen." Proceedings of 1970 Metals Conference, Cleveland, OH, USA. 1970.

87 Periaswani, G., et al. "Solubility of manganese and iron in sodium." Material

Behavior and Physical Chemistry in Liquid Metal Systems. Springer, Boston, MA, 1982. 411-420.

88 Pellett, C. R., and R. Thompson. "Measurement of Transition Metal Solubilities in Liquid Sodium; Cobalt, Nickel and Chromium." Liquid Metal Engineering and Technology. 3 (1984): 43-48.

89 Höhne, G. W. H., W. F. Hemminger, and H-J. Flammersheim. "Theoretical fundamentals of differential scanning calorimeters." Differential Scanning Calorimetry. Springer, Berlin, Heidelberg, 2003. 31-63.

90 Sangster, J., and C. W. Bale. "The Na-Sn (sodium-tin) system." Journal of phase equilibria 19.1 (1998): 76-81.

91 Bushmanov, V. D., and S. P. Yatsenko. "Immiscibility in binary systems of cesium with aluminium, gallium, indium, thallium." Izvestiya Akademii Nauk SSSR, Metally (1981): 202-204.

92 De Groot, S.R. and P. Mazur, “Non-equilibrium thermodynamics” (1962), Amsterdam; New York: North-Holland Pub. Co.; Interscience Publishers.

93 Duffy, D.G., “Green's functions with applications” (2001), Boca Raton, Fla.: Chapman & Hall/CRC

94 Mojtabi, Abdelkader, and Michel O. Deville. "One-dimensional linear advection–diffusion equation: Analytical and finite element solutions." Computers & Fluids 107 (2015): 189-195.

95 De Boer, F.R., et al. “Cohesion in Metals: Transition Metal Alloys” (1988), Elsevier: Amsterdam, The Netherlands.

96 Lyublinski, I. E., et al. "Numerical and experimental determination of metallic solubilities in liquid lithium, lithium-containing nonmetallic impurities, lead and lead-lithium eutectic." Journal of nuclear materials 224.3 (1995): 288-292.

97 Lupis, Claude HP. "Chemical thermodynamics of materials." Elsevier Science Publishing Co., Inc., 1983, (1983): 581.

98 Isler, Jeremy, and Jinsuo Zhang. "Examination of Solubility Models for the Determination of Transition Metals within Liquid Alkali Metals." Metals 6.7 (2016): 144.

99 Samin, Adib, et al. "Ab initio molecular dynamics study of the properties of cerium in liquid sodium at 1000 K temperature." Journal of Applied Physics 118.23 (2015): 234902.

100 Hong, Qi-Jun, and Axel van de Walle. "Direct first-principles chemical potential

calculations of liquids." The Journal of chemical physics 137.9 (2012): 094114.

101 B. Widom, “Some Topics in the Theory of Fluids.” The Journal of chemical physics 39.11 (1963) p.2808-2812.

102 Kresse, Georg, and Jürgen Furthmüller. "Efficiency of ab-initio total energy calculations for metals and semiconductors using a plane-wave basis set." Computational materials science 6.1 (1996): 15-50.

103 Kresse, Georg, and Jürgen Furthmüller. "Efficient iterative schemes for ab initio total-energy calculations using a plane-wave basis set." Physical review B 54.16 (1996): 11169.

104 Liu, Maoyuan, Patrick Masset, and Angus Gray-Weale. "Solubility of sodium in sodium chloride: A density functional theory molecular dynamics study." Journal of The Electrochemical Society 161.8 (2014): E3042-E3048.

105 Perdew, John P., Kieron Burke, and Matthias Ernzerhof. "Generalized gradient approximation made simple." Physical review letters 77.18 (1996): 3865.

106 Methfessel, M. P. A. T., and A. T. Paxton. "High-precision sampling for Brillouin-zone integration in metals." Physical Review B 40.6 (1989): 3616.

107 Siberchicot, Bruno, and Jean Clérouin. "Properties of hot liquid cerium by LDA+ U molecular dynamics." Journal of Physics: Condensed Matter 24.45 (2012): 455603.

108 Borgstedt, Hans Ulrich, and Cezary Guminski. "Solubilities and Solution Chemistryin Liquid Alkali Metals." Monatshefte für Chemie/Chemical Monthly 131.9 (2000): 917-930.

109 Zhang, Xudong, and Shaoqing Wang. "First-principles study of thermodynamic properties and solubility of aluminum-rare-earth intermetallics." Computational Materials Science 90 (2014): 56-60.

110 Shaoqing, ZHANG Hui WANG. "First-principles study on the phase stability of Mg-La and Mg-Nd binary alloys." Acta Metall Sin 48.7 (2012): 889-894.

111 Li Xiang, Zhang Jinsuo, Unal C., Mariani R. D., “First-principle study of iron and cerium in sodium”, Submitted to Progress in Nuclear Energy

112 Togo, Atsushi, and Isao Tanaka. "First principles phonon calculations in materials science." Scripta Materialia 108 (2015): 1-5.

113 David A. Porter, Kenneth E. Easterling and Mohamed Y. Sherif, “Phase Transformations in Metals and Alloys.” (2009) Chapter 1.5, pp 31-42.

114 F.R. deBoer, et al, “Cohesion in Metals: Transition Metal Alloys”, North-Holland, Amsterdam (1988), Chapter II, p:38-84.

115 Atkins, Peter; Jones, Loretta, “Chemical Principles: The Quest for Insight (4th ed.).” W. H. Freeman and Company (2008) p. 236

116 Blöchl, P. E., “Projector augmented-wave method”. Physical Review B, (1994) 50(24): p. 17953-17979.

117 Zhang, J., P. Hosemann, and S. Maloy. "Models of liquid metal corrosion." Journal of Nuclear Materials 404.1 (2010): 82-96.

118 Stanaway W.P. and Thompson R., second Intern. Conf. on Liquid Metal Technology in Energy Production, Conf-800401-P2, Richland, Washington (1980) pp. 18-54.

119 Borgstedt, H.U., Mathews, C.K, “Thermochem and Chemical Processing.” Indian Institute of Metals, Kalpakham (1992) p. 141-147

120 Thorley, A.W., H.U. Borgstedt, “Material Behavior & Physical Chemistry in Liquid Metal Systems.” Plenum, N.Y., (1982) p. 19-36.

121 G.J. Lamprecht and P. Crrowther, “Transaction of the metallurgical society of AIME” Vol 242 (1968), p.2169-2171

122 Mariani, Robert D., et al. "Lanthanides in metallic nuclear fuels: Their behavior and methods for their control." Journal of Nuclear Materials 419.1-3 (2011): 263-271.

123 Isler, Jeremy Payton. Interactions of Lanthanides and Liquid Alkali Metals for" Liquid-Like" Lanthanide Transport in U-Zr Fuel. Diss. The Ohio State University, 2017.

124 Li, Xiang, et al. "Ab-initio molecular dynamics study of lanthanides in liquid sodium." Journal of Nuclear Materials 484 (2017): 98-102.

125 Li, Xiang, et al. “Behaviors of Ce, Pr and Nd in liquid cesium by Ab-initio molecular dynamics simulations.” Journal of Nuclear Materials (2017), Submitted.

126 Einstein, Albert. "Zur theorie der brownschen bewegung." Annalen der physik 324.2 (1906): 371-381.

127 Yuryev, A. A., and B. R. Gelchinski. "Simulation of properties of liquid alkali metals at high temperatures and pressures by ab initio molecular dynamics method." Doklady Physics. Vol. 60. No. 3. Pleiades Publishing, 2015.

128 Vandarkuzhali, S., et al. "Electrochemistry of rare earth oxy ions REO+ (RE= Ce, La, Nd) in molten MgCl2–NaCl–KCl eutectic." Journal of Electroanalytical Chemistry 611.1-2 (2007): 181-191.

129 Wax, Jean-François, and N. Jakse. "Molecular dynamics simulation study of the interdiffusion properties of liquid Na-K alloys." Journal of Physics: Conference Series. Vol. 98. No. 4. IOP Publishing, 2008.

130 Kakinuma, Fujio, et al. "A structural study of liquid Te-rich Si-Te alloys." Journal of Physics: Conference Series. Vol. 502. No. 1. IOP Publishing, 2014.

131 Yuryev, Anatoly A., and Boris R. Gelchinski. "Ab initio molecular dynamics study of liquid sodium and cesium up to critical point." AIP Conference Proceedings. Vol. 1673. No. 1. AIP Publishing, 2015.

132 Jie, Wanqi. "Solute redistribution and segregation in solidification processes." Science and Technology of Advanced Materials 2.1 (2001): 29-35.

133 Caldwell, E. C., F. J. Fela, and G. E. Fuchs. "The segregation of elements in high-refractory-content single-crystal nickel-based superalloys." JOM 56.9 (2004): 44-48.

134 Zeller, R., and P. H. Dederichs. "Calculations for the electronic structure of isolated cerium impurities." Physica B+ C 130.1-3 (1985): 34-36.

135 Krishna, R., and J. M. Van Baten. "The Darken relation for multicomponent diffusion in liquid mixtures of linear alkanes: an investigation using molecular dynamics (MD) simulations." Industrial & engineering chemistry research 44.17 (2005): 6939-6947.

136 Gaston, Derek, et al. "MOOSE: A parallel computational framework for coupled systems of nonlinear equations." Nuclear Engineering and Design 239.10 (2009): 1768-1778.

137 MOOSE (software).. In Wikipedia, The Free Encyclopedia. Retrieved 13:39, March17,2017,
from https://en.wikipedia.org/w/index.php?title=MOOSE_(software)&oldid=770430226

138 Knoll, Dana A., and David E. Keyes. "Jacobian-free Newton–Krylov methods: a survey of approaches and applications." Journal of Computational Physics 193.2 (2004): 357-397.

139"MOOSE Framework - Open Source Multiphysics". Idaho National Laboratory. Retrieved 2017-03-17. http://mooseframework.org/

140 Kirk, Benjamin S., et al. "libMesh: a C++ library for parallel adaptive mesh refinement/coarsening simulations." Engineering with Computers 22.3-4 (2006): 237-254.

141 Williamson, R. L., et al. "Multidimensional multiphysics simulation of nuclear fuel behavior." Journal of Nuclear Materials 423.1-3 (2012): 149-163.

142 Gamble, Kyle Allan Lawrence, et al. BISON and MARMOT Development for Modeling Fast Reactor Fuel Performance. No. INL/EXT--15-36440. Idaho National Laboratory (INL), Idaho Falls, ID (United States), 2015.

143 Galloway, Jack D., Neil N. Carlson, and Cetin Unal. BISON framework for the analysis of performance of metallic fuels. No. LA-UR-12-26297. Los Alamos National Laboratory (LANL), 2012.

144 Carlson, Neil N., Cetin Unal, and Jack D. Galloway. Formulation of the Constituent Distribution Model Implemented into the BISON Framework for the Analysis of Performance of Metallic Fuels with Some Initial Simulations Results. No. LA-UR-13-26824. Los Alamos National Laboratory (LANL), 2013.

145 Gao, Jeff Y. "Studying Dissolution with a Model Integrating Solid–Liquid Interface Kinetics and Diffusion Kinetics." Analytical chemistry 84.24 (2012): 10671-10678.

146 Zheng, L. L., D. J. Larson Jr, and H. Zhang. "Role of thermotransport (Soret effect) in macrosegregation during eutectic/off-eutectic directional solidification." Journal of crystal growth 191.1-2 (1998): 243-251.

147 Brenan, James M., and Neil Bennett. "Soret separation of highly siderophile elements in Fe–Ni–S melts: Implications for solid metal–liquid metal partitioning." Earth and Planetary Science Letters 298.3-4 (2010): 299-305.

148 Kovacina, T. A., P. G. Johnson, and R. R. Miller. Kinetics of Excess Solute Precipitation in Liquid Sodium Solutions. No. NRL-6424. NAVAL RESEARCH LAB WASHINGTON DC, 1966.

149 Jakubiak, Paulina, et al. "Development of a unified dissolution and precipitation model and its use for the prediction of oral drug absorption." Molecular pharmaceutics 13.2 (2016): 586-598.

150 Olander, Donald R. Fundamental aspects of nuclear reactor fuel elements: solutions to problems. No. TID-26711-P2. California Univ., Berkeley (USA). Dept. of Nuclear Engineering, (1976), pp 210-213

151 Arnold, C. W., Jack Galloway, and Cetin Unal. "Modeling Lanthanide Transport in Metal Fuels with BISON." Paris, France, September (2015): 20-24.

152 Carmack, William J. Temperature and burnup correlated FCCI in U-10Zr metallic fuel. No. INL/EXT-12-25550. Idaho National Laboratory (INL), 2012.

153 https://en.wikipedia.org/wiki/Experimental_Breeder_Reactor_II

154 Jain, Anubhav, et al. "Commentary: The Materials Project: A materials genome approach to accelerating materials innovation." Apl Materials 1.1 (2013): 011002.

155 Alchagirov, Boris Batokovich, and Alexandr Gerasimovich Mozgovoi. "The density of liquid cesium in the vicinity of the melting point." High temperature 44.2 (2006): 216-220.

156 Fink, J. K., and L. Leibowitz. Thermodynamic and Transport Properties of Sodium Liquid and Vapor (Argonne Natioal Laboratory, 1995). ANL/RE-95/2.

157 Huijben, M. J., et al. "Density of liquid sodium-caesium alloys." Scripta Metallurgica 9.6 (1975): 653-656.

158 Ogata, Takanari, Mitsuo Akabori, and Akinori Itoh. "Diffusion of cerium in uranium-zirconium solid solutions." Materials Transactions 44.1 (2003): 47-52.

159 Roth, K., Soil Physics Lecture Notes, V2.2, Institute of Environmental Physics, Heidelberg University, D-69120 Heidelberg, Germany, 2012

160 Bruna, Maria, and S. Jonathan Chapman. "Diffusion in spatially varying porous media." SIAM Journal on Applied Mathematics 75.4 (2015): 1648-1674..

161 Weissberg, Harold L. "Effective diffusion coefficient in porous media." Journal of Applied Physics 34.9 (1963): 2636-2639.

162 Bozzolo, G., et al. "Surface properties, thermal expansion, and segregation in the U–Zr solid solution." Computational Materials Science 50.2 (2010): 447-453.

163 Huber, J. G., and P. H. Ansari. "The superconductivity of BCC U-Zr alloys." Physica B+ C 135.1-3 (1985): 441-444.

164 Blöchl, Peter E. "Projector augmented-wave method." Physical review B 50.24 (1994): 17953.

165 Kresse, Georg, and D. Joubert. "From ultrasoft pseudopotentials to the projector augmented-wave method." Physical Review B 59.3 (1999): 1758.

166 Perdew, John P., Kieron Burke, and Matthias Ernzerhof. "Generalized gradient approximation made simple." Physical review letters 77.18 (1996): 3865..

167 Methfessel, M. P. A. T., and A. T. Paxton. "High-precision sampling for Brillouin-zone integration in metals." Physical Review B 40.6 (1989): 3616.

168 Monkhorst, H. J. and Pack, J. D., “Special points for Brillouin-zone integrations.” Physical Review B, 13.12 (1976), p. 5188-5192

169 Henkelman, Graeme, Blas P. Uberuaga, and Hannes Jónsson. "A climbing image nudged elastic band method for finding saddle points and minimum energy paths." The Journal of chemical physics 113.22 (2000): 9901-9904.

170 Sheppard, Daniel, Rye Terrell, and Graeme Henkelman. "Optimization methods for finding minimum energy paths." The Journal of chemical physics 128.13 (2008): 134106.

171 Katz, L., M. Guinan, and R. J. Borg. "Diffusion of H 2, D 2, and T 2 in single-

crystal Ni and Cu." Physical review B 4.2 (1971): 330.

172 Ogata, Takanari, Mitsuo Akabori, and Akinori Itoh. "Diffusion of cerium in uranium-zirconium solid solutions." Materials Transactions 44.1 (2003): 47-52.

173 Kim, Yeon Soo, et al. "Modeling of constituent redistribution in U–Pu–Zr metallic fuel." Journal of nuclear materials 359.1-2 (2006): 17-28.